Investigation of dipole blockade in ultracold atomic ensembles

---

Jagoda Radogostowicz

Advisor:
Prof. Ennio Arimondo

Università degli Studi di Pisa
Dipartimento di Fisica *E. Fermi*
Corso di Dottorato in Fisica Applicata

To my brother Ziemowit, to my parents Urszula and Witold and
to my love Lorenzo…

"If you want to make God laugh, tell him about your plans."
Woody Allen

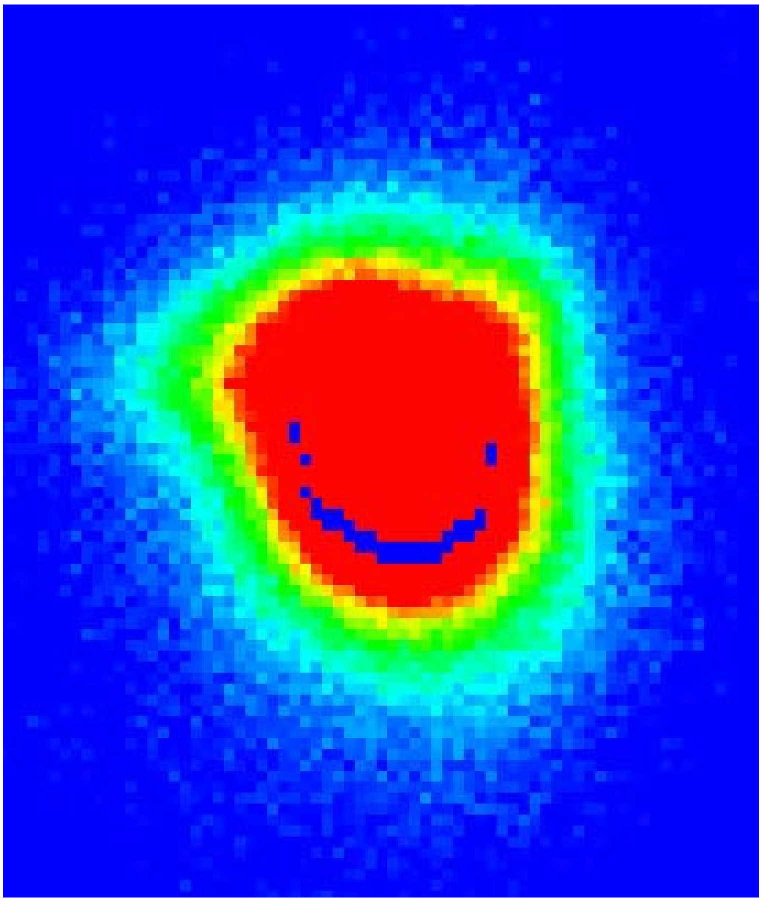

Sometimes even atoms smile :)

Contents

Chapter 1

Introduction

Owing to new available technologies, new research fields become available to scientists. Within the area of atomic physics, the ultracold gas technologies open new perspectives in the investigation of the regimes with strong interactions between atoms. A wide range of applications is associated with the manipulation in different configurations of ultracold atoms excited to highly excited states. Rydberg atoms have been intensively studies since nineteen seventy and due the merge of this field with ultracold atomic physics, cold Rydberg atoms brought several concepts to a new light. Rydberg atoms are known to exhibit strong dipolar moments hence flexible investigations of strong interactions between excited atoms become an interesting subject. For example it becomes possible to investigate interactions between individual particles.

One of the implications of the strong interactions between Rydberg atoms is the phenomenon denominated as dipole blockade [44, 51], that has been recently studied both theoretically, for instances [4, 17], and experimentally for different atomic ensembles, as in [72, 33, 38]. This concept is presented in the context of atomic clocks [15], quantum computation [29], quantum cryptography [6] and quantum information [51, 44]. Further research on the Rydberg-Rydberg interactions has produced collective coherent excitations [39, 39, 33, 45] and a non-linear dependence on the number of excited atoms as a function of intensity of the irradiation lasers and atomic density [72, 67].

In order to achieve the quantum computation targets [60], the implementation of quantum protocols consisting of a sequence of quantum gates requires an experimental realization of a quantum bit. As Rydberg atoms exhibit long range interactions they were proposed to be suitable candidates for realization of controllable quantum systems [44]. Yet, the implementation of a quantum gate is an ambitious task where a coherent manipulation of a great number of coupled states is needed. For this reason it was proposed that Rydberg excitations should be performed in samples with a precise spatial order. As a solution atoms in optical lattices were proposed. Already a strong interest in optical lattices as a tool of investigation of ultracold atoms [59],[8] or as a tool of addressing the atoms has been showed [59]. The combination of the strong interactions between Rydberg atoms with the possibility of implementing a spatial order that will simplify coherent manipulation of a large number of coupled states provide us with exciting applications for the quantum information.

The main goal of my thesis is to present new results on the excitation of Rydberg atoms from ultracold atomic samples obtained during my work as. The dipole blockade and its experimental implications without and with the presence of optical lattices are presented. This thesis shows results on Rydberg excitations of rubidium Bose condensates in one-dimensional periodic potentials. The coherent excitation dynamics of up to 30 Rydberg states in a condensate occupying around 100 sites of an optical lattice was observed. The zero-dimensional character of the system, in which at most one Rydberg excitation is present per lattice site, is ensured by expanding the condensate in a cylindrical trap in which the radial size of the atomic cloud is much less than the blockade radius of the Rydberg states with $55 < n < 80$.

This thesis encompasses six chapters and is organized as follows:

- Chapter 2 is an introduction to general ideas of atomic physics. It introduces basic theoretical concepts such as the light shift or the three level atom. These concepts have applications while performing our experiments. Moreover, a short characterization of Rydberg atoms and their properties is included. The most important topic of this thesis the Rydberg dipole blockade is also described.

- Chapter 3 describes the theoretical background of Bose Einstein condensation. The first part presents the trapping and cooling methods used in experimental realization of ultracold atoms. The second part of the chapter gives an overview of cold atoms in periodic potentials. It presents also how to realize a periodic potential by light interference.

- Chapter 4 is devoted to experimental setup. The experimental apparatus of the Pisa BEC laboratory is described. An accurate description of the experimental procedure applied to reach the BEC quantum phase in dilute gases is included. This chapter also includes information about excitation of Rydberg atoms and the implementation of periodic potentials. The setup used in this thesis to prepare cold atomic samples was build at the end of last century and described in detail in the PhD thesis of Donatella Ciampini [19]. The part of the setup used to create optical lattices was implemented and presented in the PhD thesis's of Alessandro Zenesini [75] and Carlo Sias [66]. Therefore those setups will be not described with full details.

The part of setup dedicated to Rydberg excitations was mainly build during my PhD work and is first described in details in the present thesis and also reported in Viteau et al. [74].

- Chapter 5 describes the characterization of experimental parameters such as the Rabi frequencies and the efficiency of the ion detection. The first results obtained on the photoionization of Bose Einstein condensates and cold atoms in magneto-optical traps are also shown. Moreover, the effects of excitation lasers and electric fields on the atomic ensembles are mentioned. All the material contained in this chapter, and in the following ones, is the result of my original research work, in collaboration with other members of the BEC team.

- Chapter 6 presents our results on the excitations of Rydberg atoms from both BEC samples and cold atoms trapped in a MOT. The experiments exploring different BEC density regimes and their influence on the ion production are presented. A new method of estimating the dipole blockade radius is examined. The further part of chapter 5 reports the temporal dependence of the detected ions on the duration of the irradiating laser pulse. Results for different atomic density regimes and different quantum number n are shown. Clear signatures of sub-Poissonian counting statistics in the regime of strong interactions have been measured.

- Chapter 7 is devoted to description of the cold Rydberg atoms experiments performed within the periodic potential of optical lattices. The influence of the Rydberg excitations in optical lattices on the phase coherence of a Bose Einstein condensate is examined. The coherent excitations of the ultracold atomic samples are described. The influence of atomic distributions is also taken into account. A new method of spatial distribution cleaning is presented.

Chapter 2

Atomic Physics Foundations

2.1 Atom-Light Interactions

To deal with ultracold atoms it is crucial to understand atom light interactions. A major part of the techniques used in our experiments is based on the interactions between the matter and light. During the preparation of ultracold samples the optical pumping into chosen state is used. Then dipole traps are based on the idea of a dipole force acting on atoms. Another implementation of the atom light interactions may be found in imaging the atoms. To manipulate ultracold samples we use optical lattices that are also based on the dipole force. In the experiments with Rydberg atoms, ultracold samples are excited by mean of the two photon transitions.

The simplest model describing the properties of these interactions is the two level atom presented in (2.1.1). Since the Rydberg atoms used in the experiments presented in this thesis are excited via two photon excitation, a three level atom is described in subsection (2.1.3). Most of the experiments described in this work use far detuned transitions, so section (2.1.3) also deals with an effective two level atom.

2.1.1 A Two-level Atom

In this section the basis of atom light interaction theory is described. The detailed description of this problem can be found in ref. [57]. We consider a closed two level atom composed by the ground state $|g\rangle$ and the excited state $|e\rangle$ decaying to the ground state by spontaneous emission with rate Γ. They are separated by $\hbar\omega_0$. In figure 2.1 a schematic picture of the two level atom is presented. The atom is irradiated by monochromatic light with frequency ω_L and detuned by Δ. This system is described by total Hamiltonian H:

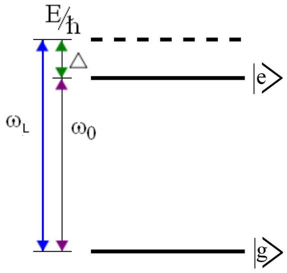

Figure 2.1: A two level atom with the ground state $|g\rangle$ and an excited $|e\rangle$, where $\hbar\omega_0$ is the energy difference between these states. Laser coupling between $|e\rangle$ and $|g\rangle$ has a frequency ω_L and is detuned by $\Delta = \omega_L - \omega_0$ from resonance.

$$H = H_A + H_L + H_{AL}, \tag{2.1}$$

where H_A stands for the electronic energy of the atom, H_L is the energy of the light and H_{AL} represents the atom-light interaction. The three contributions are [57]:

$$H_A = \hbar\omega_0 \left|e\right\rangle \left\langle e\right|, \tag{2.2}$$

$$H_L = \hbar\omega_L(\hat{a}^+\hat{a} + \frac{1}{2}), \tag{2.3}$$

$$H_{AL} = \frac{\hbar\Omega}{2}\left(\left|g\right\rangle \left\langle e\right| \hat{a} + \left|e\right\rangle \left\langle g\right| \hat{a}^+\right), \tag{2.4}$$

where $\hat{a}^+$ and $\hat{a}$ are creation and annihilation operators. In equation (2.4), the dipole approximation is made. In this case the size of the atom is neglected with respect to the wavelength of the light. The resonant Rabi frequency is given by the dipole coupling of the two states:

$$\Omega = \frac{-eE_0}{\hbar}\left\langle e\right| r \left|g\right\rangle = \frac{-E_0}{\hbar}\mu_{eg}, \tag{2.5}$$

where E_0 stands for electric field amplitude. For the purpose of this subsection we can assume a classical light field omitting creation and annihilation of photons. In this way the dynamics of the system can be described using the density matrix ρ. The convenience of the two-level atom is that it evolves in accordance with the optical Bloch equations (OBEs). The steady state solution of the OBE permits the estimation of the steady state for the excited population ρ_{ee}:

$$\rho_{ee} = \frac{s_0/2}{1 + s_0 + (2\Delta/\Gamma)^2} = \frac{\Omega^2}{\Gamma^2 + 2\Omega^2 + 4\Delta^2}, \tag{2.6}$$

where Γ is a decay rate from the excited state and s_0 stands for on-resonant saturation parameter given by:

$$s_0 = \frac{2\Omega^2}{\Gamma^2} = \frac{I}{I_s}. \tag{2.7}$$

In equation (2.7) I_s is the saturation intensity defined as:

$$I_s = \pi hc/3\lambda^3\tau, \tag{2.8}$$

where λ is the wavelength of the irradiating light. In general the saturation parameter is given by:

$$s = \frac{\Omega^2/2}{\Delta^2 + \Gamma^2/4}. \tag{2.9}$$

For $s << 1$ populations are mostly in the ground state and at larger values they are distributed between the excited and the ground state, for instance at $s = 1$ in a one to three ratio. When the excitation rate and decay rate in the steady state are equal the total scattering rate Γ_{sc} of light from the laser field is given by:

$$\Gamma_{sc} = \Gamma\rho_{ee} = \frac{\Gamma\Omega^2}{\Gamma^2 + 2\Omega^2 + 4\Delta^2}. \tag{2.10}$$

In the case of strong damping $\Gamma >> \Omega$ the solution of the optical Bloch equations give the excited state population:

$$\rho_{ee}(t) = \frac{\Omega^2}{4\Delta^2 + \Gamma^2}\left(1 + e^{-\Gamma t} - 2\cos\Delta t e^{-\Gamma t/2}\right). \tag{2.11}$$

At very high intensities i.e. for $s_0 >> 1$, power broadening of the linewidth of the transition may be observed. Its power-broadened value Γ' is given by:

$$\Gamma' = \Gamma\sqrt{1 + s_0}. \tag{2.12}$$

The quantities derived above can be used to calculate the absorption of a laser beam by an atomic cloud due to re-scattering of the laser light. The scattering of light from a laser beam results in intensity losses as spontaneously re-emitted photons are spread over the whole solid angle. This reduction is given by:

$$\frac{dI}{dz} = -\hbar\omega_L\Gamma_{sc}n_g, \tag{2.13}$$

where I stands for the intensity of the light and n_g is the atomic density. When laser light intensity near resonance is low, the scattering rate is given by $\Gamma_{sc} = s_0\Gamma/2$ and therefore, the absorption rate is:

$$\frac{dI}{dz} = -\sigma_{eg}n_gI, \tag{2.14}$$

where σ_{eg} for scattering light out of the beam on resonance given by:

$$\sigma_{eg} = \frac{\hbar\omega\Gamma}{2I_s} = \frac{3\lambda^2}{2\pi}. \tag{2.15}$$

2.1.2 Light Shift and Dressed States

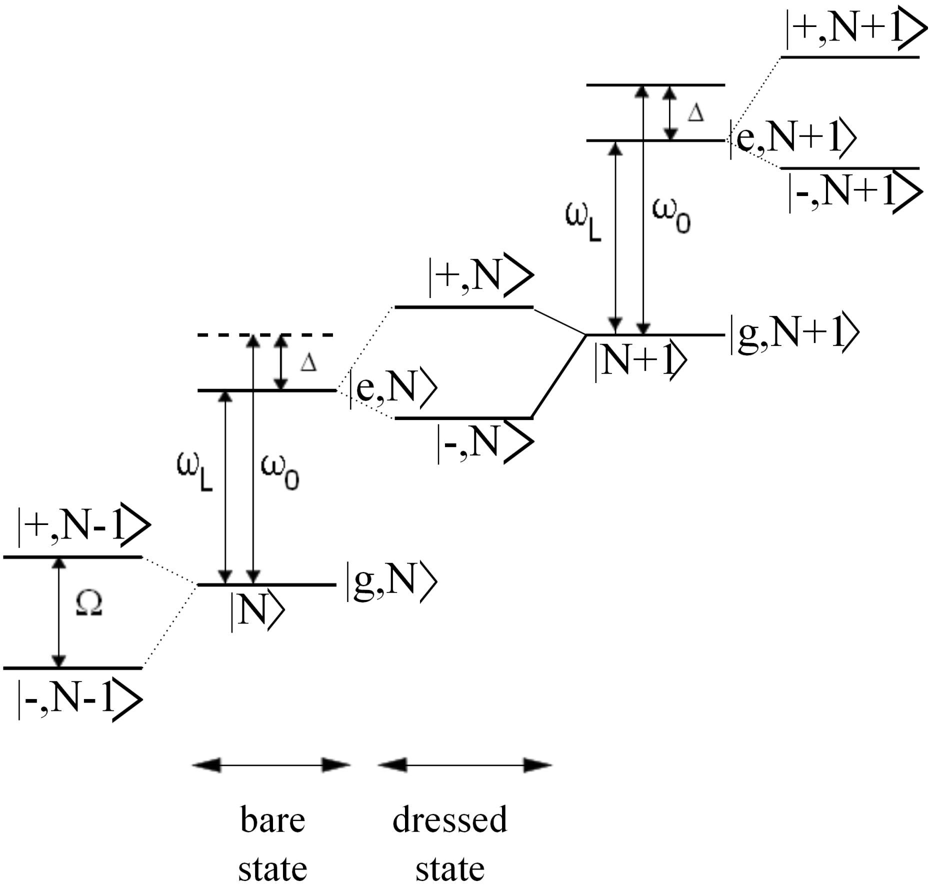

Figure 2.2: The dressed atom picture for a two level atom. N and N+1 are the number of photons in the light mode.

The light shift of atomic or molecular states caused by electromagnetic radiation must be considered when one performs high resolution spectroscopy experiments. Such a light shift perturbs the atomic frequencies whose measurement may be the goal of several experiments. For example in our experiment we exploit the light shift in order to generate potential in light fields for example dipole traps or optical lattices. When the quantization of the light field is taken into account we can talk about the dressed atom picture. The dressed state approach combines an atom with its bare states $|g\rangle$ and $|e\rangle$ and eigenstates of the light fields $|N\rangle$. This concept is discussed in details in ref. [21]. Figure 2.2 presents an intuitive dressed state picture. This figure shows the atomic levels from section 2.1.1 plotted and horizontally separated for different number of photons in the light mode (N-1, N, N+1,...). The corresponding energy state is denoted by the atomic state and by the photon number. Its energy is the sum of the light mode energy and atomic excitation energy. The coupling between the atom and the laser field leads to a mixing of these states, resulting in the dressed states. In figure (2.2) $|g, N+1\rangle$ and $|e, N\rangle$ form a new states called $|+, N\rangle$ and $|-, N\rangle$ with the energy given by:

$$E_{\pm} = \pm\frac{\hbar}{2}\sqrt{\Omega_0^2 + \Delta^2} = \pm\frac{\hbar}{2}\Omega_{eff}, \tag{2.16}$$

this equation defining an effective Rabi frequency Ω_{eff}. Each of these states consists of a superposition of both atomic states. Fraction of each state on resonance, $\Delta = 0$, is 50% and far from the resonance, $\Delta >> \Omega$, every state has a dominant contribution of one atomic state. The shift with respect to dominating state also known as the ac Stark shift Δ_{ac} is:

$$\Delta_{ac} = \pm\left(\frac{1}{2}\sqrt{\Omega^2 + \Delta^2} - \frac{\Delta}{2}\right) \approx \pm\frac{\Omega^2}{4\Delta}. \tag{2.17}$$

2.1.3 Three-level Atom and an Effective Two-level Atom

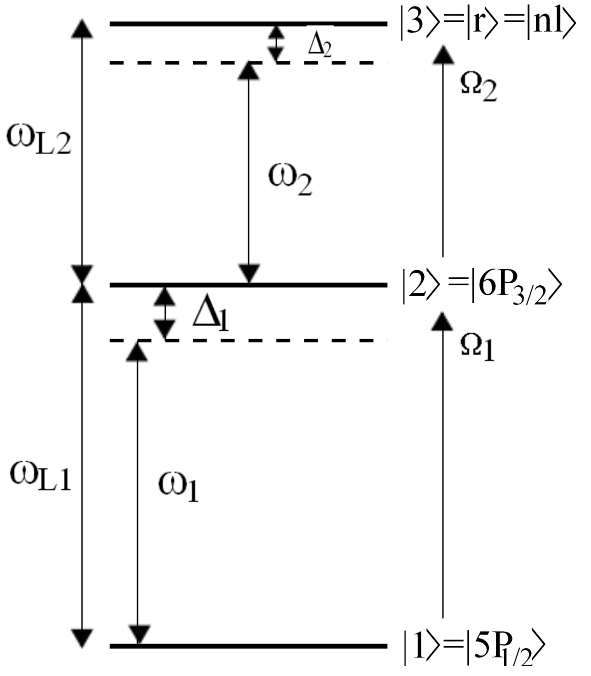

Figure 2.3: The Three level atom. An atom with the ground state $|1\rangle$, first excited state $|2\rangle$ and second excited state $|3\rangle = |r\rangle$ coupled by two laser modes.

When the two level scheme is expanded to the three level one, new applications become available. Therefore, in this subsection a three level system is explained. Applications of this system are relevant for the experiments presented in this thesis:

- **a)** Measurement of the Autler-Townes Splitting which in a three-level configuration is used to to experimentally estimate the Rabi frequency of the strongly driven transition. In the present investigtion the first step of the transition is strongly driven, whereas the second is weak to probe the Rydberg states. The spectroscopy on the transition connecting $|3\rangle$ and $|2\rangle$ shows two lines due to the dressed state, each containing a fraction of $|2\rangle$. The splitting of these lines is the effective Rabi frequency Ω_{eff}. Experimental implementation of this effect (Autler-Townes splitting [5]) will be shown in chapter 5 as a tool in to measure first step transition Rabi frequency.
- **b)** Excitation of the Rydberg atoms, where the two photon transition is used. In figure 2.3 the three level system is presented. An atom is irradiated by two light pulses with frequencies ω_{L1} and ω_{L2} respectively. The laser light for both steps is slightly detuned from the resonance, detunings being Δ_{L1} and Δ_{L2}, respectively. The coupling strength of each transition step is described as Ω_1 for the first step and Ω_2 for the second one.

Most of our experiments done with the Rydberg atoms is detuned from the intermediate state. This detuning is much larger than the resonant Rabi frequencies. For this reason that state is almost not populated. Then, if decay from $|r\rangle$ to $|2\rangle$ is neglected, $|2\rangle$ mat be adiabatically eliminated and a reduction to an effective two level atom can be applied. For the Rydberg excitation scheme the method is found in Appendix A of [52]. The effective resonant two photon Rabi frequency is given by:

$$\Omega'_{eff} = \frac{\Omega_1 \Omega_2}{4\Delta_{L1}}, \tag{2.18}$$

with an effective two-photon detuning modified with respect to $\Delta_{L1} + \Delta_{L2}$ by a light shift analogous to that of equation (2.17):

$$\Delta_{eff} = \Delta_{L1} + \Delta_{L2} + \frac{|\Omega_2|^2}{4\Delta_{L1}} - \frac{|\Omega_1|^2}{4\Delta_{L1}}. \tag{2.19}$$

Therefore, the effective non-resonant Rabi frequency is given by:

$$\Omega_{eff} = \sqrt{\Omega'^2_{eff} + \Delta^2_{eff}}. \tag{2.20}$$

A more precise adiabatic elimination procedure was developed in ref. [14] for a three-level Λ scheme. The additional light shift introduced in equation (2.19) is small enough to be neglected. Therefore in our experiments we take into consideration only equation (2.18).

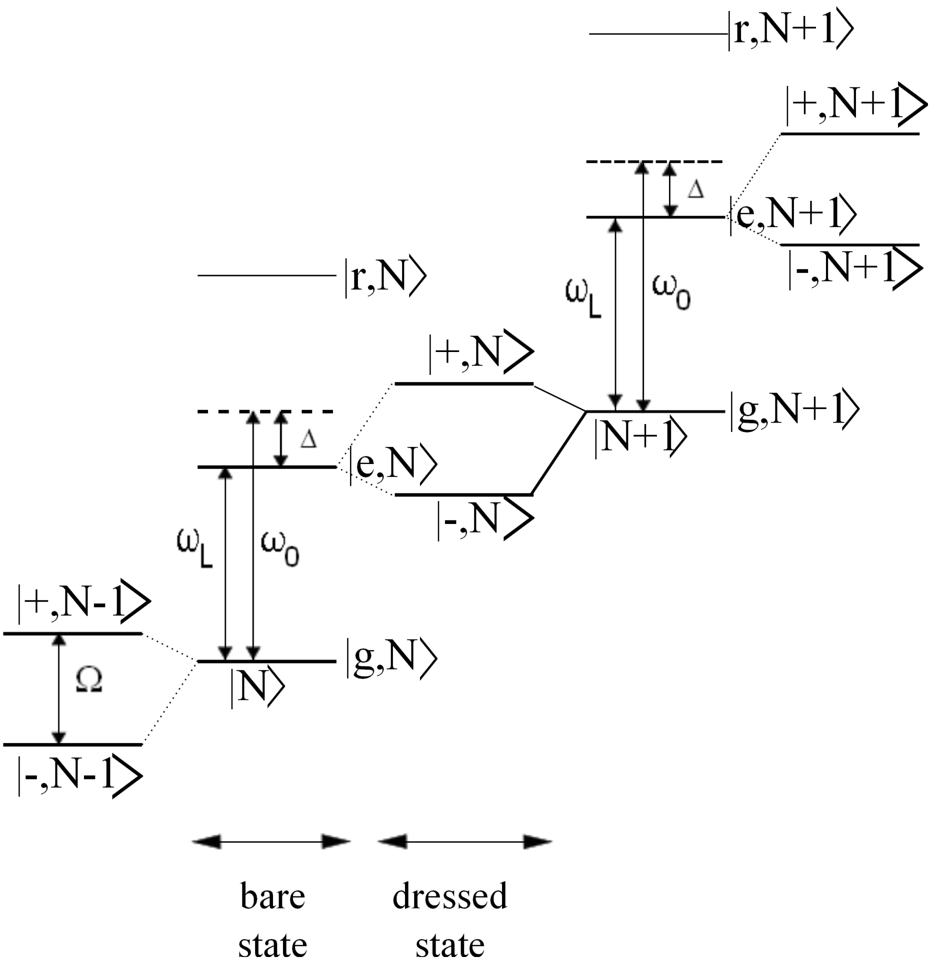

Figure 2.4: Dressed atom picture for three level atom coupled by two laser modes. this scheme is very similar to the dressed two level atom in figure 2.2. The additional state $|r\rangle$ is used as a third level.

2.2 Rydberg Atoms

In the previous section (2.1) the three level atom was discussed. In this part the nl Rydberg state will replace former $|3\rangle = |r\rangle$ level. Rydberg atoms are atoms excited to high energy states, described by the principal quantum number n. Intense studies on Rydberg atoms have been conducted since the 1970s and they have played an important role in atomic physics ever since. They were first observed in 1885 by Balmer and presented in his formula for wavelengths of visible series of atomic hydrogen for transitions from n_i=2 to a higher level with a quantum number n [34]:

$$\lambda = \frac{4c}{R_y} \frac{n^2}{n_i^2 - 4}. \tag{2.21}$$

The large distance of the electron from the atomic core determines most of the physical properties of Rydberg atoms. For instance the radius of an excited atom scales like n^2 and can hence become very large (for n=100 about one μm) compared to the atom in a ground state (order of nm). Rydberg atoms can stay in the excited state for long periods of time, for n=100 almost one second. They are sensitive even to small electric fields via the Stark effect. Their advantage, for several experiments over neutral ground state atoms is the high polarizability that scales like n^7. This section will briefly introduce the properties of Rydberg atoms, already described in [34] and the interactions between them..

2.2.1 Properties of Rydberg Atoms

A Rydberg atom can be described as an electron orbiting around the atomic core. This electron “feels” mainly the Coulomb potential of the Z protons in the nucleus. This nucleus is shielded by Z-1 core electrons. This configuration resembles hydrogen and therefore, a lot of the properties of Rydberg atoms can be derived from the hydrogen atom approach. The energy and radius of hydrogen atom with an electron in a state with principal quantum number n are given by:

$$E_n = -\frac{R_y hc}{n^2}, \tag{2.22}$$

$$r_n = a_0 n^2, \tag{2.23}$$

where a_0 stands for the Bohr radius and R_y for the Rydberg constant:

$$Ry = \frac{m_e e^4}{8\epsilon_0^2 h^3 c} = -13.6 \text{ eV}. \tag{2.24}$$

Rydberg states with small angular momentum $l < 4$ are called *defect states*. This defect is due to the energy shift caused by the core electrons. This shift has to be taken into account by replacing the principal quantum number n with an effective principal quantum number $n^* = n - \delta_l$. The quantum defect, δ_l, can be calculated with the Rydberg-Ritz formula [34]. Table (2.1) shows the properties of Rydberg atoms that are important for following discussion.

2.2.2 Dipole matrix elements

One condition for a coherent two photon excitation to the Rydberg state is that the excitation rate Ω is bigger than the decay rate Γ. When this requirement is

Table 2.1: scaling laws for properties of Rydberg atoms.

Property	Expression	P state n-scaling law
Binding energy	$E_n = -\frac{R_y}{(n^*)^2}$	$(n^*)^{-2}$
Level spacing	$E_n - E_{n-1}$	$(n^*)^{-3}$
Polarizability	$\pi \left(\langle r \rangle\right)^2$	$(n^*)^7$
Liftime (spontaneous decay)	$\tau = \tau' n^{*\gamma}$	$(n^*)^3$
Lifetime (black body radiation)	$\tau_{bb} = \frac{3\hbar(n^*)^2}{4\alpha^3 k_B T}$	$(n^*)^2$
Transition dipole moment	$\mu_{5P,nS} = 4.4154(n^*)^{-1.5}$	$(n^*)^{-1.5}$
Dipole-dipole interaction coefficient	C_3	$(n^*)^4$
van der Waals interaction coefficient	C_6	$(n^*)^{11}$

met one can observe coherent excitation. Both Ω and Γ depend on the quantum number n. The Rabi frequency in a two level atom is proportional to the matrix transition element μ_{eg} and the decay rate Γ_{eg} is proportional to its square:

$$\Gamma_{eg} = \frac{2\omega_{eg}^3}{3\epsilon_0 h c^3}\mu_{eg}^2. \tag{2.25}$$

This matrix element can be decomposed to a radial $R_{n'l',nl}$ and an angular $A_{l'm',lm}$ part. For the transition caused by the absorption of a photon μ_{eg} is given by:

$$\mu_{eg} = e \left\langle e\right| \hat{\epsilon} r \left|g\right\rangle = e \left\langle n'l'm'\right| \hat{\epsilon} r \left|nlm\right\rangle = e \left\langle n', l' \right\| r_q \left\| n, l \right\rangle A_{l'm',lm}, \tag{2.26}$$

where the states are described using their quantum numbers (*n,l,m*), m stands for magnetic quantum number and the final states are indicated by an apostrophe (*n',l'm'*). the radial part of the dipole matrix is in the order of $a_0 n^2$ and it is defined as:

$$\left\langle n', l' \right\| r \left\| n, l \right\rangle = \sqrt{l_{max}} R_{n',l',nl}, \tag{2.27}$$

where l_{max} stands for the maximum of l' and l and $R_{n',l'nl}$ is given by

$$R_{n',l',nl} = \int r^2 dr R_{n',l'}(r) r R_{n,l}(r). \tag{2.28}$$

2.2.3 Lifetime of Rydberg States

All atoms that are excited to Rydberg states are subject to spontaneous emission. A Rydberg state has many lower lying *n,l* states it can decay to. Therefore, the total lifetime of a state is the sum of all decay rates through all decay channels:

$$\frac{1}{\tau} = \sum_{n,l} A_{n',l',nl}, \tag{2.29}$$

where $A_{n',l',nl}$ are the Einstein A-Coefficient describing the total decay rate from a state n',l' to a state n,l:

$$A_{n'l',nl} = \sum_{m,q} \frac{2\omega_{eg}^3}{3\epsilon_0 hc^3} | \langle n'l'm' | \,\hat{\epsilon} r\, | nlm \rangle |^2 = \frac{2\omega_{eg}^3 e^2}{3\epsilon_0 hc^3} \frac{R^2_{n'l',nl}}{2l'+1}. \tag{2.30}$$

For the nS and nD alkali Ryberg states here investigated, the lifetimes are several microseconds long. The radiative lifetime increases as n or l increases and can be accurately calculated [71] using the empiric formula:

$$\tau = \tau' n^{*\gamma}. \tag{2.31}$$

The lifetime of Rydberg atoms can be also limited by thermal radiation so the black body correction has to be taken into account:

$$\frac{1}{\tau^T} = \frac{1}{\tau} + \frac{1}{\tau_{bb}}, \tag{2.32}$$

where $1/\tau_{bb}$ is the back body radiation induced decay rate [34]:

$$\frac{1}{\tau_{bb}} = \frac{4\alpha^3 k_B T}{3(n^*)^2}, \tag{2.33}$$

with α the fine structure constant. Values of τ' and γ are presented in table (2.2)

Table 2.2: Lifetime parameters for Rb atoms [34].

Parameter	s	p	d	f
τ' (ns)	1.43	2.76	2.09	0.76
γ	2.94	3.02	2.85	2.95

2.2.4 Rydberg Atoms in Electric Fields

Rydberg atoms are sensitive to electric fields. The large separation between an electron and its positive core is responsible for the weak binding energy. Therefore, to ionize Rydberg atoms relatively weak electric fields are needed. This sensitivity is used in the detection system where excited atoms are ionized and then pushed toward a detecting device. The ionization and the detection of Rydberg atoms is described in more details in chapter 4 and chapter 5. Atoms other than hydrogen can be described using the hydrogen approach. However, the important differences should be kept in mind. In zero electric field the ionic core depresses the energy of the levels with low l. To quantitatively treat the problem of an atom in electric field, a perturbative approach is used with the perturbation term for an electric field of a strength F in z-direction $V = ezF$. The perturbation treatment of the energy of states n gives:

$$E_n = E_n^{(0)} + \left\langle n^{(0)} \left| V \right| n^{(0)} \right\rangle + \sum_{k \neq n} \frac{| \left\langle n^{(0)} \left| V \right| n^{(0)} \right\rangle |^2}{E_n^{(0)} - E_k^{(0)}} + ..., \tag{2.34}$$

where the second order term is summed over all unperturbed states $\left| k^{(0)} \right\rangle$. Atomic states with distinct parity don't have a permanent dipole moment therefore, there is no energy correction for the first order. Degenerate states however, with different parity can mix and form states with the permanent dipoles. This dipole moment can then interact with the applied electric field. Therefore, the Stark effect can be observed. One can distinguish two types of Stark effect, first and second order. The first order results in a linear shift of the energy levels and it happens for degenerate hydrogen-like states. As presented in the textbook by Gallagher [34], the defect states, as those we are dealing with in the alkali atoms, show the second order Stark effect which is quadratic and can be calculated using:

$$\Delta E_{st} = -\frac{1}{2} \left[\alpha_0 + \alpha_2 \frac{3m_J^2 - J(J+1)}{J(2J-1)} \right] F^2, \tag{2.35}$$

where α_0 and α_2 are the scalar and tensor polarizabilities, the F is the applied electric field and J stands for the angular momentum with its projection along the quantization axis. The sign of the quadratic shift is determined by the sign of the detuning to the closest state due to the energy denominator in equation (2.34). The Stark shift in rubidium atoms varies for different l-levels. For S-states th energy shift is always negative [61], while for D-state positive polarizabilities were also observed [38]. An important feature of non-hydrogen alkali atoms is the avoided crossing between Stark levels of two different n-states.

2.2.5 Dipole-Dipole Interaction

During experiments with Rydberg atoms, the electric field is used to ionize the atoms or to induce a permanent dipole moment. When the electron cloud is shifted with respect to the nucleus atoms gain a dipole moment. Dipole-dipole interactions are the result of the interactions between two atoms or molecules with permanent dipole moments. To describe the dipole-dipole interaction let us consider a system consisting of two atoms A (core A$^+$ and electron 1) and B (core B$^+$ and electron 2), as in figure 2.5. These atoms are separated by the distance $\vec{R}$. The

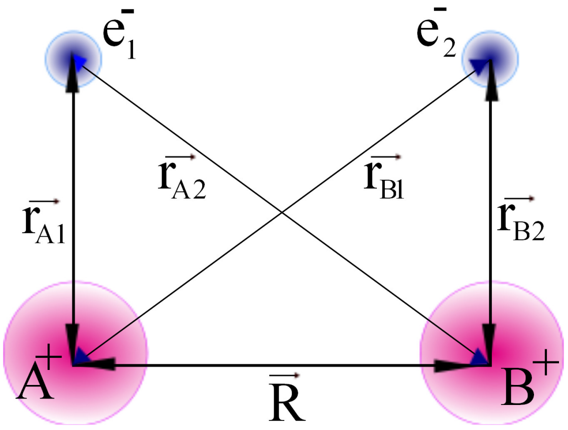

Figure 2.5: Two excited atoms: A (core A^+ and electron 1) and B (core B^+ and electron 2) at the distance R.

Hamiltonian describing this system is:

$$H = H_{OA} + H_{OB} + V_{int} + V_{dd}, \tag{2.36}$$

where H_{OA} and H_{OB} are the terms describing electrons of atoms A and B, and V_{int} determines the Coulomb interaction terms between two atoms :

$$V_{int} = \frac{e^2}{\left|\vec{R}\right|} - \frac{e^2}{|\vec{r_{A_2}}|} - \frac{e^2}{|\vec{r_{B_1}}|} + \frac{e^2}{|\vec{r}|}, \tag{2.37}$$

here $\vec{R} = \vec{AB}$ is the distance between atom A and atom B, $\vec{r_{A_2}}$ is the distance between atom A and the excited electron of atom B and $\vec{r_{B_1}}$ is the distance between atom B and the excited electron of atom A.

$$\vec{r}_{A_2} = \vec{R} + \vec{r}_{B_2}, \tag{2.38}$$

$$\vec{r}_{B_1} = \vec{R} + \vec{r}_{A_1}, \tag{2.39}$$

$$\vec{r} = \vec{R} - \vec{r}_{B_1} + \vec{r}_{A_2}. \tag{2.40}$$

Then the interaction term of the Hamiltonian V_{dd} is described by the dipole-dipole interaction

$$V_{dd} = \frac{1}{4\pi\epsilon_0 R^3}(\vec{\mu_A} \cdot \vec{\mu_B} - 3(\vec{n} \cdot \vec{\mu_A})(\vec{n} \cdot \vec{\mu_B})), \tag{2.41}$$

where $\vec{n} = \frac{\vec{R}}{R}$ is the interatomic operator and $\vec{\mu_A}$ and $\vec{\mu_B}$ are the atomic dipoles. Due to the long range interaction electron 1 is always close to core A and electron 2 to core B.

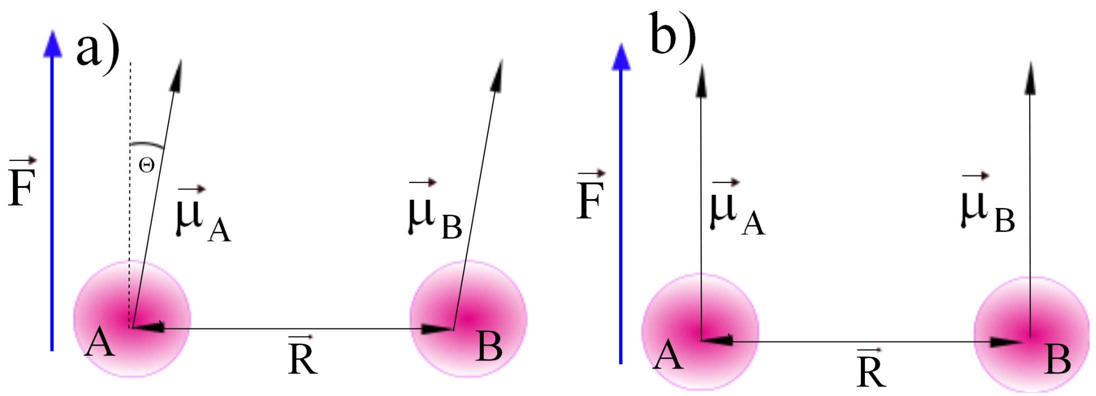

Figure 2.6: (a) Two excited atoms A and B separated by a distance R in the presence of an electric field $\vec{F}$ with an angle θ between the vector of the electric field and the dipole moment of atom and (b) with the dipole moments μ_A andμ_B along the direction of the electing field $\vec{F}$.

If we apply an electric field, the atoms may create a permanent dipole along the direction of the applied field $\vec{F}$. If this external field $\vec{F}$ results stronger than all other fields, for example the sum of the fields created by the dipoles, all dipoles are aligned along the same field $\vec{F}$:

$$\frac{1}{2}\alpha\vec{F} = \vec{\mu}, \tag{2.42}$$

where α is the polarizability. Then V_{dd} will take the form

$$V_{dd} = \frac{\vec{\mu_A} \cdot \vec{\mu_B}}{4\pi\epsilon_0}\frac{1}{R^3}(1 - 3\cos^2\Theta), \tag{2.43}$$

where Θ is the angle between the vector of the electric field and the dipole moment of atom A. The schematic picture of atom A and B in the presence of the electric field $\vec{F}$ is shown in figure (2.6). The $(1 - 3\cos^2\Theta)$ dependence was observed in Noel's group [16]. In figure (2.7) the interaction between two dipoles are shown. Dipoles placed side to side repel each other and dipoles aligned head to tail attract.

The amplitude of dipole-dipole interaction is typically written in the form

$$V_{dd} = \frac{C_3}{R^3}, \tag{2.44}$$

with the C_3 coefficient determining the interaction amplitude. C_3 increase with the quantum number and obeys a rapid $(n^*)^4$ scaling as in ref. [22].

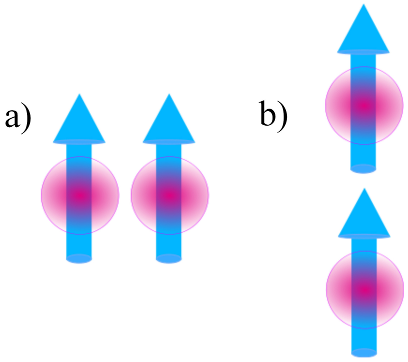

Figure 2.7: Dipoles placed "side by side" repel each other, the one "head to tail" attract.

In absence of a permanent dipole, the energy shift constitutes the distance dependent potential curve between Rydberg atoms that is given by:

$$\hbar\tilde{\Delta}(R) = \frac{\hbar\Delta}{2} - sign(\hbar\Delta)\sqrt{\frac{\hbar\Delta^2}{4} + \frac{C_3^2}{R_6}}, \tag{2.45}$$

where Δ is the energy mismatch of the energy transfer process. The cross over can be defined as a distance at which the energies transition from Van der Waals into dipole dipole form and is gen by:

$$\hbar\Delta = \frac{C_3}{R_{VdW}^3}. \tag{2.46}$$

Therefore we can conclude that for short distance $R << R_{VdW}$ the energy shift takes form :

$$\hbar\tilde{\Delta} = \frac{C_3}{R^3}, \tag{2.47}$$

which is the largest possible interaction energy between two Rydberg atoms.

In the case of long distance tail $R >> R_{VdW}$ when only one nearby energy level dominates, the energy shift takes form:

$$\Delta E = \frac{(C_3/R^3)^2}{\hbar\Delta} = \frac{C_6}{R^6}, \tag{2.48}$$

with the C_6 coefficient determining the interaction amplitude. Also C_6 increase with the quantum number and obeys a more rapid $(n^*)^{11}$ scaling as in ref. [22].

2.2.6 Dipole Blockade

Dipole-dipole interactions between Rydberg atoms give rise to a phenomenon called dipole blockade. The blockade of excitation to the Rydberg state occurs when dipole-dipole interactions take place and shift the energy levels. The blockade effect has been observed for cold atoms [22], and several similar phenomena has been observed for electrons [32] and photons [7]. In dipole blockade, the laser excitation of cold Rydberg atoms ground and Rydberg states are coupled by a laser with a Rabi frequency Ω. When two atoms are in the same excited state, the strong interaction between them (due to their large electric dipoles) causes a symmetrical energy shift ΔE. If this shift becomes bigger then Ω, only one atom can undergo excitation to the Rydberg state [73, 33]. In other words, the probability of excitation from the ground levels to the Rydberg levels decreases thanks to the interaction with an already excited atom. If the interaction energy becomes larger than the Rabi frequency and the laser resolution, the excitation laser frequency is out of resonance with the shifted state. Then only one atom at a time can be excited to the Rydberg state. The dipole blockade effect will be studied in two extreme regimes: pairs of Rydberg atoms and dense atomic clouds.

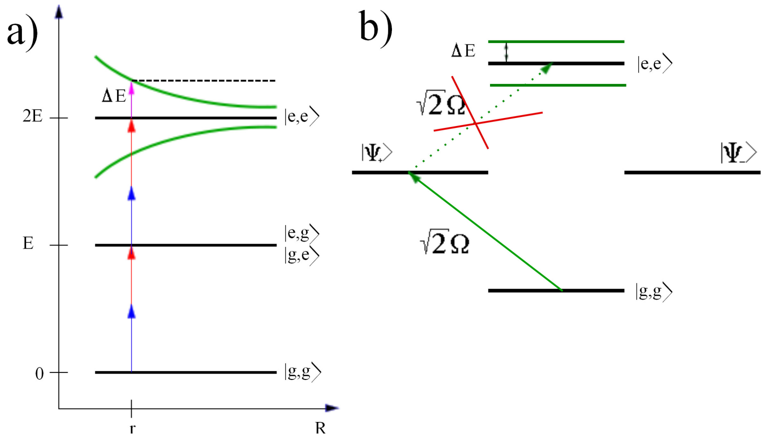

Figure 2.8: (a) Principle of the Rydberg blockade between two atoms separated by a distance R. The ground state $|g, g\rangle$ is coupled to the excited state $|e, e\rangle$ with a Rabi frequency Ω. The strong interaction between the two atoms causes a shift in the level energy. when this shift is larger than $\hbar\Omega$ the blockade effect occurs. (b) Two-level atom approach is used to described atoms in the blockade regime. The atoms are described by the two level system. The $|\Psi_+\rangle$ is coupled only with $|g, g\rangle$ states, where $|\Psi_-\rangle$ is not coupled to neither of $|g, g\rangle$ and $|r, r\rangle$ states.

First lets consider a pair of Rydberg atoms. In this situation one can either excite the two atoms individually or collectively. Conditional excitation refers to the situation when atoms are addressed individually. During collective excitation one addresses both atoms at the same time. The principle of the dipole blockade is indicated in figure (2.8). The most important consequence of the dipole blockade is the fact that we are not able to indicate which of these two atoms carries the excitation. The two atoms end up entangled, with the wavefunction given by:

$$|\Psi_+\rangle = \frac{1}{\sqrt{2}}\left(|g,r\rangle\, e^{ikR_2} + |r,g\rangle\, e^{ikR_1}\right), \tag{2.49}$$

where R_1 and R_2 stand for the position of the two atoms and k for the wavevector. The antisymmetric wavefunction is given by

$$|\Psi_-\rangle = \frac{1}{\sqrt{2}}\left(|g,r\rangle\, e^{ikR_2} - |r,g\rangle\, e^{ikR_1}\right), \tag{2.50}$$

The coupling of $|g,g\rangle$ state with $|\Psi_+\rangle$ is $\sqrt{2}\Omega$ and coupling with $|\Psi_-\rangle$ doesn't exist, see figure (2.8). Therefore, two atoms taking part in the Rydberg excitation can be described by an effective two level system. If the decay rate of the Rydberg state, Γ, is smaller than the effective Rabi frequency, Ω'_{eff}, the blockade radius is defined by:

$$r_b \equiv \sqrt[6]{\frac{C_6}{\hbar\Omega'_{eff}}}. \tag{2.51}$$

The blockade radius describes the smallest volume in which only one atom can be excited into the Rydberg state.

The experiments presented in this thesis are conducted with samples of $\sim 10^5$ atoms and high densities ($\sim 10^{13}$ cm^{-2}). This means that the volume of a blockade sphere may not cover all the volume of the sample (depends on the state and therefore on the blockade radius). Thus the sample may contain up to several hundreds of atoms in the ground state and only a few in the Rydberg state. This fact changes the dynamics and now collective behavior has to be considered. The Hamiltonian that describes system of N interacting externally driven atoms is given by:

$$H^N = \sum_{j=1}^{N} H_j^s + \sum_{k<l} V_{kl}\frac{1}{2}(1+\sigma_z)_k\frac{1}{2}(1-\sigma_z)_l, \tag{2.52}$$

where V_{kl} stands for the interactions between atoms k and l, H_j^s is the single atoms Hamiltonian defined by:

$$H_j^s = \frac{\hbar}{2}\Omega(\sigma_x)_j + \frac{\hbar}{2}\Delta(\sigma_z)_j, \tag{2.53}$$

and σ_x and σ_z are the well know Pauli matrices. The indexes *j,k* and l describe The Hilbert subspace for respective atom. If the interaction are strong enough and only one atom can be excited, all states with more than one excitation can be neglected. The ground state of the system is described by:

$$\left|\Psi^{(N,0)}\right\rangle = \left|g_1, g_2, ..., g_N\right\rangle , \tag{2.54}$$

and the collective state with one excitation is given by:

$$\left|\Psi^{(N,1)}\right\rangle = \frac{1}{\sqrt{N}} \left|g_1, g_2, ..., e_i, ..., g_N\right\rangle . \tag{2.55}$$

where a constant phase factor was inserted for all components of the collective state. In reality atoms separated by more than one wavelength experience different phases of the excited light. This system can be again reduced to two-level system with $\left|\Psi^{(N,1)}\right\rangle$ and $\left|\Psi^{(N,0)}\right\rangle$ states. The transition is driven with collective Rabi frequency

$$\Omega_{coll} = \sqrt{N}\Omega. \tag{2.56}$$

Therefore this system of N atoms behaves like a single atom and can be called the *superatom*. The enhancement by $\sqrt{N}$ of Rabi frequency was already predicted by [27].

Chapter 3

Introduction to Bose Einstein Condensation and Optical Lattices.

A Bose Einstein Condensate (BEC) is the starting point of most of our investigations and it is used as a source of a phase coherent cold atoms. In 1995 the phase transition of a dilute gas of bosons to a BEC was observed by several groups [2, 26, 11]. The realization of a Bose Einstein Condensate was one final result of a decade long research on the cooling and trapping of atomic gases. In this chapter a review of some basics concepts about the theory of degenerate bosonic gases is shown. Then the techniques needed to optically cool and trap atoms are presented. Finally some theoretical and experimental concepts about optical lattices are described, as they are used as an important experimental tool in one of the later chapters of this thesis.

3.1 Bose Einstein Condensation in dilute alkali gases

Bose Einstein Condensation is a quantum phenomenon that results from the quantum statistics of identical particles with integer spin. A Bose Einstein Condensate (BEC) was predicted in 1925 by Albert Einstein [30, 31] on the basis of a work by Satyendranath Bose [10]. The achievement of a BEC provides unique opportunities to explore quantum phenomena using macroscopic samples. In this section the main ideas for the theoretical description of Bose Einstein Condensates are shown.

3.1.1 The non interacting Bose gas: statistical approach

A gas of non-interacting bosons at temperature T can be treated as a grand canonical ensemble with the number of atoms given by:

$$N = \sum_m \frac{1}{\exp(\beta(\epsilon_m - \mu)) - 1}, \tag{3.1}$$

where ϵ_m is the mth energy level, μ stands for the chemical potential, k_B is the Boltzmann constant and $\beta = (k_B T)^{-1}$. If the energy spectrum is considered to be a continuum the sum in equation 3.1 can be replaced by an integral resulting in:

$$N = \int_0^\infty \frac{g(\epsilon) d\epsilon}{\exp(\beta(\epsilon - \mu)) - 1}. \tag{3.2}$$

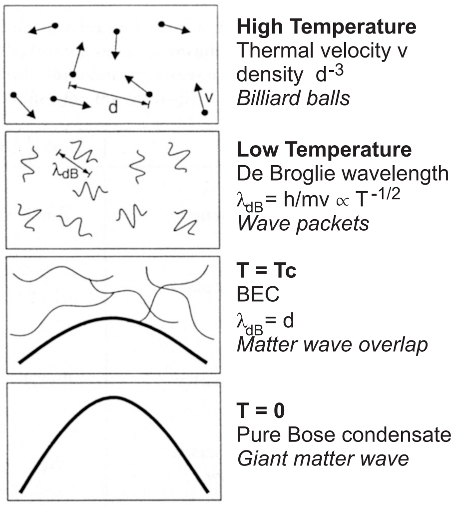

Figure 3.1: When the temperature of the gas is high enough, the quantum nature of the particles can be neglected and the system obeys Boltzmann statistics. With decreasing temperature, the De Broglie length increases and when it has the same order of magnitude as the inter atomic distance, the wave functions overlap [41].

In equation 3.2, $g(\epsilon)$ stands for the density of states and depends on the potential experienced by bosons. For a harmonic trapping potential it is given by:

$$g(\epsilon) = \frac{\epsilon^2}{2(\hbar\omega_{ho})^3}. \tag{3.3}$$

Magnetic and optical traps used in experiments on cold Bose gases can be approximated by the harmonic oscillator, whose energy spectrum is;

$$\epsilon_{n_x,n_y,n_z} = \left(n_x + \frac{1}{2}\right)\hbar\omega_x + \left(n_y + \frac{1}{2}\right)\hbar\omega_y + \left(n_z + \frac{1}{2}\right)\hbar\omega_z. \tag{3.4}$$

Therefore, $\omega_{ho} = (\omega_x \omega_y \omega_z)^{1/3}$ and stands for the mean trapping frequency. Below the critical temperature T_C the chemical potential is extremely close to zero, $\mu \approx 0$, [55]. the number of atoms, N_0, populating the lowest energy state, $\epsilon_{0,0,0}$ becomes a macroscopic fraction of the whole system. When this condition is fulfilled Bose Einstein condensation occurs. The number of atoms in the excited state is much smaller than the total number of atoms $N_{exc} << N$, where N_{exc} is described as a difference between the total number of atoms and the number of atoms in the ground state: .

$$N_{exc} = N - N_0 = \int_0^\infty \frac{g(\epsilon)d\epsilon}{exp(\beta\epsilon) - 1}. \tag{3.5}$$

Introducing equation (3.3) into equation (3.5) and solving the integral, one obtains:

$$N_{exc} = N - N_0 = \zeta(3)\left(\frac{k_B T}{\hbar\omega_{ho}}\right), \tag{3.6}$$

where $\zeta(\cdot)$ is the Riemann function with $\zeta(3) \cong 1.2$. The gas becomes a thermal Bose gas when its temperature is above the critical value T=T$_c$ such that $N_0 << N$. This value can be calculated by imposing N_0=0 into equation (3.6):

$$k_B T = \hbar\omega_{ho}\left(\frac{N}{\zeta(3)}\right) \cong 0.94\hbar\omega_{ho}N^{1/3}. \tag{3.7}$$

This equation shows that for a large enough number of atoms, N, the critical temperature is much larger than the energy level separation: $k_B T_C / (\hbar\omega_{ho}) \cong 0.94N^{1/3} >> 1$. In this case Bose Einstein condensation can be obtained experimentally with the use of cold bosonic gases confined in harmonic potentials. For temperatures below T$_c$ the numbers of atoms in the ground state increases and from equation (3.1) and equation (3.6) the fraction of condensed atoms can be evaluated as:

$$\frac{N_0}{N} = 1 - \left(\frac{T}{T_c}\right)^3. \tag{3.8}$$

During the experiments this behavior is clearly visible in the different widths of the momentum distribution of the atoms in the condensate fraction and those in the thermal cloud. The thermal cloud follows the Boltzmann distribution while the condensate is described by the wave function of the ground state of the harmonic trap. The wave function of the condensed gas is then given by:

$$\phi_0(\vec{r}) = \left(\frac{m\omega_{ho}}{\pi\hbar}\right)^{3/4} \exp\left(-\frac{m}{\pi\hbar}\left(\omega_x x^2 + \omega_y y^2 + \omega_z x^z\right)\right). \tag{3.9}$$

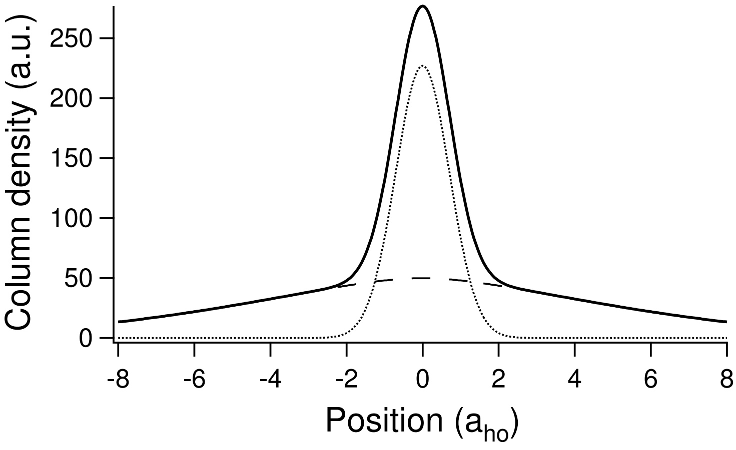

Figure 3.2: Column density as a function of the position for a non-interacting Bose gas at $T = 0.95T_C$. The dotted line represents the density of the condensate fraction, the dashed line shows the density of the thermal fraction and the continuous line is the total density.

If the confining potential is switched off when the temperature is between 0 and T$_c$ the distribution of the condensed and thermal part is different. The atoms in the thermal cloud are characterized by the Gaussian distribution with a larger width. The width of the BEC is narrower than in the thermal cloud case. From these Gaussian widths the temperature of the atoms can be calculated. More details about Bose Einstein condensation can be found in [25, 63].

3.1.2 The interacting Bose gas: mean field theory

Up to this point the non-interacting gas was taken into account but in the case of weakly interacting atoms a different theoretical approach is needed. The many body Hamiltonian describes a system of N interacting particles in a potential V$_{ext}$:

$$\hat{H} = \int d\vec{r}\hat{\Psi}^{+}(\vec{r}) \left[-\frac{\hbar^2}{2m} + V_{ext}\right] \hat{\Psi}(\vec{r}) + \frac{1}{2}\int d\vec{r}' d\vec{r}\hat{\Psi}^{+}(\vec{r})\hat{\Psi}^{+}(\vec{r'})V(\vec{r}-\vec{r'})\hat{\Psi}(\vec{r})\hat{\Psi}(\vec{r}'), \tag{3.10}$$

where $V(\vec{r}-\vec{r'})$ is the inter-particle interaction potential and $\hat{\Psi}^2(\vec{r})$ is the boson field operator that annihilates or creates a particle at the position $\vec{r}$. This operator can be written as:

$$\hat{\Psi}(\vec{r}) = \sum_{\alpha} \Psi_{\alpha}(\vec{r})\hat{a}_{\alpha}, \tag{3.11}$$

where $\Psi_\alpha(\vec{r})$ is the single particle wave function of the α-th energy level, and $\hat{a}_\alpha$ is the corresponding boson annihilation operator. This equation can be simplified using mean field approximations. The condensate part $\hat{\phi}(\vec{r},t)$ is separated from the bosonic operators:

$$\hat{\Psi}(\vec{r},t) = \hat{\phi}(\vec{r},t) + \hat{\Psi}'(\vec{r},t). \tag{3.12}$$

When the temperature of the system is below T$_c$, the number of atoms in the ground state is very large. Therefore, an addition or subtraction of one atom from the system does not significantly changes the populations. For these reasons we can treat $\phi(\vec{r},t)$ as a complex function and equation (3.12) can be written as:

$$\hat{\Psi}(\vec{r},t) = \phi(\vec{r},t) + \hat{\Psi}'(\vec{r},t), \tag{3.13}$$

where the wavefunction of the condensate is defined as $\phi(\vec{r},t) \equiv \left\langle \hat{\Psi}(\vec{r},t) \right\rangle$ and the condensate density is:

$$n_0(\vec{r},t) = |\phi(\vec{r},t)|^2 . \tag{3.14}$$

The boson field operator in equation (3.13) is written in the Heisenberg picture, so it can be directly written in the Heisenberg equation:

$$i\hbar\frac{\partial}{\partial t}\hat{\Psi}(\vec{r},t) = \left[\hat{\Psi},\hat{H}\right] = \left(-\frac{\hbar^2\nabla^2}{2m} + V_{ext}(\vec{r}) + \int d\vec{r'}\hat{\Psi}^{+}(\vec{r'},t)V(\vec{r'}-\vec{r})\hat{\Psi}(\vec{r'},t)\right)\hat{\Psi}(\vec{r},t). \tag{3.15}$$

Assuming a dilute gas, the interaction term is just the two body scattering and the interaction potential can be written as:

$$V(\vec{r'}-\vec{r}) = \frac{4\pi\hbar^2 a_s}{m}\delta(\vec{r'}-\vec{r}), \tag{3.16}$$

where a_s is the s-wave scattering length. Moreover, if in equation 3.13, $\hat{\Psi}'(\vec{r},t)$ is small, then the operator $\hat{\Psi}(\vec{r},t)$ can be replaced by the complex function $\phi(\vec{r},t)$ [25, 63]. In this way equation (3.15) becomes the *Gross Pitaevskii Equation*:

$$i\hbar\frac{\partial}{\partial t}\phi(\vec{r},t) = \left(-\frac{\hbar^2\nabla^2}{2m} + V_{ext}(\vec{r}) + g\left|\phi(\vec{r},t)^2\right|\right)\phi(\vec{r},t), \tag{3.17}$$

where$g$ is given by

$$g = \frac{4\pi\hbar^2 a_s}{m} \tag{3.18}$$

p The Gross Pitaevskii Equation is Schr$\ddot{o}$dinger equation with a nonlinear interaction term. It is valid when the total number of atoms is much larger than 1, and if scattering length is much smaller than the mean distance between atoms.

3.2 Laser Cooling

This thesis work based on the excitation of Rydberg atoms from ultracold atomic samples. To obtain a source of such atomic ensembles one needs to find methods to cool down the atoms. The Laser cooling, first mentioned by Hänsch and Schawlow[37] and by Lethokov[3]: in the seventies is based on the interaction between atoms and laser light. The development of laser cooling techniques was an important step towards the realization of the Bose Einstein Condensate. In this section the Doppler and Sub-Doppler laser cooling methods are presented.

3.2.1 Doppler Cooling

The first idea of laser cooling was to exploit light absorption and the Doppler effect due to a motion of atoms [37]. A two level atom absorbing a photon gets a momentum kick in the direction of the photon propagation axis. The atoms spontaneously reemit a photon in a random direction, obtaining a recoil in the direction opposite to the direction of the photon. If the difference between the frequency of the irradiating light ω_L and the atom transition frequency ω_0 is negative

$$\Delta = \omega_L - \omega_0 < 0 \tag{3.19}$$

the laser is *red detuned* and an atom has maximum probability to absorb a photon when it moves in the opposite direction with respect to the laser beam propagation, since the Doppler effect shifts the laser frequency closer to the atomic transition frequency. The velocity of the atom is decreased by gaining momentum in the direction opposite to its motion. While considering the absorption of several photons and their following emissions, one gets a momentum kick per cycle in the direction of the incoming photon. This idea can be considered in a more rigorous treatment, when one takes into account the radiation pressure by solving the optical Bloch equations [57]. For small detuning ($\Delta << \omega_0$) a process of absorption and spontaneous emission on one atom changes its momentum by:

$$\delta p = \hbar \vec{k} \left(1 - \cos(\theta)\right), \tag{3.20}$$

where $\vec{k}_L = k_L \hat{z}$ is the wavewector and θ is random. Therefore, by averaging over θ and deriving from the Bloch equation solution the number of spontaneous emission processes per unit time, the force acting on atoms can be written as:

$$F = \hbar k \frac{\Gamma \Omega_R^2/4}{\Delta^2 + \Gamma^2/4 + \Omega^2/2}, \tag{3.21}$$

where Γ is the natural linewidth of the excited atomic state and Ω_R the Rabi frequency. Considering the case of two counterpropagating beams, the total force is a sum of the forces acting on the atoms. The detuning Δ has to be replaced by $\Delta \pm k_L v$ to take into account the Doppler shift, where v is the velocity of the atom. One then finds:

$$\vec{F} = \vec{F}_+ + \vec{F}_- \approx \hbar k_L^2 \Gamma \Delta \frac{\Omega^2 R}{(\Gamma^2/4 + \Delta^2)} = -\gamma v_z \hat{z}. \tag{3.22}$$

For the red detuning, i.e. $\Delta < 0$ equation (3.22) states that the laser fields work as a viscous medium for the atom. Such a system is know as an *optical molasses* [18]. The theoretical lowest temperature achievable in an optical molasses is:

$$k_B T_D = \frac{1}{2}\hbar\Gamma, \tag{3.23}$$

and is usually referred to the Doppler temperature.

3.2.2 Sub-Doppler Cooling

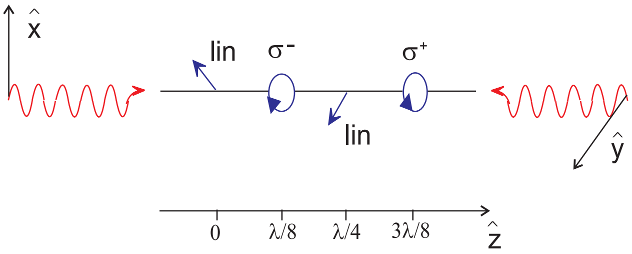

Figure 3.3: Polarization scheme for the $lin \perp lin$ configuration.

Although using the Doppler cooling one can cool samples down to temperatures on the order of hundreds of microKelvins, the temperatures far below than that are needed to achieve a Bose Einstein condensation. The next step in the quest for condensation is constituted by the sub-Doppler cooling mechanisms where temperatures lower than the Doppler cooling are realized experimentally [48]. The explanation for this behavior was found by treating the atom-light interaction in dressed atom model of chapter 2. Sub-Doppler cooling was then explained by taking into account the internal structure of an atom and the presence of polarization gradients. This process is usually called *Sisyphus cooling* and can be easily understood in the case of two counterpropagating laser beams in the $lin \perp lin$ configuration, where beams have mutually orthogonal polarization. In this case the laser light carries the overall electric field given by:

$$\vec{E}(\vec{r},t) = E_0 \hat{x} \cos(\omega_L t - k_L z) + E_0 \hat{y} \cos(\omega_L t - k_L z) \tag{3.24}$$

$$= E_0 \left[(\hat{x} + \hat{y}) \cos \omega_L t \cos k_L z + (\hat{x} - \hat{y}) \sin \omega_L t \sin k_L z \right]. \tag{3.25}$$

Considering an atom with total angular momentum J$_g$=1/2 for the ground state and J$_e$=3/2 for the excited one (see figure 3.4), the two Zeeman sublevels of the ground state have different energies depending on the local polarization of the laser field. These two states cross when the local polarization is linear. When an atom is in a higher sublevel it has a maximum probability to experience a photon absorption. Every time an atom spontaneously decays to the lower sublevel after absorption, it loses the kinetic energy that it used to climb the potential hill corresponding to the difference in energy between the two ground sublevels. This process repeats during the motion of the atom.

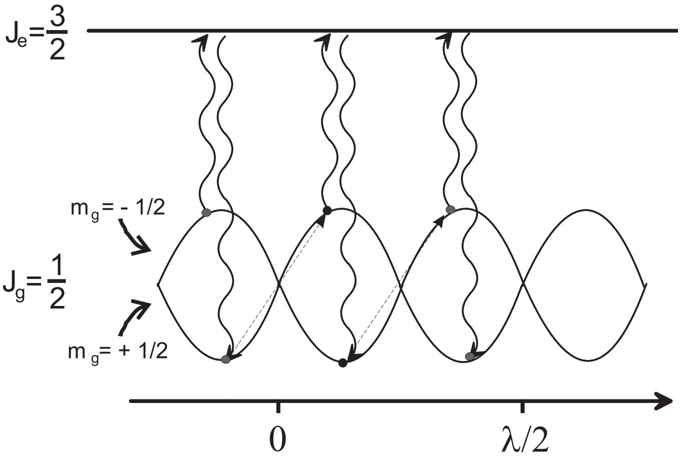

Figure 3.4: Energy of the ground state sub levels of a J$_g$ =1/2 atom in a $lin \perp lin$ laser field configuration.

This sequence when averaged in time causes a cooling of the gas below the Doppler limit. The steady state kinetic energy is on the order of a few times the recoil energy:

$$E_{rec} = \hbar^2 \frac{k_L^2}{2m}, \tag{3.26}$$

where k$_L = 2\pi/\lambda$ is the light wavevector. For example, the possible achieved temperature in ^{87}Rb is on the order of 1 μK.

3.3 The Magneto Optical Trap

Cooling in optical molasses is based on the dependence of the detuning seen by the atoms on their velocity, see equation 3.25. Atoms inside three dimensional molasses are not spatially confined. To trap these atoms a good strategy is to make this detuning dependent on the spatial position of the atoms. To do this a

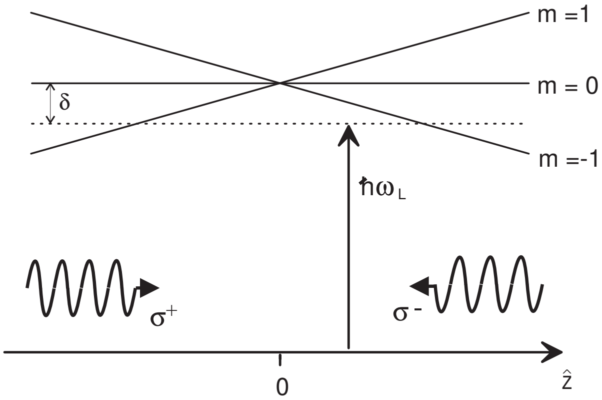

Figure 3.5: Principle of 1D MOT for a F=0→F'=1 transition. The inhomogeneous magnetic field induces a space-dependent shift of Zeeman sublevels, producing a space-dependent force on the atoms.

magnetic gradient b' can be used. In a one dimensional system this corresponds to having a magnetic field varying in space: $\vec{B} = b'z\hat{x}$. The magnetic field shifts the Zeeman sub-levels of the excited state by:

$$\Delta E_z = \mu_B g_F m_F b' z, \tag{3.27}$$

where μ_B is the Bohr magneton, g$_F$ is the Landé factor and m$_F$ stands for the z component of the angular momentum. Assuming that the two counterpropagating beams have a circular polarization $\sigma^{\pm}$ and that they create an optical molasses along axis z, the detuning of these beams become:

$$\Delta \mp \gamma v_z \mp \mu_B g_F m_F b' z/\hbar. \tag{3.28}$$

To understand how trapping occurs, one can consider atoms to have a ground state with total angular momentum J$_g$=0 and an excited state with J$_e$=1. The molasses laser beams are resonant to the m_J=0→m_J=1 transition for $z < 0$ and the m_J=0→m_J=-1 transition for $z > 0$. In the case of circular polarizations σ^+ and σ^-, the atoms absorb photons only when they are far from B=0 position, and only from the molasses beam that is counterpropagating with respect to their motion, see figure (3.5). In the three dimensional system with three counterpropagating pairs of laser beams, force acting on atoms is given by, see figure (3.6):

$$\vec{F} = -\left(\gamma v + m\omega^2 \vec{r}\right), \tag{3.29}$$

where

$$\gamma = -\hbar k_{L^2} \Gamma \Delta \frac{\Omega_r}{(\Gamma^2/4 + 2\Delta)^2} \omega^2 = \frac{\mu_{g_F} m_F b'}{m\hbar k_L} \gamma. \tag{3.30}$$

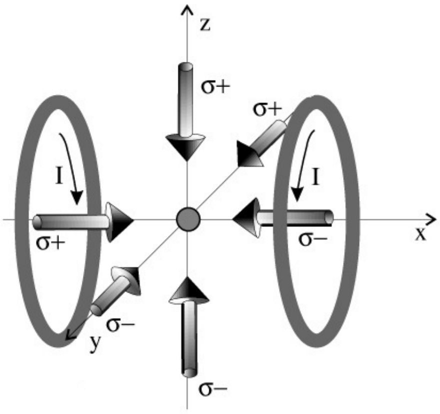

Figure 3.6: Laser beams and magnetic coils configuration in a standard 3D MOT.

The atoms are then trapped around B=0 point and this trapping is called Magneto-Optical trapping.

3.4 Evaporative Cooling

Bose Einstein condensation requires cooling samples to temperatures not achievable with an optical molasses. The technique used to cool atoms to the regime where Bose Einstein condensation is possible is called the evaporative cooling [56]. The idea of an evaporative cooling is to expel atoms with the highest energy from the whole system. This is achieved by cutting the edges of the thermal velocity distribution as presented in figure 3.7.

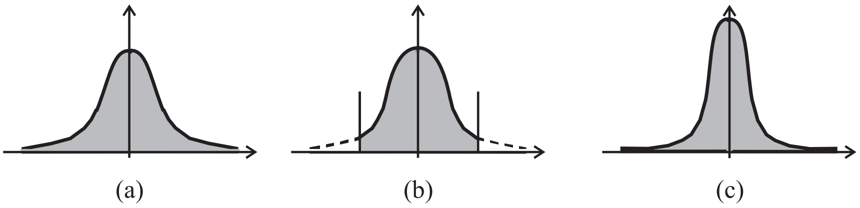
(a) (b) (c)

Figure 3.7: In the evaporative cooling process the tail of the thermal velocity distribution of the atoms is cut by expelling the atoms with the highest energy, see (b). (c) The system then re-thermalizes and and the final temperature is lowered.

The evaporation is applied by lowering the edges of the confining potential and letting the hottest atoms leave the trap. In our experiments evaporative cooling is done in magnetic and optical traps. To obtain an efficient cooling procedure with a minimum loss rate, the energy of the system must vary sufficiently slowly compared to the timescale of the thermalization process. The latter depends on the elastic collision rate, so dense samples are needed if one wants to achieve fast evaporation.

3.5 The magnetic Trap

In order to implement evaporative cooling with cold atoms, one needs conservative traps and the possibility to cut the high-energy tail of the atomic momentum distribution. In our experiment we used two different magnetic traps.

- **The quadrupole trap.** Trapping with the quadrupole trap is the easiest method of trapping atoms without using light assisted methods. A spherical quadrupole field creates a magnetic gradient which results in a field:

  $$\vec{B} = 2b'z\hat{z} - b'y\hat{y} - b'x\hat{x}, \tag{3.31}$$

  where $\hat{z}$ is called the strong axis because of the factor 2. The potential seen by a particle with magnetic moment $\vec{\mu}$ in a magnetic field $\vec{B}$ is given by:

  $$U = -\vec{\mu}\vec{B}, \tag{3.32}$$

  and the energy of the atoms is then described by an equation similar to equation (3.27):

  The atoms are confined in a local energy minimum. For $g_F m_F > 0$ (weak field seeking states) this requires a local magnetic field minimum. The states that are strong field seeking ($g_F m_F < 0$) cannot be trapped by static magnetic fields due to Maxwell equations not allowing a maximum of a magnetic field in a free space. The modulus and orientation of the field seen by the atoms in motion change continuously. The magnetic dipole of these atoms must follow the magnetic field in order to avoid spin flips (*Majorana spin flips*) that would cause transitions to untrapped Zeeman states. The condition that has to be satisfied in order to avoid this behavior is:

  $$\frac{d\theta}{dt} < \frac{\mu B}{\hbar} = \omega_{Lar}, \tag{3.33}$$

  where θ is the orientation of the magnetic field B and ω_{Lar} is the frequency of rotation of the atomic magnetic moment around the direction of the magnetic field, called the Larmor frequency. In the region where B=0, ω_{Lar}=0 and the condition presented above cannot be satisfied and spin flips result in loss of atoms from the trap.

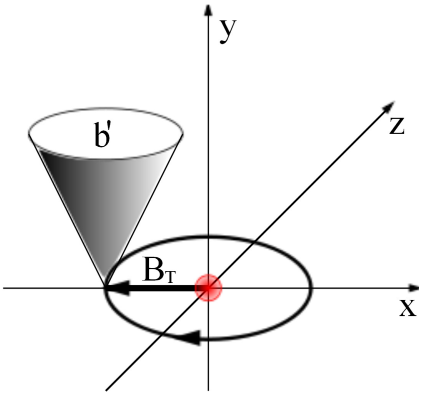

Figure 3.8: The TOP trap. A rotating magnetic field causes a continuous displacement of the B=0 point in order to avoid spin flip losses at the center.

- **The TOP Trap.** A time-averaged orbiting potential (TOP) was introduced in ref. [64] in order to solve the problem of Majorana spin flips at the center of a quadrupole magnetic trap. Those losses are avoided by the use of a rotating magnetic bias field B_{TOP} added to the quadrupole magnetic field, see figure (3.8). This time-dependent magnetic field creates a time-averaged minimum of the effective potential acting on the atoms. The bias field is given by:

  $$\vec{B_{TOP}} = B_0 \left[\hat{x} \sin(2\pi\Omega_{TOP}) + \hat{z} \cos(2\pi\Omega_{TOP})\right], \tag{3.34}$$

  where the rotation frequency Ω_{TOP} is chosen to be smaller than ω_{Lar} to maintain the atomic magnetic moment aligned with the total field. If the motion of the atoms is much slower than the movement of the magnetic field point, the potential felt by atoms then corresponds to the instantaneous potential integrated over time:

  $$U(x,y,x) = \int_{t=2\pi/\Omega_{TOP}} U(x,y,x,y)dt. \tag{3.35}$$

  The shape of the integrated potential is, close to its minimum, parabolic, with its minimum $B_{min} \neq 0$, and with average frequency given by:

  $$\omega_{ho} = (\omega_x \omega_y \omega_z)^{1/3} = \frac{b'}{\sqrt{B_{TOP}}} \sqrt{\frac{\mu}{m}}. \tag{3.36}$$

3.6 The Optical Dipolar Trap

The second stage of evaporative cooling is implemented in an optical trap. The optical dipole trap (further called dipole trap) uses the dipole force that emerges when atoms are irradiated by a laser light [36]. The laser light has to be far detuned from the atomic transition of the sample in order to avoid photon scattering. The dipolar force is created due to the electric field carried by light:

$$\vec{E}(\vec{r},t) = \vec{E}_\omega e^{-i\omega t} + \vec{E}_{-\omega} e^{i\omega t}. \tag{3.37}$$

In equation (3.37) the classical field $\vec{E}_\omega e^{-i\omega t}$ represents the absorption of a photon in a quantum mechanical treatment. The field $\vec{E}_{-i\omega} e^{\omega t}$ instead corresponds to the photon emission. The irradiated atoms experience a potential acting on them given by:

$$U = -\vec{d} \cdot \vec{E_\omega}, \tag{3.38}$$

where $\vec{d}$ stands for the atomic electric dipole. Due to this potential the ground state of the atoms changes as:

$$\Delta E_g = \sum_e \langle g| \vec{d}\vec{E}_\omega |e\rangle \frac{1}{E_g - E_e + \hbar\omega} \langle e| \vec{d}\vec{E}_{-\omega} |g\rangle \,, \tag{3.39}$$

where the sum is over all the excited states. Equation (3.39) after some calculation becomes:

$$\Delta E_g = -\frac{1}{2}\alpha(\omega) \left\langle E^2(\vec{r},t)\right\rangle_t, \tag{3.40}$$

where $\langle\cdot\rangle_t$ refers to a time average and $\alpha(\omega)$ stands for the atomic polarizability given by:

$$\alpha(\omega) = \sum_e \frac{2(E_e - E_g) \left|\langle e| \vec{d}\hat{\epsilon} |g\rangle\right|^2}{(E_e - E_g)^2 - (\hbar\omega)^2} \tag{3.41}$$

The ground state energy changes due to the presence of the effective potential $V_{eff} = \Delta E_g$ causing a force on the atoms:

$$\vec{F} = -\nabla V_{eff} = -\frac{1}{2}\alpha(\omega) \left\langle \nabla E^2(\vec{r},t)\right\rangle_t. \tag{3.42}$$

The dipolar force, attractive when $\hbar\omega < E_e - E_g$, i.e. the laser light is red detuned, and repulsive when $\hbar\omega > E_e - E_g$, i.e. the optical field is blue detuned, relies on an spatially inhomogenous laser intensity. This description ignores the

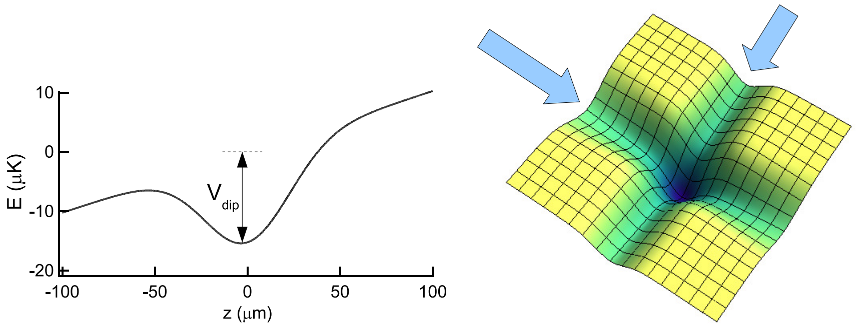

Figure 3.9: On the left: Dipolar confinement along the gravity (z) direction created by a laser beam. On the right: Dipolar confinement on the XY plane created by two crossed laser beams.

effect of spontaneous emission and it is valid when the detuning of the laser light is much bigger then the spontaneous decay rate:

$$|\Delta| = |\hbar\omega - (E_e - E_g)| >> (E_e - E_g). \tag{3.43}$$

In this case atoms are excited to the virtual energy levels and then decay by stimulated emission. The heating of the sample can be neglected because of the absence of spontaneous emission. Therefore, a red detuned Gaussian laser beam creates a trap for the atoms. This trap is usually called the *dipolar trap* has a depth that can be expressed in terms of an equivalent temperature T_{dip} in Kelvin:

$$T_{dip} = \frac{\hbar\Gamma^2}{\pi\Delta I_{sat} k_B} \frac{P}{w_0^2}, \tag{3.44}$$

where P is the power of the laser beam and w_0 stands for its waist. The radial frequency of the dipolar trap is described by:

$$\omega_{dip} = \sqrt{\frac{2\Gamma^2\hbar}{\pi|\Delta| m I_{sat}} \frac{\sqrt{P}}{w_0^2}}. \tag{3.45}$$

3.7 Optical lattices

Section (3.6) presented our application of the dipole force for trapping and applying evaporative cooling. By going one step further one can make this force periodic. In this way new applications such as investigation of the BEC phase, are available. Periodic potentials have been studied extensively in the physics of electrons in crystals. Since some of the experiments presented in this thesis were performed on Bose Einstein Condensates loaded into periodic potentials, in this section tools used for the experimental realization and calibration of optical lattices are briefly discussed.

3.7.1 The standing wave

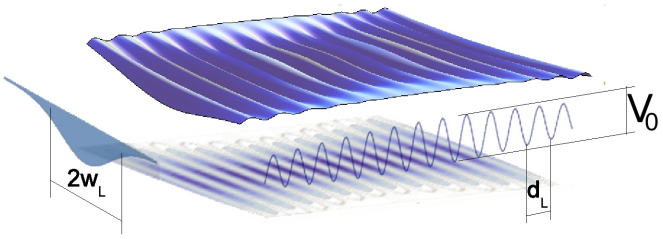

Figure 3.10: The periodic potential created by two counterpropagating laser beams with lattice constant d_L and depth V_0. The radial Gaussian profile is due to the finite size of the laser beams.

A standing wave can be realized using counterpropagating linearly polarized laser beams of the same frequency ω_L. The electric field $\vec{E}$ generated by the light is given by:

$$\vec{E}(\vec{r},t) = E_0 \sin(k_L x + \omega_L t)\hat{e} + E_0 \sin(k_L x - \omega_L t)\hat{e} = 2E_0 \sin(\omega_L t)\sin(k_L x)\hat{e}, \tag{3.46}$$

where E_0 stands for the electric field amplitude and k_L for the wavevector. As explained in subsection (3.6) atoms in the presence of a wave feel an external potential. In the case of a standing wave these atoms feel a periodic potential. This potential depends on a square of $\vec{E}$ and can be written as:

$$V(x) = \frac{V_0}{2}\cos(2k_L x), \tag{3.47}$$

where V_0 is the depth of the optical lattice. The amplitude of this potential is given by:

$$V_0 = \xi\hbar\frac{I_p}{I_s}\frac{\Gamma_s}{\Delta}, \tag{3.48}$$

where I_p stands for the peak intensity of the laser beam, I_s is the saturation intensity, ξ stands for a correction depending on the level structure of the atom [36, 24] and d_L is the lattice spacing. The quantum mechanical approach takes into account the interaction between an atom and the photons of the lattice beams. This approach requires to define quantities related to the lattice starting from the recoil momentum $p_{rec} = \hbar k_L$. Therefore V$_0$ is measured in units of the recoil energy E$_{rec}$ introduced in equation (3.26). Other important quantities used are the recoil frequency $\omega_{rec} = E_{rec}/h$ and the recoil velocity $v_{rec} = p_{rec}/m$.

3.7.2 Atoms in a periodic potential

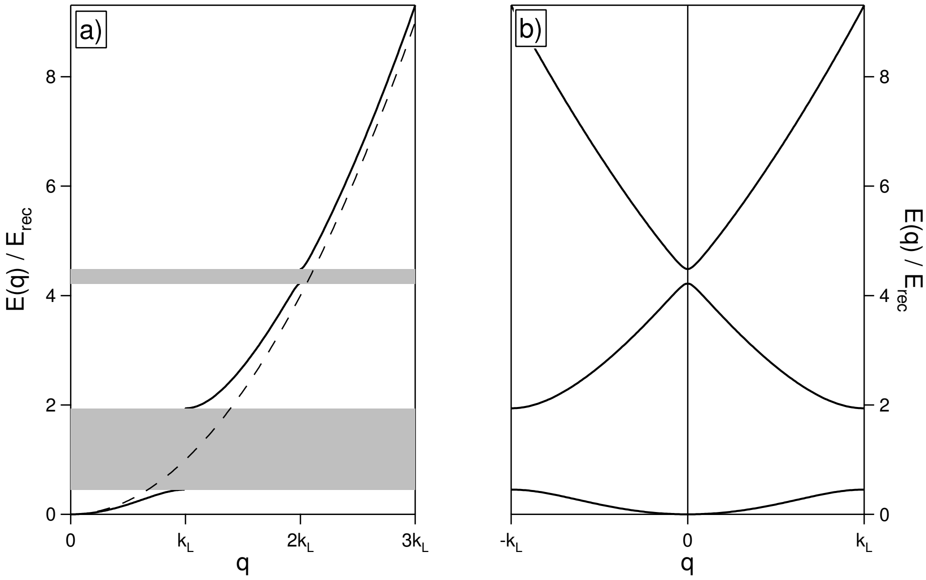

Figure 3.11: (a) The dispersion law for the free particle presented as a dashed line plotted with the energy versus momentum curve in the presence of the periodic potential (continuous line) (b) Energy spectrum folded into first Brillouin zone.

- **The bands:**

  The theory than has been most successful in describing periodic potentials in quantum mechanics is the Bloch bands theory. The Hamiltonian describing a system in the presence of a spatial periodicity equal to L is given by:

$$H = \frac{\nabla^2}{2m} + V(x) = \frac{\nabla^2}{2m} + V(x+L), \tag{3.49}$$

  and it can be easily shown that its eigenstates take the following form:

$$|\psi_{n,q}(x)\rangle = \sum_q e^{iqx} |u_{n,q}(x)\rangle\,, \tag{3.50}$$

where $|u_{n,q}(x)\rangle$ is periodic in space. the energy spectrum of these eigenstates have gaps in the energy dispersion relation every k_L. This curve can be folded into the first Brillouin zone and its limitations are described by the interval $q \in [-k_L, k_L]$ in quasi momentum space. One can consider the same phenomenon in the atom-optic approach. If the Fourier transform of the equation (3.49) it done, we obtain:

$$|u_{n,q}(x)\rangle = \sum_j u_{n,q}(j)e^{i2jk_L} = \sum_j c_{n,q} |2jk_L\rangle\,, \tag{3.51}$$

so the eigenstates takes the form:

$$|\psi_{n,q}\rangle = \sum_j c_q |q + 2jk_L\rangle\,, \tag{3.52}$$

where $|\psi_{n,q}\rangle$ is a superposition of plane waves produced after the n$_{th}$ order of the diffraction process. From the experimental point of view it means that the state of the BEC in the optical lattice can be seen as a superposition of velocity classes with discreet momentum distribution $|q + 2jk_L\rangle$. Figure 3.12 presents a BEC released from the lattice after a t_{TOF} time of flight of 23.6 ms. The image shows different clouds located in space at positions $j \cdot (2t_{TOF})/m$. Each of the clouds contain atoms that experiences j cycles of absorption and emission of the lattice photons.

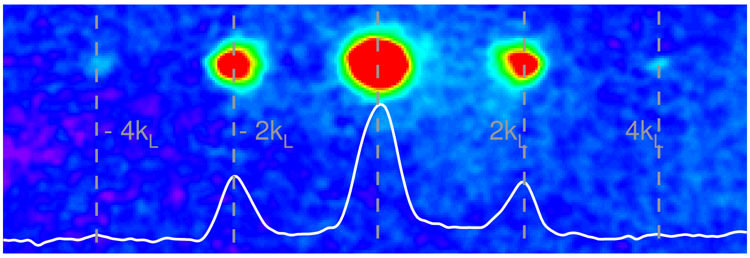

Figure 3.12: The time of flight picture of a BEC released from an optical lattice 17 E$_{rec}$ deep. The white line represents an integrated profile of the atoms distribution.

- **The two level solution:** The band gaps resulting from Bloch theory can be also observed in a simple toy model closer to the atom optics approach. The model follows the treatment presented in the Section 3.6. It is repeated here because the effective potential acting on the atoms in an optical lattice plays an important role in the following analyses.

  In a system composed by the ground state $|g\rangle$ and the excited state $|e\rangle$ interacting with the electric field of a standing wave laser, the presence of the optical lattice, the Hamiltonian can be written as:

  $$H = \begin{pmatrix} -\hbar\Delta & \hbar\Omega_R \sin(k_L x)/2 \\ \hbar\Omega_R \sin(k_L x)/2 & 0 \end{pmatrix}.$$

  where x is the mean value of the position and Ω_R stands for the Rabi frequency. When a large detuning is considered, the upper state is not excited and, in analogy with equation (3.39), the ground state eigenvalue is described by:

  $$\Delta E_g = \hbar\frac{\Omega_R^2}{4\Delta}\sin^2(k_L x). \tag{3.53}$$

  That means that the atoms experience a potential $V(x)$, see equation (3.48) with V_0 given by:

  $$V_0 = \hbar\frac{\Omega_R^2}{4\Delta} = 2\hbar\Omega_R^2. \tag{3.54}$$

  The eigenstates of the Hamiltonian $H(x) = \frac{p^2}{2m} + \frac{V_0}{2}\cos(2k_L)x$ are the sum of the Mathieu functions. At the edge of the Brillouin zone on the base of the atomic plane waves $|{+k_L}\rangle$ and $|{-k_L}\rangle$ one finds,

  $$H = \begin{pmatrix} E_{rec} & V_0/4 \\ V_0/4 & E_{rec} \end{pmatrix},$$

  with its solutions:

  $$E_0(k_L) = E_{rec} - \frac{V_0}{4}; |\psi_{0,k_L} =\rangle \frac{1}{\sqrt{2}}\left(|{+k_L}\rangle - |{-k_L}\rangle\right) \tag{3.55}$$

  $$E_1(k_L) = E_{rec} + \frac{V_0}{4}; |\psi_{1,k_L} =\rangle \frac{1}{\sqrt{2}}\left(|{+k_L}\rangle - |{-k_L}\rangle\right). \tag{3.56}$$

This calculations allows us to observe the energy spectrum of the Hamiltonian from equation (3.7.2) with its two eigenstates (equation (3.56)). This eigenvalues are not degenerate but have a difference in energy of $\Delta E_0 = V_0/2$. This is equivalent to an *energy gap* in the dispersion law by Bloch theory.

- **Tight binding Model and Wannier States:**

  One can study a periodic system considering a localized wavefunction $|\phi_n\rangle$ of an atom in a single site with perturbations coming from the neighboring sites [46]. In this approximation, one deals with the overlap of atomic wavefunctions which are sufficient to require a correction to the isolated atoms picture. However, the single site description remains relevant. The Hamiltonian (3.49) can be expressed in the Wannier basis as well. The Hamiltonian matrix elements are:

  $$H_{n,l} = \langle\phi_n| H |\phi_l\rangle = E_0. \tag{3.57}$$

  If the contribution from the next-nearest sites are negligible, one is allowed to impose $H_{n,n+l} = 0$ for $l \neq 0, \pm 1$ which represents the tight binding approximation. The generic wavefunction is a superposition of the localized wavefunctions, the Wannier functions:

  $$\psi(x) = \sum_n c_n \phi_n, \tag{3.58}$$

  where ϕ_n are mutually orthogonal. The localized functions ϕ_n do not satisfy the Bloch theorem but this problem can be avoided by considering the following superposition of the localized wavefunctions:

  $$\psi_q(x) = \frac{1}{\sqrt{2}} \sum_n e^{iqnd} \phi_n, \tag{3.59}$$

  where N stands for the number of occupied sites. The energy dispersion for the fundamental band is given by:

  $$E(q) = \langle\psi_q(x)| H |\psi_q(x)\rangle. \tag{3.60}$$

  In the case of a single isolated state the localized functions are equivalent to the eigenstates of a harmonic oscillator. The widths of the energy levels of the Wannier functions are then described by the perturbations that are added by the other sites. In this way the the correlation between the band width and the dispersion are evident.

3.7.3 The adiabatic theorem

The adiabatic transfer of an eigenstate of a solvable Schrödinger equation to a perturbed one has been studied since the beginning of quantum mechanics [9]. The Schrödinger equation is represented in a form:

$$i\hbar\partial \left|\psi(t)\right\rangle = \left[H_0 + V(P(t))\right] \left|\psi(t)\right\rangle . \tag{3.61}$$

Equation (3.61) contains a term $V(P(t))$ that is varying in time because the parameter P varies with time. By solving the time dependent equation and taking into account the decomposition of the system at time $t = 0$, one can write the adiabatic condition:

$$\left|\left(\frac{\partial H}{\partial t}\right)\right| << \frac{\left|E_k - E_0\right|^2}{\hbar}, \tag{3.62}$$

where E_0 and E_k are energies of the initial and final state, respectively. One of the applications of the adiabatic theorem is the loading of atoms into a periodic potential. We can consider what can happen when the BEC described as a plane wave $|p\rangle$ is put into the optical lattice of depth V_0 at time $t = 0$. The states of the atoms in the basis of the Bloch states are given by:

$$|p\rangle_{t=0} = \sum_{n,q} \left|\psi_{n,q}\right\rangle \, \left\langle\psi_{n,q}\right| p\rangle, \tag{3.63}$$

where q is the momentum of the atoms in the first Brillouin zone, and n stands for the band index. $\langle\psi_{n,q}|\, p\rangle$ is the probability for the atoms of being in state $|\psi_{n,q}\rangle$

As in most of the experiments we want to populate only the ground state we load the atoms into the lattice in a time τ_{on} such that the atomic wavefunction follows the adiabatic state. The initial free particle state $|p\rangle$ is linked to the single Bloch state. Then the adiabatic condition (3.62) can be expressed:

$$\left|\left\langle \psi_{n',q} \left| \frac{d}{dt} \right| \psi_{n,q} \right\rangle\right| << \frac{\left|E_{n'} - E_n\right|}{\hbar}. \tag{3.64}$$

The loading into the optical lattice is adiabatic when the above condition holds for any Bloch state with $n \neq n'$. The most restrictive condition is for the band that is closest in energy. That means for $n' = n \pm 1$. If one loads the condensate into the $|\psi_{1,0}\rangle$ state of the fundamental band, loading will be adiabatic if the condition (3.64) is done for $n' = 2$. Considering a shallow lattice, the gap between the fundamental and the first excited state can be approximated with its value in the free particle case $|E_{n'} - E_n| \approx 4E_{rec}$ and the condition (3.64) becomes [62]:

$$\frac{d}{dt}\frac{V_0}{E_{rec}} << 32\sqrt{2}\frac{E_{rec}}{\hbar}. \tag{3.65}$$

In the case of loading with a linear ramp in time τ_{on} equation (3.65) can be reduced to:

$$\tau_{on} >> \tau_{ad} = \frac{1}{32\sqrt{2}\omega_{rec}} \frac{V_0}{E_{rec}}, \tag{3.66}$$

where $\omega_{rec} = E_{rec}/\hbar$. The adiabaticity condition 3.66 is also valid for the switching off procedure with the switching off time τ_{off}. On one hand if $\tau_{off} << \tau_{ad}$ the wavefunction of the atoms will be formed by the plane wave decomposition. On the other hand when $\tau_{off} >> \tau_{ad}$ the atomic wavefunction follows the adiabatic state instantaneously and the lattice is switched off in a single wave plane.

Chapter 4

Experimental Set-up and methods

4.1 Creation of Bose Einstein Condensates

To create a Bose Einstein Condensate several steps have to be done. Atoms have to be cooled and compressed to reach the critical value of the phase-space density for the macroscopic occupancy of the ground state. The experimental realization of the BEC is described in this section. The experimental setup in Pisa was created and improved over the years. First to describe the apparatus used to obtain ultracold samples was Donatella Ciampini [19]. In her thesis one can find the setup presented in more details.

4.1.1 The Experiment

A Bose Einstein condensate is the principal tool of our investigations and its creation is a hard task. Production of a BEC of ^{87}Rb atoms is the first step in almost all our experiments. ^{87}Rb is an alkali element, i.e., in group 1A of Mendeleev periodic table. Its valence electron is in the $5^2\mathrm{S}_{1/2}$ orbital so the lowest energy transitions are to the $5^2\mathrm{P}_{1/2}$ and $5^2\mathrm{P}_{3/2}$ levels. These transitions are called the D1 and D2 lines, centered at $795\,\mathrm{nm}$ and $780\,\mathrm{nm}$ respectively.

The optical transition used to cool atoms is the D2 line, whose spectrum is shown in figure (4.1). The hyperfine levels of the $5\ ^2\mathrm{S}_{1/2}$ and $5^2\mathrm{P}_{3/2}$ states are labeled F and F'. The ground state hyperfine level used in our experiments is $|F = 2\rangle$. Therefore, the frequency of the light used for the optical molasses and the MOT is near resonant to the transition $|F = 2\rangle \to |F' = 3\rangle$, the so-called laser cooling transition. It means that only the atoms in the $|F = 2\rangle$ level are trapped in the MOT. However, this laser cooling transition is not closed, and atoms can be off-resonantly excited to the $|F' = 2\rangle$ level, where they may decay to $|F = 1\rangle$. This decay may cause the losses of atoms from the MOT. To avoid this, light near-resonant to the $|F = 1\rangle \rightarrow |F' = 2\rangle$ transition is added to the laser cooling light. This action re-pump atoms from the $|F = 1\rangle$ level to the $|F = 2\rangle$ one. This light is called *repumper*.

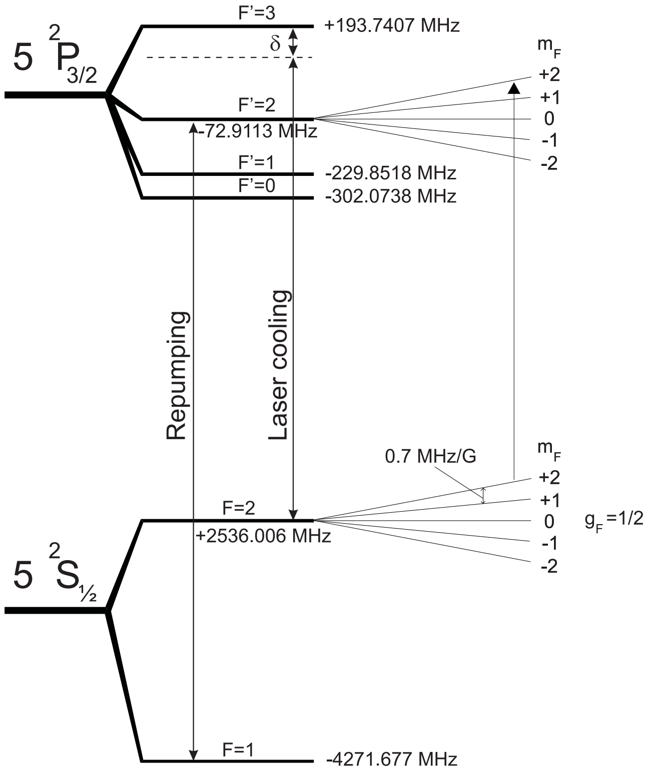

Figure 4.1: Scheme of D2 line of Rb 87

4.1.2 Laser sources

The experimental setup occupies two optical tables. One called the *laser table* is used for the preparation of almost all the laser radiation. The so called *BEC or cell table* contains the vacuum apparatus, the double MOT system and the major part of the optics used for beam preparation. To shield the laser setup from acoustical noise, both tables are enclosed by plastic curtains. This protection also helps to minimize the effect of temperature fluctuations in the laboratory. To avoid stray light the plastic shields of the BEC table are opaque.

The cooling and re-pumping light is provided by two master lasers, whose output is optically amplified in order to obtain the power needed for the experiment. The master lasers are composed of commercial laser diodes, with natural linewidths of the order of few MHz. To reduce the linewidth, the diode outputs are sent to gratings that create an external cavity with first order diffraction. At the back of the grating a piezo electric transducer is placed to vary the cavity length. In this setup, home made mounts are used. The whole laser system is temperature stabilized using two Peltier elements, with precision of 0.01K. Also, to avoid any coupling to the usual line noise, the lasers were powered from external batteries.

The frequency stabilization of the master lasers is a crucial point in all experiments with cold atoms. It is achieved using Doppler free spectroscopy. The laser frequency is locked to a peak in the saturated absorption spectrum and the correction signal is sent to the external cavity length. In the master mounting the grating position is controlled by a Piezo-Electric-Transducer (PZT). Scanning the voltage applied to the PZT, the atomic absorption lines are produced. The correction signal sent the PZT is created as following. An Acousto Optic Modulator shifts the laser frequency. Then, a double photodiode subtracts the Doppler curve to the saturation absorption signal. To derive the peak, a sinusoidal modulation is introduced to a Voltage Controlled Oscillator (VCO). Next, the output of the signal of the differential photodiode pair is fed to a lock-in amplifier to generate the error signal. At the end this signal goes to PZT and by this the lock-in loop is closed. The optical circuit scheme used for the frequency lock-in is present din figure 4.2

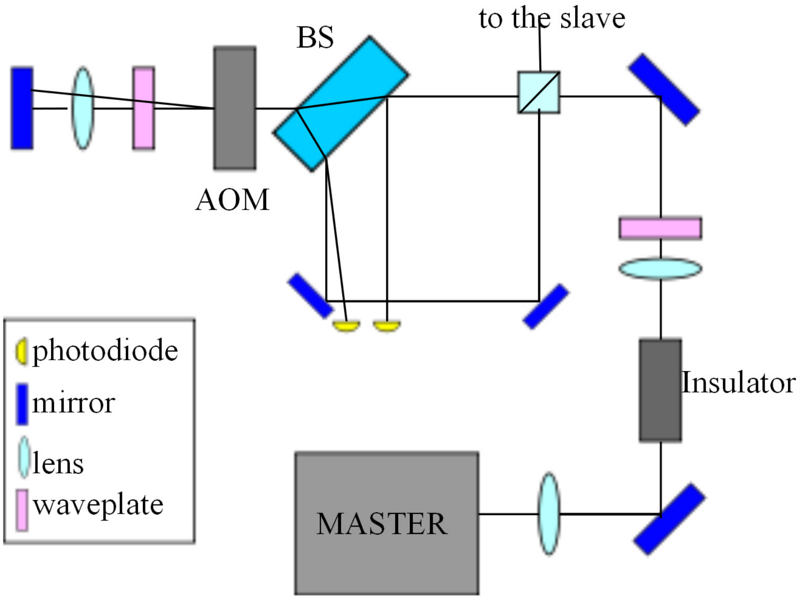

Figure 4.2: Saturated absorption scheme.

The output power of the two master lasers is around $\sim 20\,\mathrm{mW}$. The re-pump light is amplified by using a master-slave configuration, where a diode laser is used as a slave. The output power of the slave is around $\sim 55\,\mathrm{mW}$. To generate the laser cooling light much higher output power is needed. Thus, the amplification takes place in two stages. At first, the master light is injected to a slave diode laser. Then its output beam is used to inject a Power Amplifier (MOPA) amplifier with output power of $600\,\mathrm{mW}$. This light was used for all the purposes of the experiment and after splitting was passed through acousto-optic modulators (AOMs) to vary its frequency and to control the pulse duration and amplification.

4.1.3 The vacuum chamber

Our apparatus includes two quartz vacuum chambers placed at opposite sides of a central body. This is made of steel and is internally divided by a wall whose role is to divide the vacuum chamber in two parts. Each of them is connected by a hole placed in the center of the wall where a carbon tube is positioned in order to enhance differential pumping. The design of the cells is shown in the figure 4.3. The two cells have square cross-section, but are of different sizes: 49x49x100 mm and 24x24x100 mm. The smaller one is called $science\ cell$ because that is where the experiments take place. In order to created a pressure gradient between two cells, two ionic pumps connected to the two parts of the vacuum chamber creates pressure of 10^{-11} mbar in the science cell and 10^{-9} mbar in the big cell. In this way the differential pump system is created. its role is to collect the largest number of atoms to perform efficient evaporative cooling. The atoms are collected in the 2D MOT cell, where high Rb background pressure allows rapid MOT loading. Then they are pushed to the science cell where they are evaporative cooled.

Close to the 2D MOT (bigger cell) two pairs of dispensers are placed. They consist of electric resistances in which rubidium atoms are chemically bound to their surfaces. They emit atoms when an electric current heats the strips and induces a chemical reaction. The two dimensional MOT is created by two pairs of counterpropagating laser beams circularly polarized with waist $w_0 = 12$ mm. The laser is detuned by $\Delta = -2.4\Gamma$ from the $|F = 2\rangle \rightarrow |F' = 3\rangle$ transition ($\Gamma = 6.065\,\mathrm{MHz}$ is the natural linewidth of the $|F' = 3\rangle$ level), and a repumper beam is added to them. The 2D MOT magnetic gradient is $b' = 11\,\mathrm{G/cm}$. The role of the 2D MOT is to collect and cool atoms in a cigar shaped cloud, whose long axis is parallel to the carbon tube. In the same direction near resonant light is sent to push the atoms from the 2D MOT cell into the second chamber. In the science cell the atomic flux is collected by a 3D MOT.

4.1.4 The 3D MOT

To create a 3D MOT three pairs of counterpropagating beams are used. They are obtained by splitting the $32\,\mathrm{mW}$ beam into six beams of waist $w_0 = 8\,\mathrm{mm}$ and power ~5 mW. Repumper laser light is added to two of these pairs. The six

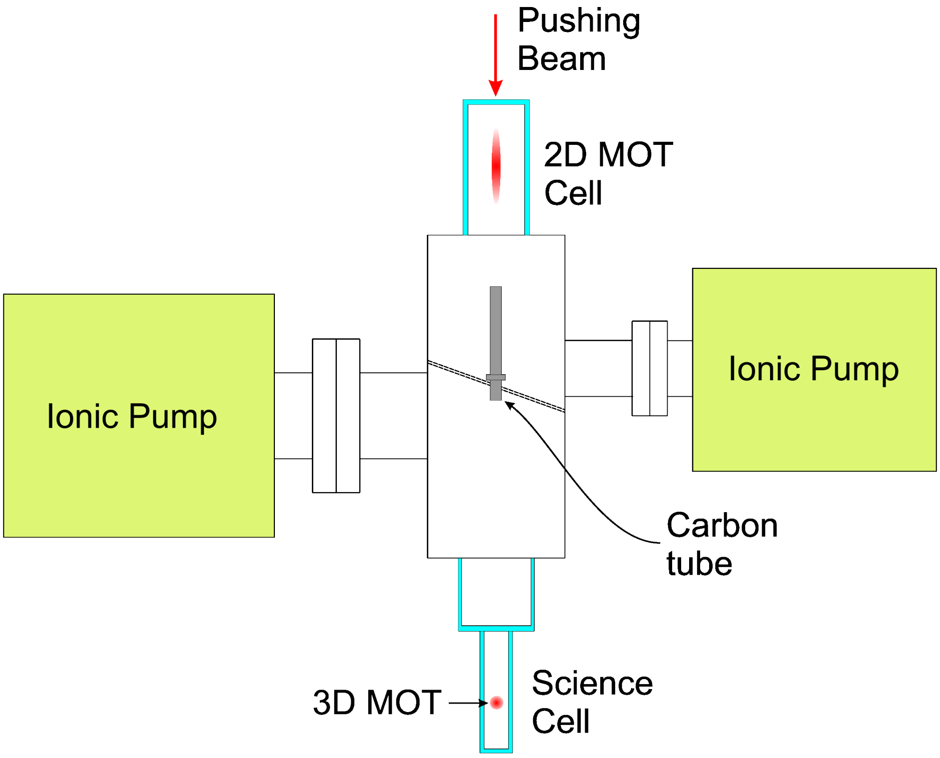

Figure 4.3: Scheme of the vacuum chamber. The magnetic field coils and both 2D and 3D MOT laser beams are not present.

beams are detuned from the $|F = 2\rangle \rightarrow |F' = 3\rangle$ transition by $\Delta = -2.9\,\Gamma$. The magnetic gradient for the MOT is $b' = 6.6\,\mathrm{G/cm}$. The flux of atoms from the 2D MOT leads to a continuous loading of the 3D MOT. This loading process is counteracted by atom loss process that is mainly due to collisions with background atoms. It takes $\sim 90\,\mathrm{s}$ of loading for the MOT to reach a stationary size, where up to $2 \cdot 10^9$ atoms are trapped. A portion of the light scattered by the atoms is collected by a lens and sent to an amplified photodiode, whose signal is proportional to the number of atoms in the MOT. This defines the reference for the trigger for the experiment in order to start with the cloud of roughly the same number of atoms for every cycle. In this experiment loading times of $15 - 35\,\mathrm{s}$ are usually sufficient in order to trap enough atoms before starting sub-Doppler and evaporative cooling.

4.1.5 The magnetic field

The cooling and trapping of atoms requires different magnetic fields whose generation requires power supplies capable of generating high currents and special switches for large currents. This section presents a summary of the technical features of our system.

- **The quadrupole field**. This is created by six cylindrical pancake-shaped coils whose symmetry axis is along the direction of gravity Z, that is hence the strong axis with the largest field gradient. In order to create a spatial magnetic gradient, the three coils above the science cell are in anti-Helmholtz configuration with respect to the three coils below the science cell, see Fig.4.4. The coils are made of copper and are covered with an insulating sock. The wires used for the coils are hollow, and are continuously cooled by water flow. The resulting magnetic gradient has cylindrical symmetry so that its modulus in the z direction (the strong axis) is $2b'$, while in the x, y directions it is b'. Magnetic gradients up to $b' = 366\,\mathrm{G/cm}$ are created when the current is 226 A . This value is reached in $4\,\mathrm{ms}$, while the time for switching off the field is of the order of few μs.

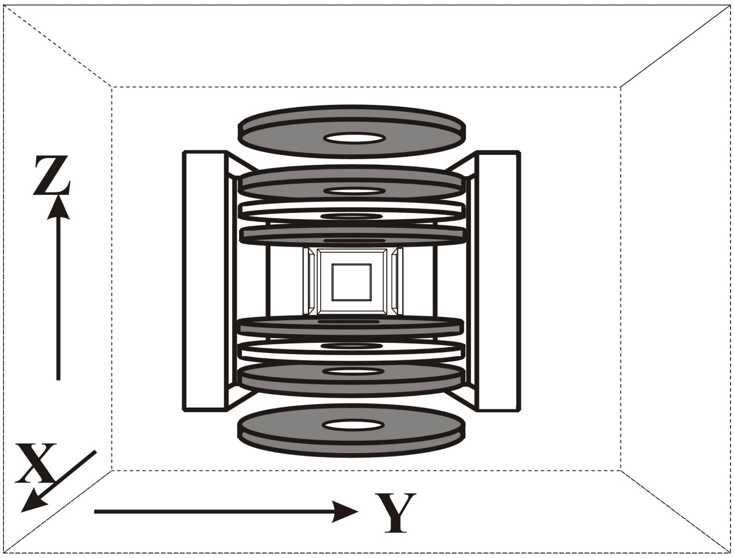

Figure 4.4: Schematic diagram of the mount of the coils for the magnetic gradient (shaded) and the rotating bias field (white). The science cell is at the center of the coils.

- **The rotating bias field**. This field B_{TOP} is created by two pairs of coils: a pair of circular coils that are placed between the quadrupole coils, and a pair of square coils in the orthogonal direction (see Fig. 4.4), both in the Helmholtz configuration. The current flowing in each pair oscillates in time, and the pairs have a phase difference of by $\frac{\pi}{2}$: $I_{circular} = I_{TOP} \sin \omega t$, $I_{squared} = I_{TOP} \sin{(\omega t + \frac{\pi}{2})}$, with $\frac{\omega}{2\pi} = 10\,\mathrm{KHz}$. The maximum value of the field is $B_{TOP} = 38\,\mathrm{G}$. The cooling of the coils is ensured by their contact with the water-cooled quadrupole coils.

- **The compensation coils**. These are three mutually orthogonal pairs of coils in the Helmholtz configuration. The current flowing in these coils is of the order of 100 mA. The magnetic field created by these coils is used to compensate the external fields, such as the earth's magnetic field and the magnetic field created by the ion pumps.

- **The extra-compensation coil**. This is single a coil placed above and parallel to the quadrupole coils. It creates a magnetic field that is varied during the experiment in order to be able to vertically move the position of the cloud along the z-axis and hence to minimize the losses when the trap is changed, e.g., when passing from the TOP to the dipole trap.

4.2 The experimental sequence

Once $\sim 10^9$ atoms are trapped in the MOT, sub-Doppler and evaporative cooling are used in order to create a BEC. The different stages for driving the atoms through the BEC phase transition results in a temporal sequence during which several experimental parameters (laser frequency and intensity, magnetic fields etc.) are changed. The temporal sequence of the experiment is controlled by a computer with a precision of $10\,\mu\mathrm{s}$. Every single experiment performed is destructive for a BEC, so the whole process has to be restarted from the 3D MOT loading. In the following, the experimental sequence for the creation of a Bose-Einstein condensate is listed in chronological order.

- **The compressed MOT (C-MOT)**. During this phase the size of the MOT is reduced by decreasing the magnetic gradient (to $b = 2.6\,\mathrm{G/cm}$) and increasing the detuning (to $\Delta = -4.8\,\Gamma$) of the laser. This phase is $200\,\mathrm{ms}$ long. The compression is done to optimize the loading into the TOP trap.

- **The Molasses**. During this phase ($6\,\mathrm{ms}$), the magnetic gradient is switched off and the detuning of the laser increases to $\Delta = -5.0\,\Gamma$. The sample is cooled to the sub-Doppler regime, reaching at the end of the stage a temperature around $15\,\mu\mathrm{K}$. Moreover, the capacitors of the quadrupole field power supply are charged during the molasses phase. This happens in order to reduce the rising time of the magnetic gradient in the TOP trap.

- **Optical pumping**. This phase consists of pumping the atoms into the $|F = 2, m_F = 2\rangle$ state. The quantization axis is defined by the rotating bias field B_{TOP} that is switched on with amplitude $B_{TOP} = 3.8\,\mathrm{G}$. The selection rule for the light-induced atomic transition $\Delta m_F = +1$ is realized when the light is circularly polarized $\sigma^{(+)}$ and the magnetic field is pointing in the same direction as the light wavevector.

- **The TOP trap**. At the end of the optical pumping stage the atoms are loaded into the TOP trap. This is done by increasing the magnetic gradient in $1\,\mathrm{ms}$ to $b' = 73\,\mathrm{G/cm}$, while the rotating bias field is turned on at its maximum value, in order to maximize the circle of death radius. After the loading, the trap frequencies are first increased in order to enhance the collision rate, and hence to create the conditions for efficient evaporative cooling. The evaporative cooling is then realized by reducing the circle of death radius. At the end of the process the cloud contains $\sim 6 \cdot 10^5$ atoms at a temperature $T = 2.5\,\mu\mathrm{K}$.

- **The Dipole trap**. The atoms are loaded into the dipole trap, which is created by use of a Yb:YAG laser with a maximum power of 5W and emitting at $\lambda = 1030$ nm, i.e., far off-resonance from the Rb transitions. Its output is split into two beams, and each of them is sent to an acousto-optic modulator, and then to the atoms. There the two beams intersected at an angle $\sim 90°$, creating an optical trap for the atoms. After passing through the science cell, the reflection of each beam is collected and sent to a photodiode, whose signal is sent to a PID circuit to control the power of the radiofrequency input of the corresponding AOM and hence the power of the dipole beams. The dipole beams have a maximum power of 1.2 W each, and are focused on the atoms with a waist $w_0 \cong 70\,\mu\mathrm{m}$. The typical condensate is created in a trap with maximum mean frequency of $\bar{\omega} \sim$ 520 Hz.

- **Bose Einstein Condensation**. Following the atom loaded into the dipolar trap, evaporative cooling starts. This is performed by ramping down the power of both dipolar beams, so both the depth and the frequencies of the optical trap are reduced. The overall ramp is formed by four linear ramps of decreasing gradient. This cooling stage is $2.5\,\mathrm{s}$ long, and at its end a Bose Einstein condensate of up to 10^5 atoms is created. An image after time of flight of the almost pure condensate is presented in figure 4.5(b).

- **Experiment**. Holding the condensate in the dipolar trap with the final frequencies or in other configurations, different experiments are performed by switching on an optical lattice, Rydberg laser radiation or modulating the power of the dipolar trap beams.

- **Imaging** At the end of the experiments the atoms are released from the trap and allowed to expand in free space, in order to decrease the density of

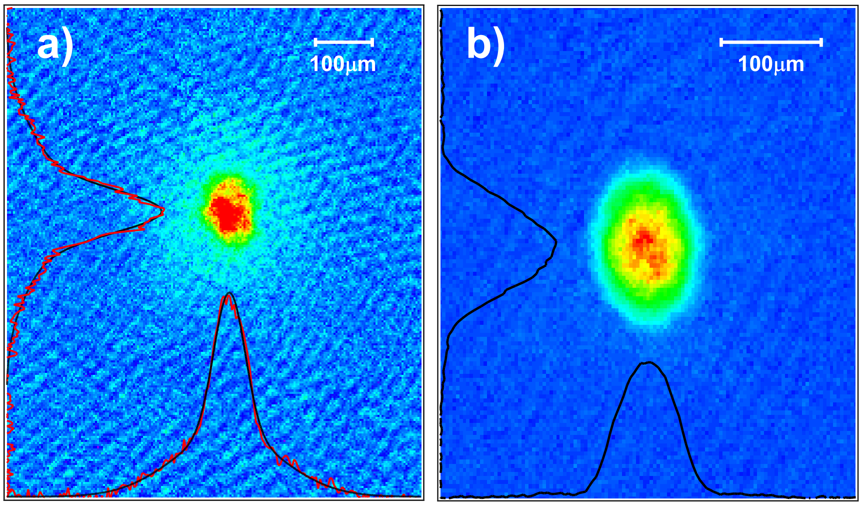

Figure 4.5: Images of the atomic cloud after 23 ms of time of flight, in (a) just below the threshold temperature for condensation where the bimodal distribution is evident, and in (b) for a almost pure condensate far below that temperature.

the cloud and increase its size. After a certain time (called *time of flight*) of $\sim 10 - 20\,\mathrm{ms}$ a resonant light pulse of $20\,\mu\mathrm{s}$ duration illuminates the atoms and then is collected by a CCD camera, in which the shadow of the atomic cloud is imaged. The CCD camera is from DTA, featuring a Kodak Chip (KAF 1400) with pixel size 6.8 $\times$ 6.8 μm, whose quantum efficiency is 40% at $780\,\mathrm{nm}$. In front of the CCD camera an objective (Rodenstock Aporodagon) of focal length $f = 75\,\mathrm{mm}$ and f-number $f/\# = 4.5$ is placed. The objective is optimized for 1:2 reduction, but it is used reversed in order to have a magnification of $\sim$ 2. The system is focused by minimizing the apparent size of small atomic clouds imaged on the CCD and the calibration of the image size is done by performing an experiment of free fall of the condensate under gravity.

The distinctive threshold for the formation of the condensate is identified by looking at the profile of the absorption images. Just below the critical temperature T_C, a clear bimodal distribution is visible where the narrower peak contains the condensate while the wider one is the thermal part of the cloud. Almost pure condensate is observable when temperature of the sample is equal to T_C.

4.3 Excitation, ionization and detection of Rydberg states

Dealing with Rydberg atoms is a complex task. In this section excitation path are shown. Then lasers sources are described. Finally, ionization and detection of Rydberg atoms are presented.

4.3.1 Excitation Paths of Rydberg states

As introduced in the previous section atoms are cooled down via laser and evaporative cooling until they undergo Bose Einstein condensation. The BEC prepared in this way is subject to photoionization or excitation to a Rydberg state. An atom absorbs an incident photon which specifies the energy of the excited level. If one photon is absorbed, this process will be called single-photon excitation. Two-photon excitation is a special case of optical excitations. In this case the threshold energy for excitation is achieved by combining two photons (equal or different). For ^{87}Rb single photon transition to a Rydberg state would require an ultraviolet photon source but the limitation in the range of wavelengths at which cw lasers are available made us consider the two-photon excitation scheme shown in figure 4.6. To excite atoms to a chosen Rydberg state transition $5S_{1/2} \rightarrow 6P_{3/2} \rightarrow nl$ is used. The first step, $5S_{1/2} \rightarrow 6P_{3/2}$ is achieved using 420 nm blue light. To avoid creation of unwanted ions by blue laser and resonant excitation of the $6P_{3/2}$ state, the first step of the excitation is detuned between $300\,\mathrm{MHz}$ and $1\,\mathrm{GHz}$ from resonance. Ionization of the rubidium atoms takes place via the two blue photon transition $5S_{1/2} \rightarrow 6P_{3/2} \rightarrow$ *ionization limit*. Resonantly excited states and unwanted ions are enough to destroy coherence of Rydberg excitation. From the $6P_{3/2}$ state, accordingly to the atomic selection rules, atoms can be excited to any D or S state. To reach these states an infrared laser locked between 1000 nm and 1030 nm is used. This wide wavelength range allows the excitation of state with principal quantum number n between 30 and 120. The majority of the experiments presented in this thesis states 55 D and 53 S were used. The choice of quantum number n was rather arbitrary at the beginning of the experiments. For this reason some data in this thesis was obtained using excitation to different Rydberg states. Nevertheless through the course of these the measurements, when the limitations of the set-up become clear, this choice was adjusted. All factors affecting the choice of principal quantum number are described in the following parts of this thesis.

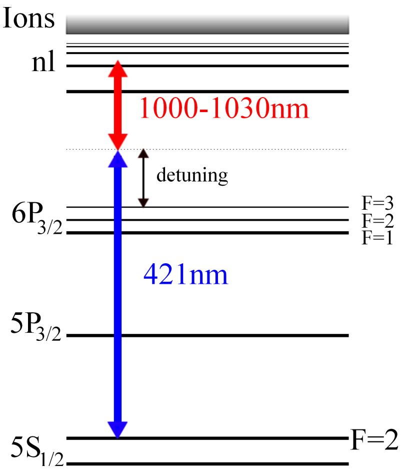

Figure 4.6: Rydberg atom excitation scheme. the first step is achieved by $421\,\mathrm{nm}$ laser light whereas the second step is by IR radiation between $1000\,\mathrm{nm}$ and $1030\,\mathrm{nm}$

4.3.2 The Lasers Settings

To coherently excite Rydberg states, the Rabi frequency has to be large compared to spontaneous decay and decoherence rate. Level spacing of Rydberg states become smaller (n^{-3}) with higher principal quantum number n . To selectively excite only one state, the laser linewidth must be much smaller than the gap between Rydberg states. Therefore, the generation and stabilization of the laser light is of high importance. In the following the lasers used for Rydberg atom excitation and frequency locking system are explained.

- **First step transition :** $5S_{1/2} \rightarrow 6P_{3/2}$. The SGH 100 doubling unit uses a TA 100 laser ($840\,\mathrm{nm}$) as a light source. The $420\,\mathrm{nm}$ wavelength is achieved by doubling a MOPA laser (TOPTICA TA 100, with output power $700\,\mathrm{mW}$) with a TOPTICA doubling cavity (SGH 1004). A resonant doubling cavity in a bow tie geometry composed of two plane and two confocal mirrors is used. The schematic circuit is presented in figure 4.7. In this configuration two beam waists are produced between each mirror pair. The doubling crystal is made of potassium niobate $KNbO_3$ and is placed in the beam waits of the two confocal mirrors. The resonator is defined by 4 mirrors, where one is partially transmitting for IR light and one is mounted on a piezo element which adjusts the cavity length. The doubling crystal allows non critical phase matching for the range $420 - 480\,\mathrm{nm}$. This phase matching is achieved by temperature tuning. The temperature of the crystal is controlled using a Diode Temperature Controller DTC 100.The output power in this configuration varies between 40 and $60\,\mathrm{mW}$. The beam is then controlled via an Acousto Optic Modulator AOM with 80% efficiency for the $+1$ order. The 0-th order is sent to a photodiode and is utilized to control the stability of the power during the experiment. The light arriving on the atoms has a power of around $20\,\mathrm{mW}$.

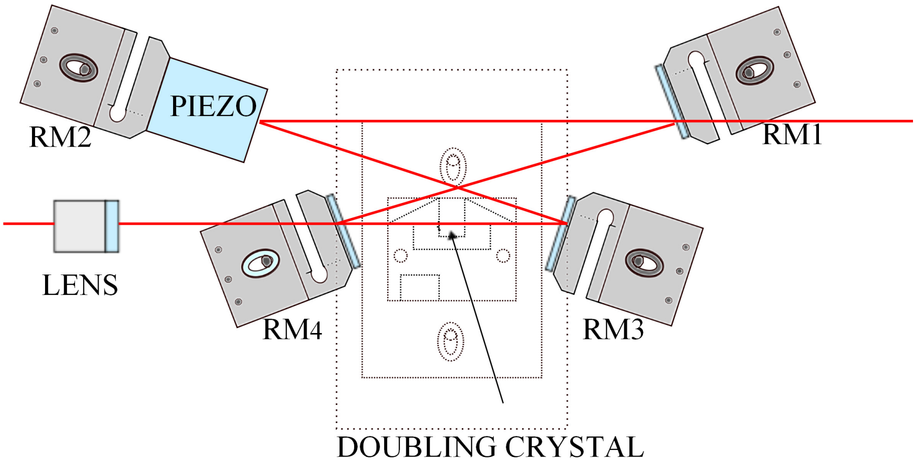

Figure 4.7: Optical circuit of the SHG100 resonant doubling cavity.

- **Second step transition**. The second step ($6P_{3/2}$ →nl) of the Rydberg excitation is accomplished by IR laser light. This laser is tuned to a frequency of the one of the Rydberg level, between 1000 nm and $1030\,\mathrm{nm}$, which corresponds to a range of quantum states between n = 30 to n = 120. To overcome the problem of limited output power, a master-slave configuration is used. A TOPTICA DL 100 laser (output power =20 mW) is injected into a Sacher TIGER laser (output power $= 400\,\mathrm{mW}$). The DL 100 is a tunable grating stabilized diode laser with a linewidth of the order of $1\,\mathrm{MHz}$. The beam arriving to the atoms is also controlled by an AOM. The power on the atoms varies between 140 and $150\,\mathrm{mW}$.

- **Reference Laser**. The third laser injected to Fabry-Perot Interferometer (described below) is an infrared TOPTICA DL100 with a wavelength of 780 nm. In this configuration, the $780\,\mathrm{nm}$ beam is used as a reference. This laser is locked to a Rb absorption line using saturated absorption technique, which along with temperature stabilization keep the laser locked for hours at a time, with a linewidth smaller than $1\,\mathrm{MHz}$.

- **Locking System**.Both lasers used for the excitation of Rydberg states are locked using a Fabry-Perot interferometer FPI 100. A third laser injected to

> FPI is the reference laser of $\lambda = 780\,\mathrm{nm}$. Scanning Fabry-Perot interferometers are frequently used tools for measuring spectral characteristic of cw lasers. They may also be used as a precise locking system which is the task the FPI fulfills in this experiment. The Fabry-Perot Interferometer FPI 100 used in our experiment is a piezoelectrically scanned device. It combines high finesse F ($F\ \sim$120 for the blue laser) with the flexibility of using it as a stable reference cavity. The FPI is characterized by a $1\,\mathrm{GHz}$ free spectral range FSR for a set wavelength. This parameter range depends on the wavelength of the injected laser. In this experiment three different laser beams are injected to the FP cavity. This cavity is optimized for the $842\,\mathrm{MHz}$ light. The main problem of this solution is the change of resolution and free spectral range of the $780\,\mathrm{nm}$ and $1020\,\mathrm{nm}$ lines. The FSR ratio of $1020\,\mathrm{nm}$ and $842\,\mathrm{nm}$ laser light is taken into account when standard deviation of the locked beam is calculated. Lasers injected into the FPI already have a linewidth smaller or comparable with $1\,\mathrm{MHz}$, so the main task of the interferometer is to stabilize the spectral lines against thermal drift during the measurement. Also, the temperature of the FP cavity has to be stabilized. The cavity is placed inside an isolated wooden box controlled by two Peltier elements. A scheme representing the laser frequency stabilization system is shown in figure 4.8 and has the following protocol. Firstly, the signal of the FPI scan is acquired by the computer with LABWIEV interface and the localization of the spectral lines is done. Figure 4.9 shows the LABWIEV locking program. To scan the frequencies of the blue and IR lasers inside the FPI cavity, TOPTICA Scan Controls SC 110 are used. Then, the distance between the reference laser and the excitation laser is fit in units of FSR. By keeping constant the distance between both the IR and the Blue laser the correction signal is generated. Subsequently, the output feedback is sent from the computer to the PID, proportional integral differential regulator (TOPTICA PID 110) used to stabilize the laser frequency on the chosen value. As a result the absolute frequency stability is on the order of 1 MHz. Nonetheless, the FPI is thermally isolated a small line drift in time is still visible. To avoid this an error signal from the computer is sent to the cavity which corrects against the change of the position by sending the feedback to the computer. In this configuration the lasers are kept locked for a long time.

The Fabry- Perot Interferometer and the $780\,\mathrm{nm}$ reference laser are placed on the laser table to avoid noise introduced by mechanical shutters from the cell table. The $780\,\mathrm{nm}$ light is transmitted via an optical fiber to the FP fiber coupler situated on the cell table, along with the $842\,\mathrm{nm}$ and $1020\,\mathrm{nm}$ lasers.

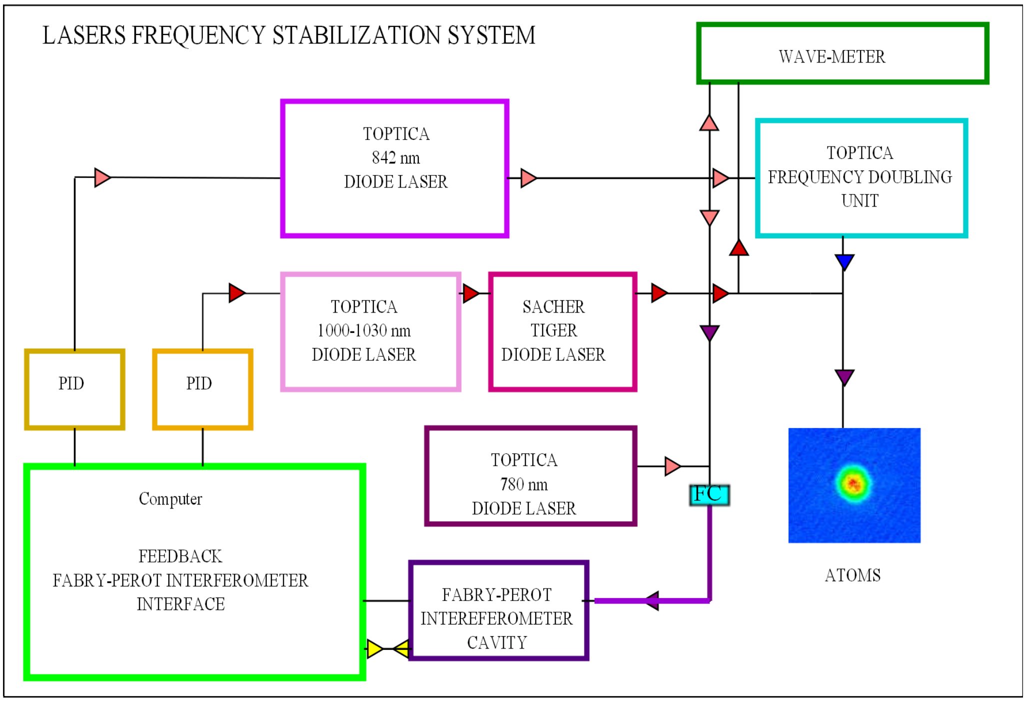

Figure 4.8: Frequency stabilization laser scheme.

Both lasers are superimposed before reaching the ions to excite the same volume of the sample. The pulse duration of the excitation lasers lasts between $100\,\mathrm{ns}$ and $10\,\mu$s, depending on the experiment.

4.3.3 The Ionization and the Detection of Rydberg States

Rydberg atoms are very sensitive to electric fields (polarizability $\sim n^7$). This sensitivity provides a possibility to manipulate Rydberg atoms using for example the Stark effect, where the energy of a state depends on the strength of an electric field. Electric fields can be used to field ionize, excite atoms to high quantum states and to push them toward the detection device, a Channel Electron Multiplier (CEM). The KBL510 CEM is used in the experiments. By introducing some moderated changes to the CEM bias circuit it is possible to operate the CEM in two different modes, to detect ions or electrons. In the case of the experiments presented in this thesis the ions are detected. The CEM is kept at $-2.4\,\mathrm{kV}$ in the ion counting mode to ensure maximum detection efficiency. After the detection of ions by the CEM the output pulse is amplified by a fast timing amplifier and subject to a constant fraction discriminator. Then an output signal is observed on the LeCroy scope (WAVERUNNER) where ions can be counted. The CEM is

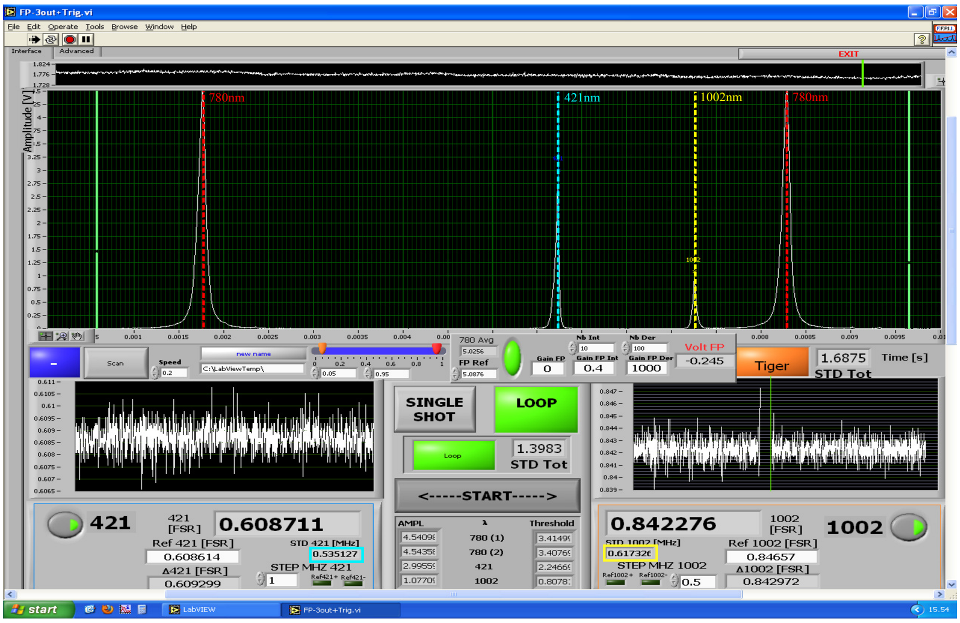

Speed 0.2
C:\LabViewTemp\
0.05
0.95
780 Avg 5.0256
FP Ref 5.0876
Gain FP 0
Nb Int 10
Gain FP Int 0.4
Nb Der 100
Gain FP Der 1000
Volt FP -0.245
1.6875 STD Tot
Time [s]
1.3983 STD Tot

421 [FSR] 0.608711
Ref 421 [FSR] 0.608614
Δ421 [FSR] 0.609299
STD 421 [MHz] 0.535127
STEP MHZ 421 1
Ref421+ Ref421-

AMPL	λ	Threshold
4.54098	780 (1)	3.41499
4.54358	780 (2)	3.40769
2.99559	421	2.24669
1.07709	1002	0.80781

1002 [FSR] 0.842276
STD 1002 [MHz] 0.617326
STEP MHZ 1002 0.5
Ref1002+ Ref1002-
Ref 1002 [FSR] 0.84657
Δ1002 [FSR] 0.842972

Figure 4.9: The frequency stabilization (locking) interface. The red dashed lines represent l780 nm reference laser, blue and yellow the 421 nm and 1000-1030 nm excitation laser respectively. The yellow and blue boxes present standard deviation of the excitation lasers.

located around 15 cm from the cell center, close to the exit of the graphite tube between the collection and science cell. A grid connected to a high voltage is located $10\,\mathrm{cm}$ from the ultracold atomic sample. Its task is to guide the emitted ions towards the CEM. Two pairs of plates connected to a high voltage are situated on the outside of the scientific cell. One pair is placed in front and one on the side of the vacuum chamber. A scheme presenting the science cell, including the charge detection system located under vacuum, is presented in the fig 4.10(a).
The cell used in this set-up is made of quartz which gives us easy access to the cell from all sides. It is not a common solution because of the creation of space charges on the cell. More common is to use a cell made of metal to avoid this effect because the conductive material would shield or neutralize them. In our case the glass cell is chosen for its optical access. It gives a possibility to implement optical lattice or freely change the paths of the excitation lasers. For this reason, a constant electric field applied to the plates may result in charging the glass cell and the creation of extra electric field acting on the atoms for a significant time. To overcome the problem of space charges in the cell, ions are collected through a sequence of electric pulses which typically have a rise time of a few ns and a duration on the order of μs. In the present setup, $3.5\,\mathrm{kV}$ is applied to the front

plates and $-1\,\mathrm{kV}$ to the lateral ones, for around 3.9 μs. This time is adjustable according to the Rydberg state. The $-1.5\,\mathrm{kV}$ pulse applied to the grid is longer (around $25\,\mu$s). The ionizing pulses of the electric field were applied with 33 μs delay. This configuration ensures a detection efficiency of positive ions on the order of $35(10)\%$. An ion signal detected by the CEM is presented in figure 4.10(b). One limitation of the setup is the ionization field limit. With maximal voltage applied on the plates we are not able to field ionize Rydberg atoms with quantum number lower than $n = 52$. We face several problems. First of all the plates are not placed inside the cell. This causes the shielding effect. Then electric field acting on atoms is not homogeneous and we don't know how exactly electric field lines propagate inside the cell. For this reasons it is not possible to estimate the electric field acting on the sample and the $n = 52$ value is the results of the experimental observation.

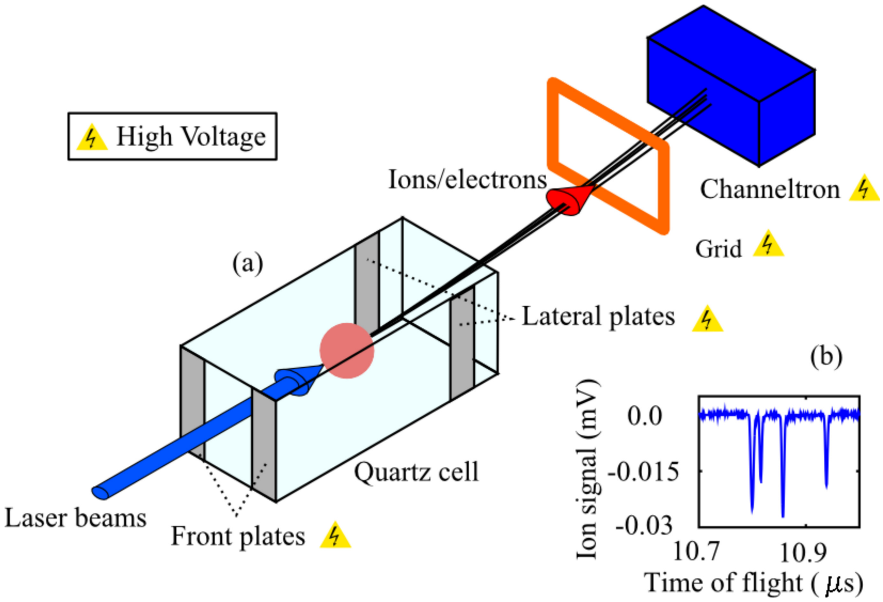

Figure 4.10: In (a) The laser beams are superimposed so as to excite atoms within the same volume. Ions are collected depending on the signs of the applied voltages. In (b) the ion signal detected by the channeltron is presented.

4.4 Experimental realization of an optical lattice

In this section the implementation of the optical lattices is described. First, the set-up used of our experiments presented. Then the experimental sequence will be explained.

4.4.1 The Set-Up

The optical lattice is created by crossing two different laser beams. They originate from the same laser, a Master Oscillator Power Amplifier (MOPA) TA100 produced by TOPTICA. The single mode laser output is set at a wavelength of around $\lambda = 849.2\mathrm{nm}$ and has an output power of $750\mathrm{mW}$. Before they split in two the beam passes through and optical insulator to avoid any back reflections that could affect the light mode. Then the beam is split using a $\lambda/2$ waveplate and polarizing beam splitter. Subsequently, each beam is guided through an acousto optic modulator AOM (Crystal Technologies) that diffracts the input beam and detunes it from its initial frequency. Both AOMs have their own radio-frequency (RF) source (Agilent 3325A). The two modulators are aligned to optimize the first order of diffraction and have the RF input centered at 74 MHz. Therefore, the lattice beams are at the same frequency, apart from the cases where a detuning between them is imposed on purpose. The efficiency of the AOMs is on the order of 70 $\%$ for the first order. The zero-th order of diffracted light of one AOM was sent to Fabry Perot cavity to monitor the single mode output of the laser. Each first order diffracted beam is guided to a single mode, polarization preserving optical fiber (OZ Optics). The optical set-up for the lattice described up to now is placed on the $laser\ table$. A scheme of this optical set-up is presented in figure 4.11.

The optical fiber outputs are mounted at a distance of 15 cm from the atoms. The power of each beam at the output of the fiber is around $70\,\mathrm{mW}$. In front of each fiber coupler a polarization cube is placed in a rotating mount as a polarization filter. The two beams are focused onto the atoms, and have a waist of around 120 μm and at the center of the cell. To provide a control of the power of each lattice beam during the experiment a small part of the beam that is reflected by the cell is sent to a photodiode. The photodiode signal is then sent to a PID circuit with a reference signal provided by the computer. The output of the PID is then sent to an attenuator that controls the RF power at the AOM input, and hence its diffraction efficiency. Both beams are controlled independently. The lattice spacing is given by:

$$d_L = \frac{\lambda}{2sin(\frac{\theta}{2})}, \tag{4.1}$$

where λ is the laser wavelength, and θ corresponds to an angle between two lattice beams. In figure 4.11a) the case of two counterpropagating lattice beams is shown. In this configuration lattice spacing is around half micron. To obtain lattice spacing comparable with the dipole blockade radius the angular lattice configuration is used (fig. 4.11b). In this case d_L is $\sim$3 μm for $\theta \sim 20^o$.

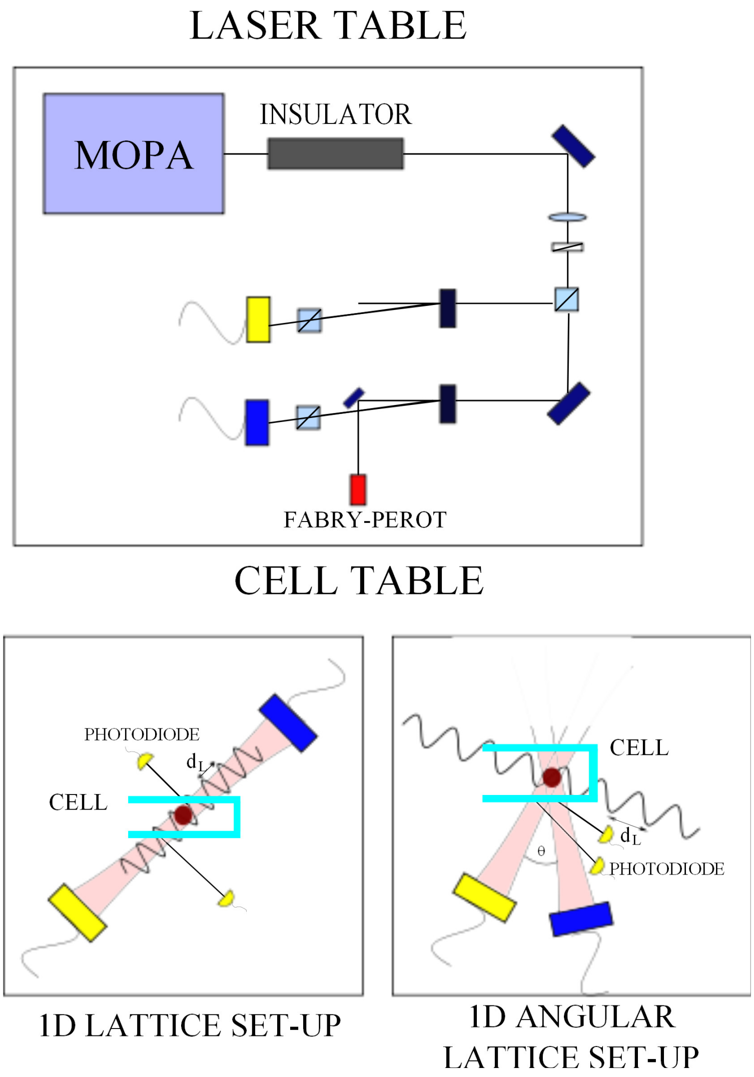

Figure 4.11: Optical circuit for optical lattice realization, case of two counter-propagating beams (d_L=0.42 μm) and of angular lattice created by two beams enclosing an angle θ.

4.4.2 Experimental sequence

The problem of adiabatic loading of atoms into an optical lattice is described in more detail in the previous chapter. Nevertheless, a few experimental parameters will be mentioned. To adiabatically load atoms into an optical lattice a linear ramp of a few tens of ms is used, as schematised in figure 4.12. During this time, atoms are transferred from the dipolar trap into the lattice by ramping up to the maximum the power of the lattice beams and ramping down the dipolar oblique beam. Then,

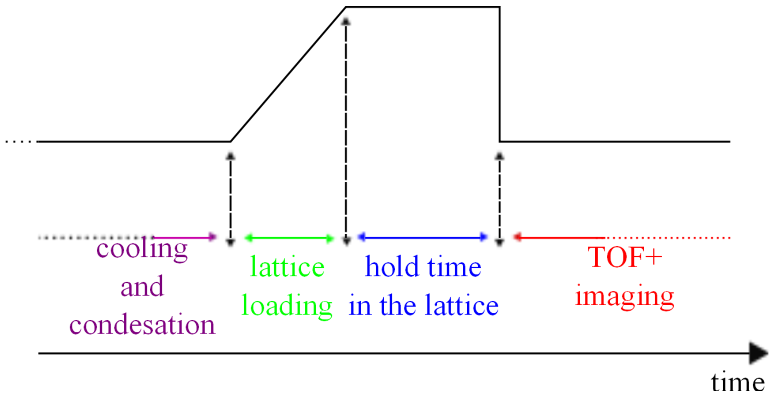

Figure 4.12: Scheme of experimental sequence.

atoms are kept inside the lattice for another few ms. This time is defined by the number and duration of excitation pulses sent to the sample. Finally, the optical lattice is switched off and the atoms are released. They are allowed to expand for a few ms and then the absorption image is taken.

4.4.3 Calibration of the optical lattice

Lattice depth is always measured in units of the recoil energy E_{rec}. Knowledge of this parameter is a reliable tool for the calibration of experiments, allowing us to perform experiments in comparable conditions every time. This value is even more crucial if one conducts experiments where agreement with theory depends strongly on the exact knowledge of the lattice depth e.g, when the tunneling rate is involved.

In principle, one can calculate the lattice depth making use of equation (3.48) While all of the atomic parameters within that equation are well known and the detuning is relatively easy to measure via spectroscopy it is much harder to precisely measure the waist of the lattice beams at the position of the atomic sample. Then other problem is to measure the optical powers and always results in some percent of error. For these reasons we use an alternative method of obtaining the value of the lattice depth. A very convenient way is to use the expansion of the atoms released from the lattice. Firstly, one loads the condensate adiabatically into the lattice and then abruptly switches the lattice lasers off. Gaussian wave packets at each lattice site will expand freely and interfere with one another. The interference pattern observed after some milliseconds of time of flight is a series of regularly spaced peaks, see figure 4.13a). These peaks correspond to the different diffraction orders. From the relative weight of the momentum peaks, the lattice depth can be calculated from, see ref. [24]:

$$s = \frac{V_0}{E_{rec}} = \frac{16}{\left[\ln P_{\pm 1}\right]^4 P_{\pm 1}^{1/4}}, \tag{4.2}$$

where $P_{\pm 1} = \exp \frac{-4\pi^2\sigma^2}{d^2}$ are the relative populations of the two symmetric plus and minus first order peaks with respect to the 0-th order central peak . However, one can use equation (4.2) only when the lattice depth is not too deep ($s < 20$), see figure 4.13b). In the case when $s > 20$ one need to use a less accurate harmonic approximation to the sinusoidal lattice potential about a potential minimum by defining σ the Gaussian width of the wavepackets at the individual lattice sides [24]:

$$\sigma = \frac{d}{\pi s^{1/4}}, \tag{4.3}$$

By inserting equation (4.3) into the formula defining the width of the cloud after a time of flight:

$$w = \frac{\hbar t_{TOF}}{m\sigma}, \tag{4.4}$$

one obtains a lattice depth is given by:

$$s^{1/4} = \frac{dmw}{\pi \hbar t_{TOF}}. \tag{4.5}$$

In the case of our experiment equation (4.2) is used when we deal with a lattice spacing on the order of half a micron. In the case of a bigger d the different peaks of the interference pattern are not distinguishable and one need to use equation (4.5) to estimate the lattice depth.

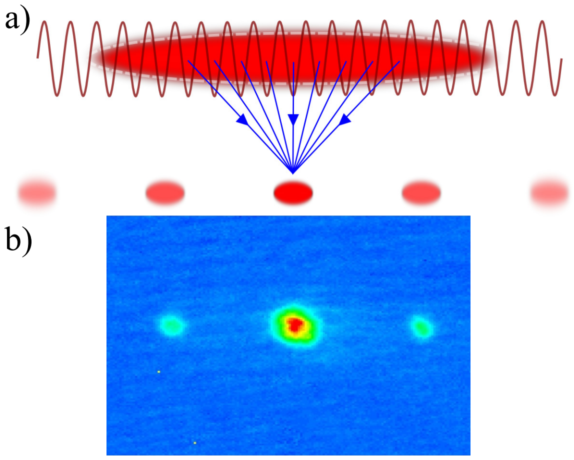

Figure 4.13: (a) A scheme of Bose Einstein condensate loaded into an optical lattice with interference patterns formed after releasing atoms from the optical potential. (b) The real image of the interference pattern of a BEC released from an optical lattice. One can see in the center the 0-th order peak and on the left and right two ±1 order peaks.

Chapter 5

Characterization of the experimental system

To conduct experiments that aim at quantum information processing, precise knowledge of the system is required. This led us to perform a series of preliminary measurements which give answers on the limitations and stability of the set-up. The role of these measurements was to precisely characterize the experimental system which gives us important information for the experiments presented in the future chapters of this thesis. In order to do this we use two methods. First of them is the photoionization as it is an efficient tool to characterize system detection efficiency or dynamics of the populations and it is not affected by the Rydberg atoms interactions. As a second method we used two photon transition to Rydberg states in order to characterize Rydberg transitions.

To describe our system we measured several quantities. The electron collection is a basic technique that we use to extract information from the system, therefore precise knowledge of the detection efficiency is crucial for estimation of number of excited Rydberg states. We also need to take into account the effect of the charges building up in the quartz cell during ionization process and how the residual electric resulting from this field affects energy levels of Rydberg atoms. This is important when one examines the Rydberg atom spectra or results of measurements on the dipole blockade. Furthermore, the knowledge of the Rabi frequencies of the two steps of the Rydberg excitation are crucial in the experiment when one wants to predict single-atoms dynamics and identify deviations from this dynamics due to strong interactions. The mechanical effect of the lasers on the ultracold atomic samples can also have important implications. Some parameters like the half width of the Rydberg spectra or the effect of the optical lattices on these spectra were obtained by the Rydberg excitation.

In this chapter the answers on all question concerning the stability and efficiency of our set up are presented. The experiments were partly conducted using

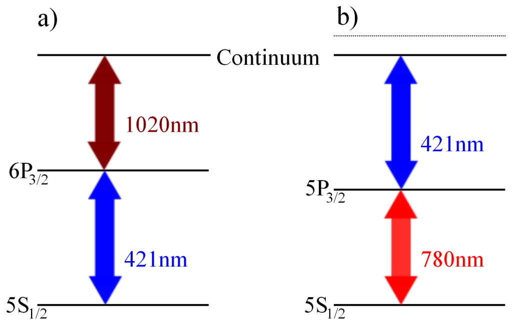

Figure 5.1: Photoionization schemes used in the experiments. In (a) standard 421 nm+1020 nm two photons transition. In (b) two photon ionization with 780 nm+421 nm lasers.

rubidium atoms trapped and cooled in magneto-optical traps and partly with Bose Einstein condensates.

5.1 Experiments in a Magneto-Optical Trap

Although the main purpose of this thesis is to present experiments conducted with samples that underwent Bose Einstein condensation, first measurements were done using ultracold atoms trapped in a MOT. Nowadays, magneto-optical traps are used as a source of cold atoms in many photoionization experiments to be here considered [28, 20, 1, 23, 65]. A big advantage of magneto-optically trapped samples is their availability as atoms in the MOT don't have limited lifetimes as they are constantly re-pumped. To perform experiments we used photoionization as it is a perfect tool to characterize, for example, ion detection efficiency or population dynamics. The photoionization of cold atomic samples of rubidium atoms trapped in a MOT was first studied by Dinneen et al [28]. Rydberg excitations are the second method of conducting measurements as it provides us with information about Rydberg spectra. It is convenient to use atomic samples trapped in a MOT because of their low density which results in interparticle spacing comparable with the dipole blockade radius.

To photoionize atoms from the MOT and BEC we use two photon transitions. Figure 5.1 presents two photoionization schemes used in our experiments. In figure 5.1 (a) the scheme used for most of our experiments is shown. In this case we use a 421 nm blue laser to excite atoms from $5S_{1/2}$ to $6P_{3/2}$ and 1020 nm to reach the ionization threshold. The second scheme (figure 5.1 (b)) makes use of the MOT beams to excite atoms to $5P_{3/2}$ and then 421 nm frequency to undergo ionization process. When this ionization scheme is used the MOT beams are always switched on, instead in the scheme when we use 421 nm+1020 nm configuration during the excitation the MOT beams are off.

The first scheme (figure 5.1 (a)) is also used to excite Rydberg states. The difference is the second step laser frequency tuned to the resonance with chosen n level. This procedure differs from the schemes reported by other research groups investigating Rydberg excitation in rubidium atoms[70, 67, 35, 58, 73, 33] that use the blue laser light as the last transition step tuned to excite Rydberg atoms. In our case, to change the Rydberg atom states the IR laser must be the tunable one.

5.1.1 Two photon MOT population losses

The photoionization of atoms in a MOT is a useful technique for measurements of detection efficiency, characterization and calibration of the set-up. Both ionization schemes introduced above have been used to create ions In the experiments described in this Section. In the first scheme of figure 5.1(a) atoms from the $5S_{1/2}$(F=2) ground state are excited by 421 nm blue light up to intermediate state $6P_{3/2}$. The ionization threshold (ionization limit) is the minimum energy required to ionize an atom and for ^{87} Rb it is $\sim$4.18 eV [69]. This limit can then be reached from the intermediate state by absorbing either a pulse of IR light or another blue photon. In figure 5.1(b) the alternative scheme is presented. The cooling lasers of $\sim$ 780 nm transfer population from $5S_{1/2}$(F=2) ground state to $5P_{3/2}$. Then a pulse of 421 nm laser light is applied.

The number of atoms N trapped in a MOT with the re-pumper laser on in continuous is almost constant (N$\sim$$10^9$). When the loading is switched off, the dynamics of the number of atoms is described by an exponential decay law with a time constant $1/\gamma$. The natural decay of atoms is caused, among others, by interactions with background gas in the science cell. The presence of ionization creates additional losses and so accelerates the atom number decay. The temporal evolution of the number of ground state atoms N in the MOT is given by following decay law [28]:

$$\frac{dN}{dt} = -\left(\gamma + \Gamma_{ion}\right) N. \tag{5.1}$$

where we have introduced the two photon ionization rate Γ_{ion}, produced by two different laser light frequencies as described by:

$$\Gamma_{ion} = g^{(2)} S^{(2)} \frac{I_1}{h\nu_1} \frac{I_2}{h\nu_2}, \tag{5.2}$$

where I_1 is the frequency and ν_1 is the intensity of the first laser and I_2 and ν_2 are intensity and frequency of the second one. The geometrical correction coefficient, $g^{(2)}$, introduced in reference [20] and taking into account the spatial distribution of the sample and the laser beam, is given by the ratio of the volume excited by the process of photoionization and the volume occupied by the atomic cloud. Assuming that the spatial distributions are of a Gaussian shape, $g^{(2)}$ results

$$g^{(2)} = \frac{1}{\sqrt{1+2\left(\frac{d_x}{w}\right)^2}\sqrt{1+2\left(\frac{d_y}{w}\right)^2}}. \tag{5.3}$$

This is true for a Gaussian laser beam with waist w, centered on a Gaussian atomic distribution with widths d_x and d_y. This factor has to be taken into account when less than the whole sample is subject to photoionization. The geometrical correction coefficient approaches unity when the size of the laser beam is bigger than to the size of an atomic sample.

During the photoionization experiment not every photon that hits atoms will photoionize them. $S^{(2)}$ determines the two photoionization rate for unitary fluxes of two laser beams. A cross section is typically introduced in the theoretical treatment of multiphoton ionization in order to describe the dependence of the loss rate, see for instance ref. [53]. In the situation when $g^{(2)}$ remains constant, the left hand side of equation (5.2) depends only on the product of the lasers intensities. This is valid only for weak intensities when shifts and widths of the intermediate states near resonance for the two photon process are not important [47]. If these conditions are not fulfilled $S^{(2)}$ is defined as a generalized cross section.

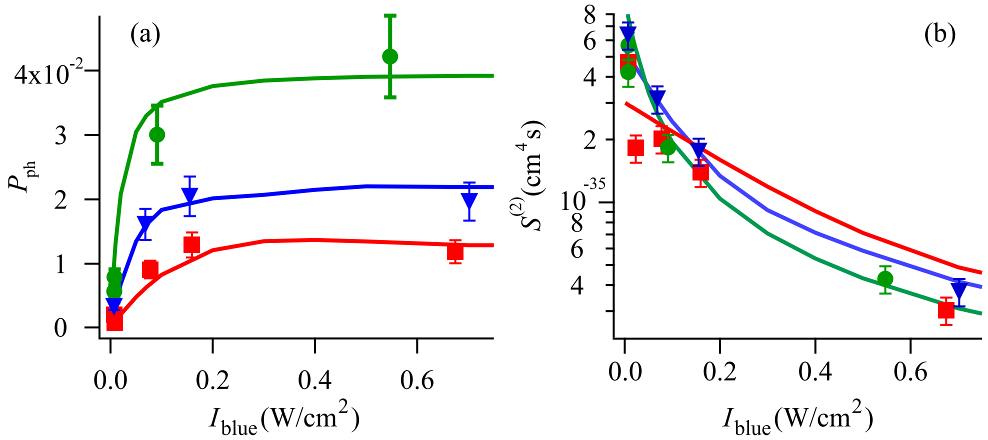

Figure 5.2: In (a), the P_{ph} photoionization probability per laser pulse, in (b) the unitary photoionization flux, $S^{(2)}$, as a function of the blue laser intensity I_{blue} at I_{IR}=2000 W/cm^2 and different pulse lengths (green circles τ_{pulse}=1 μs, blue triangles 0.5 μs and red squares 0.25 μs). The continuous lines represent theoretical predictions for those pulse durations. Both P_{ph} and S^2 were determined by measuring the temporal decay, γ, of the atoms from the MOT in the absence of photoionization and the decay, $\gamma + \Gamma$, in its presence.

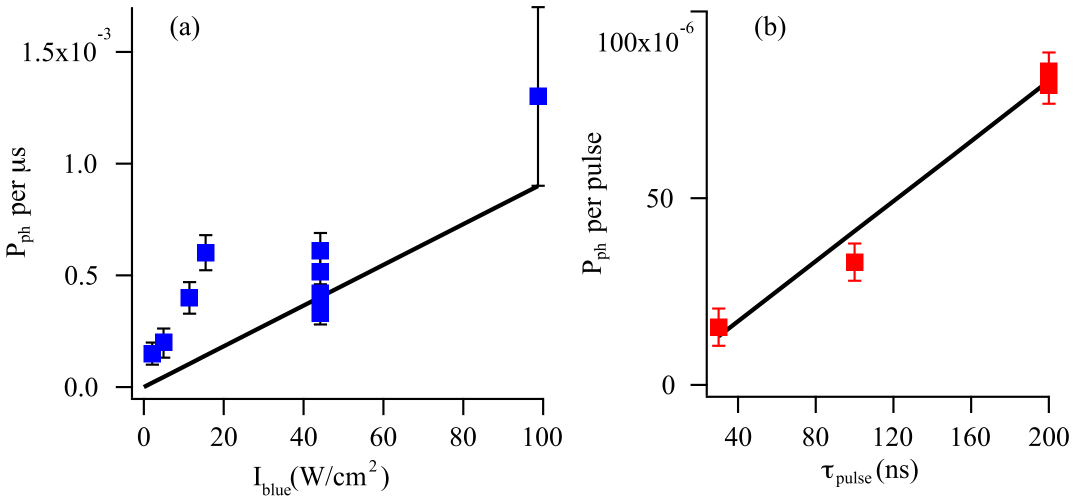

Figure 5.3: 780+421 nm photoionization, in (a) photoionization probability P_{ph} per μs as a function of blue laser intensity I_{blue} at fixed pulse duration of 1 μs. Figure (b) presents the photoionization probability P_{ph} versus the pulse duration τ_{pulse} for a fixed I_{blue}=44.2 W/cm^2. In both plots, the 780 nm laser intensity is 0.15 W/cm^2 and is detuned by -16.8 MHz from the 5S$_{1/2}$F=2→5P$_{3/2}$F'=3 resonance. The continuous lines represent theoretical predictions.

Initially to ionize atoms trapped in the MOT the first scheme of fig.5.1(a) is used. The sample is irradiated by 421 nm+1020 nm pulses of three different durations (0.25, 0.5 and 1 μs). Figure 5.2(b) presents the unitary flux photoionization rate, $S^{(2)}$, as a function of 421 nm laser intensity I_{blue}. The fact that $S^{(2)}$ changes with the intensity is justified by the influence of saturation and shifts on the 6P$_{3/2}$ level.

A photoionization probability, P_{ph}, is theoretically determined from the time evolution of density matrix equations for atoms interacting with two photoionizing pulses. The theoretical model developed in reference [1] is used to calculate the probability. It takes into account both states directly coupled by laser radiation and states involved in spontaneous emission cascade from the 6P to the 5S state, optical pumping into the 5S$_{1/2}$(F=1) is also considered. Without ground state depletion the photoionization probability is proportional to the duration of the pulse. The theoretical photoionization probability per pulse is plotted as a function of I_{blue} in figure 5.2(a). The dependence on the pulse duration is visible. The theoretical generalized cross section pulse is plotted as a function of I_{blue} in figure 5.2(b). Both plots in figure 5.2 are in good agreement with theory confirming our good control over the photoionization process.

We also measured atom losses from the MOT induced by photoionization via 5P$_{3/2}$. During the experiment blue laser intensities from 2 to 100 W/cm^2 are

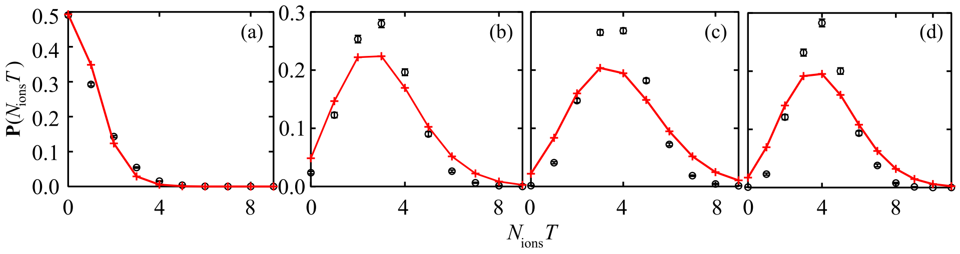

Figure 5.4: Probability P of detecting N $_{ions}$ ions for different pulse durations, τ_{pulse}, in the 780 nm + 421 nm photoionization configuration. From (a) to (d) τ_{pulse}=30, 100, 150, 200 ns. The 780 nm laser has intensity,0.15 W/cm^2 and detuning 16.8 MHz while the 412 nm laser has an intensity of 45 W/cm^2. Lines connect the values of the Poissonian fit to the data. From (a) to (d) the measured average value $\langle N_{ions} \rangle$ T of the collected ions is 0.8(1), 2.9(3), 3.7(4) and 3.9(4). The corresponding values determined from a fit with a Poisson distribution are 0.70(4), 3.0(2), 3.8(3) and 4.1(3).

explored. In the plot 5.3 (a) the P_{ph} probability per μs as a function of blue laser intensity is presented. Plot 5.3(b) reports probability P_{ph} per pulse versus the pulse duration at fixed intensity. On both plots the continuous lines represent theoretical predictions. In this case the MOT ionization rate is proportional to the product of the laser intensities. For each laser driven transition, the shifts and widths of the states are inversely proportional to the linewidth of the initial and final states. If the large laser intensity is applied to the transition from an excited state to the continuum the shift is negligible. This is due to the latter state very large linewidth. It is important to notice that during photoionization process the atomic cloud changes its volume. To analyze the atomic losses this change has to be taken into account. For this correction, it is assumed that the MOT operates in the constant density regime.

5.1.2 The Determination of the charge detection efficiency

During the experiment not all ions that are created and pushed toward the CEM will be detected. The electric field inside the cell is inhomogeneous and the detecting device is not placed exactly on the way of the ion flux. Therefore, precise knowledge of the detection efficiency is needed to perform quantitative measurements of ions collected on the CEM. From now on this parameter will be defined as ratio of ions created to ions detected on the CEM. Information about the detection efficiency can be extracted by determining photoionization losses and the average number of ions collected by the CEM measured as a function of the blue laser intensity. Such data allows the calibration of charge detection efficiency in the following manner:

- the number of atoms lost from the MOT due to the sequence of laser pulses is measured,
- the number of ions produced by the photoionisation pulse is calculated, based on the theoretical ionization probability,
- the measurement of the ions that reach the CEM is performed.

During this calibration it is important to perform the experiment at a low number of collected charges, in order to avoid a saturation of the CEM output. In order to improve the accuracy of the calibration process, we also compared the ion count directly to the MOT losses because that comparison does not require the determination of the laser parameters. To confirm the calibration of the average number of ions detected, a statistical analysis of the number distribution of the ion pulses at the CEM is applied. The ion distribution for different pulse duration are shown in fig 5.4. The mean number of atoms extracted from this distribution gives very good agreement with the mean number extracted from the average over a large number of laser pulses.

The ionization spectra shown in following part of this thesis, for instance in figure 5.11, are obtained using the configuration, presented in chapter 4 where lateral plates are not present in the set-up. In this configuration a maximal global detection efficiency of $T = 3(1)\%$ is measured. Instead the Poisson distribution presented in figure 5.4 is obtained in the configuration with lateral plates, figure 5.4 and results in an efficiency of $T = 35(10)\%$. We concluded that the presence of the lateral plates helps to guide ions toward the CEM. Both configurations are described in more details in chapter 4.

5.1.3 Rydberg excitation of atoms trapped in a MOT

To excite Rydberg states we have to tune the IR laser frequency to the frequency corresponding to chosen n state. For this reason it is necessary to check how well we are able to switch between quantum states by tuning the frequency of the IR laser in the range of its accessible wavelength. The results are presented in figure 5.5 where frequency scans of three different quantum states are shown.

To avoid populating the intermediate level 6 $\mathrm{P}_{3/2}$ that may cause incoherent excitation to the Rydberg state, the blue light has to be detuned. Scans of the Rydberg states with different detuning from the intermediate level are shown in figure 5.6. The peak at zero IR detuning is produced by the two-step process based on the resonant excitation of the intermediate $6\mathrm{P}_{3/2}$ state. The remaining peaks are produced by the two-photon process based on the off-resonant excitation of that

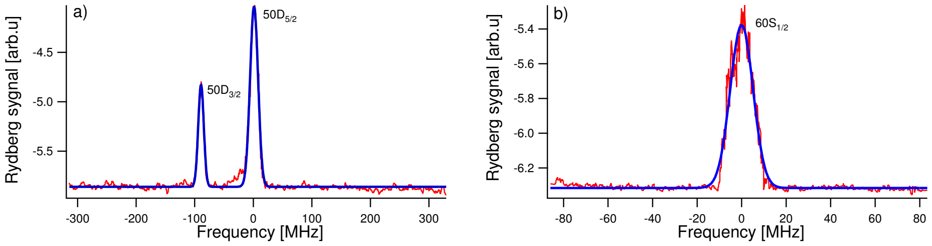

Figure 5.5: Rydberg level signals, in arbitrary units, as a function of second step excitation laser (IR) detuning for the blue laser resonant with the S→P transition. In (a) 50 D state is presented with its 3/2 and 5/2 fine levels. In (b) 60 $S_{1/2}$ level is shown.

state. The results indicate that already with the laser detuned from the resonance more than 300 MHz, the 6 $P_{3/2}$ resonant contribution (determined by the zero detuning peak) is minimal. These spectra are taken with the help of Box-car that integrates the ion signals.

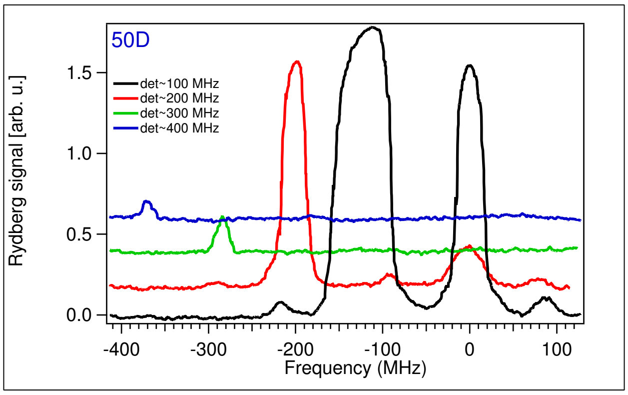

Figure 5.6: 50D level spectra as a function of IR detuning, for different blue laser detunings from the 6 $P_{3/2}$ intermediate state: 100, 200, 300 and 400 MHz. The zero detuning peak corresponds to two-step process, while the direct two-photon excitation of the Rydberg state corresponds to the peak on the left whose resonant position changes with the laser detuning.

5.1.4 The Stark shift

As explained in the chapter 2 Rydberg atoms are sensitive to electric fields. This sensitivity provides us with possibility of manipulating Rydberg atoms. The energy of a state depends on the applied field (Stark effect). In an electric field pure states are mixed. The external field can be controlled by applying different voltage into the plates. In our case good control over the electric field is important due to the glass cell and the possibility of involuntary charging up the cell. Because of this we cannot be sure that we control our fields very well. To check our control upon the electric field applied on the cell the dependence of the energy states on the applied field was measured. The constant electric field is applied during the excitations but before the field ionization. This field by acting on the atoms shifts their quantum states. In this way, by changing the voltage applied to external electrodes we obtain the Stark map of $81D_{3/2,5/2}$ states. By comparing obtained measurements with the theoretically calculated the Stark map we concluded to be able to apply the extra electric field between 0 and 150 mV/cm. These results presented in figure 5.7 (a) show that despite having the glass cell we still can apply controlled external field. In figure 5.7 (a), the case without the extra electric field is shown. It corresponds to the first point on the Stark map shown in figure 5.7 (b). From this we can deduce that the residual field in the cell is $\approx$ 10mV/cm.

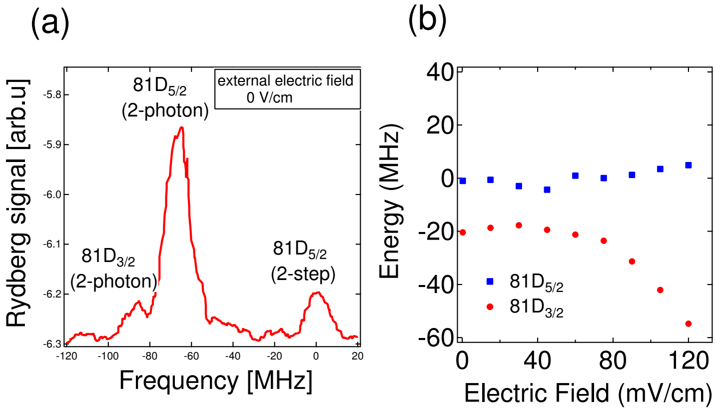

Figure 5.7: In (a) spectrum of the 81 D excitation in case of no applied external electric field and with the blue laser of the first step transition detuned by 60 MHz from the 5S→6P resonance. The two-step and two-photon peaks are observed. In (b) the Stark map of 81 D level is shown, blue squares correspond to the positions of the 81 $D_{5/2}$ and red dots to 81 $D_{3/2}$ as a function of electric field.

In order to study the electric field that may build up during the excitations we voluntary charged the cell. The field builds up in the cell when the electric pulse is too long (more than a few ms). Charges accumulate on the cell creating an extra electric field acting on the atoms. In figure 5.8, the effect of this electric field is shown. After a 5 s pulse of the electric field is applied on the plates. The spectral line of the 81 D level is taken every few minutes and its shape is compared to the case where the extra field is not present, see figure 5.7 (a). It is clear that the

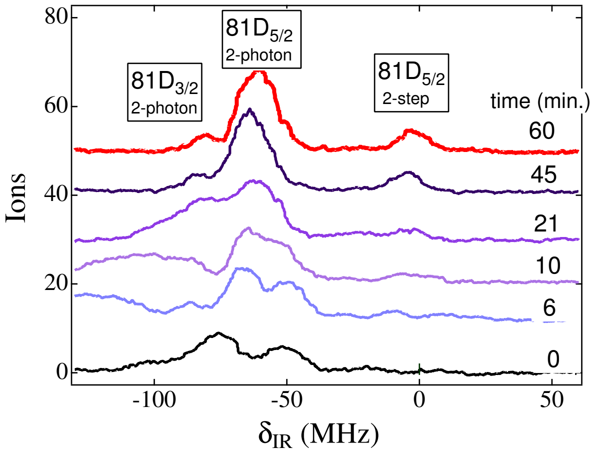

Figure 5.8: (a) Time-evolution of the spectral lines of 81 D state. The cell was first charged for 5 s and then left to freely discharge. Spectral line scans were taken every few minutes. The blue laser light was 60 MHz detuned from the intermediate state $6P_{3/2}$.

induced electric field broadens the lines, so clear resonant peaks of $D_{3/2}$ and $D_{5/2}$ are hard to distinguish, and their positions are shifted compared to the zero field case of figure 5.7 (a).

The residual electric field is hard to defined as it change on a daily basis but from several measurement one can say that it is on the order of 10 mV/cm.

5.1.5 The Determination of the Rabi frequency

While dealing with Rydberg atoms excitations it is important to know Rabi frequencies of both steps of the transition, especially when one needs to predict single-atom dynamics or consider deviations due to e.g. blockade effects. Also knowledge of the Rabi frequencies is essential for efficient Rydberg excitation. The Rabi frequency is proportional to the transition dipole moments μ_{eg}. The Rabi frequency of the first step transition Ω_1 can be easily measured experimentally by Autler-Townes spectroscopy for ultracold atoms. This was already demonstrated in reference [5]. To observe the Autler-Townes effect it is necessary to use two lasers. The first one (420 nm) drives the transition between two states, in our case $5S_{1/2}$ and $6P_{3/2}$. Therefore, theses states are considered as dressed states. Then, the transition to the Rydberg level is done using the second laser (1010-1030 nm). This laser should have a weak power so the Rydberg state remains unaffected by the applied lasers. By scanning the frequency of the second laser, we observe the splitting of the resonant line of the first step of the transition. This measurement

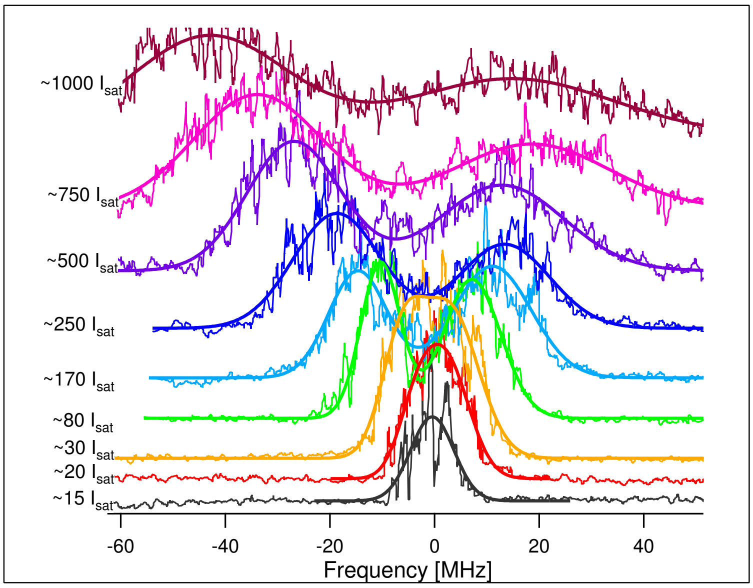

Figure 5.9: Spectrum showing the Autler-Townes split 6P $_{3/2}$ state probed by a transition to the state 52S$_{1/2}$. The strength of the probe transition was varied by varying the light power of the 421 nm laser. The blue laser was resonant with the 6P$_{3/2}$ state.

is conducted for different blue laser light intensities I_{blue} in the range from 15 to 1000 I_{sat}, where I_{sat} equals to I_{sat}=2.3 mW/cm^2. The spectra are taken at constant IR laser intensity I_{IR} of 400 mW/cm^2. Figure 5.9 presents measurements of the Autler-Townes splitting of the 6P$_{3/2}$ state. The splitting between two lines for a power of the blue laser P_{blue} $\sim$9 mW results in a Rabi frequency in the order of Ω_{blue}=2$\pi\times$41 MHz. Calculations using:

$$\Omega_{blue} = \Gamma\sqrt{\frac{I_{blue}}{2I_{sat}}}, \tag{5.4}$$

gives the value Ω_{blue}=2$\pi\times$35 MHz. This discrepancy is due to an imprecise knowledge of the laser beam waists and the experimental error of the power measurement. Table 5.1 presents values of Ω_{blue} for different values of blue laser power. The second step of the Rydberg excitation was determined from the dipole coupling of the two states. During this measurements the Rabi frequency of the second step transition was set to be Ω_{IR} =2$\pi\times$80 kHz.

While measuring the Rabi frequency of the first step of the transition some interesting phenomena were observed. The excitation spectra are asymmetric and broadened, see figure 5.9. The position of the mid point between the peaks is shifted toward the lower energies. However, the Autler Townes theory does not

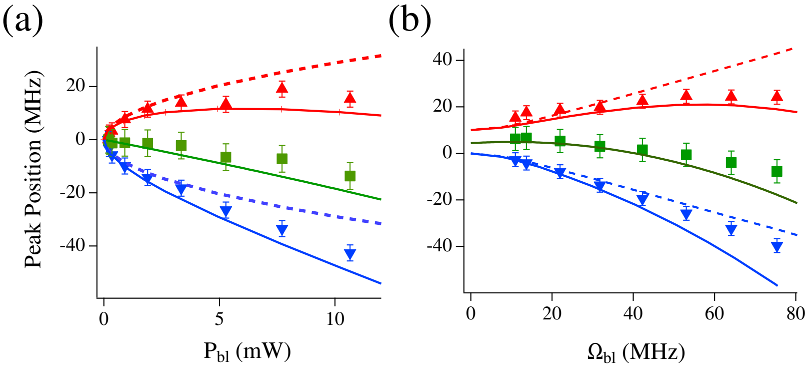

Figure 5.10: The Autler Townes peaks positions (red and blue triangles) and the central point of the spectrum (green squares). The dashed lines (red and blue) present the theoretical calculations of the Autler Townes splitting and the green continuous lines the determinations of the shifts from the electric field created by the ions, as discussed in the text. In (a) the first step transition is on resonance with the $6P_{3/2}$ state and results are plotted against power of the blue laser beam. (b) The first step of the two photon transition was detuned by -10 MHz from resonance and results are plotted as a function of the Rabi frequency Ω.

Table 5.1: Calculated values of Rabi frequency Ω_{blue} for different blue laser powers.

Power of 421 nm (mW)	$\Omega_{blue}/2\pi$ (MHz)
0.2	5.3
0.45	7.8
1.85	15
2.9	19
4.2	23
9.2	35

predict the shift of the central point and its position should be constant. Also the split peaks show a tendency to move toward lower frequencies. From a theoretical analysis it becomes clear that an electric field created by ions produced by the blue laser photoionization is responsible for the shift. A model that assumes evenly spread out ions creating the electric field confirms the previous results. To estimate the electric field acting on the sample the number of ions produced by the blue photon ionization was calculated. Then assuming all ions remain within the MOT volume the average field was calculated. In this way the Stark shift was estimated. During our experiment the first step excitation laser was on resonance or closely detuned (-10 MHz) with the intermediate $6P_{3/2}$ state. An electric field created by ions produced during excitation to the Rydberg state shift atomic states and in the result the observed Autler-Townes peaks are also shifted. In figure 5.10 one can see that experimental and theoretical results are in good agreement. The discrepancies between the model and the results are caused by the definition of the volume occupied by ions and the fact that the field is not homogeneous.

For $\delta_{bl} = 0$ the two peaks should have the same height, and instead the red shifted one is more intense. This asymmetry was observed also for the spectra recorded at $\delta_{bl} \neq 0$. We don't have a clear explanation of the asymmetry. In addition, one needs to take into account that ions are not distributed uniformly and their spatial distribution follows the Gaussian profile of the blue laser and, therefore, the created electric field is not homogeneous. Due to this field dishomogeneity the split peaks are much broader than what expected from the Autler-Townes theory.[1]

5.2 Two photon transition in BECs.

Since the main part of this thesis deals with Rydberg excitations of Bose Einstein condensate samples, we performed a series of preliminary experiments aimed on comparing two photon excitations in the MOT and in BECs in order to understand how they differ from each other.

5.2.1 Ionization of BECs

In this subsection ion losses and ion creation are presented. The experiments are done using the same laser parameters that are used while conducting experiments in the MOT. No difference between the BEC and cold atoms trapped in the MOT is seen. Nevertheless, during the analysis of BEC atom losses, the existence of

---

[1] The spread of the dipole moment values associated with various m_F-sublevels could also contribute to the apparent broadening.

thermal atoms following spontaneous emission from the excited state should be considered.

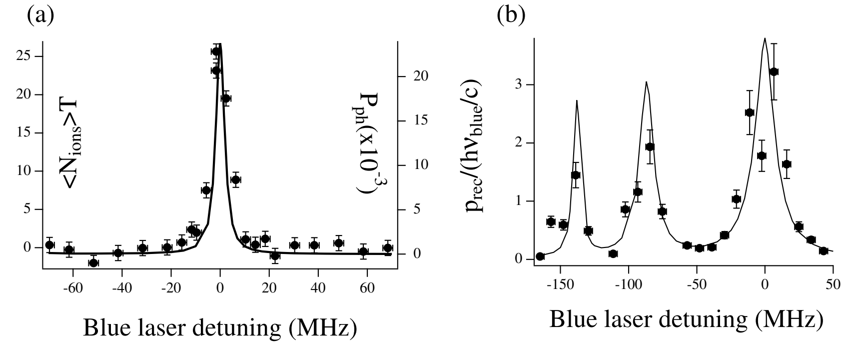

Figure 5.11: In (a) ion spectrum produced by BEC photoionization using 421+1020 lasers versus blue laser detuning, the I_{IR} intensity being constant. Each data point is taken with a laser pulse with intensity I_{blue}=0.12 W/cm^2 and I_{IR}=2000 W/cm^2. The continuous lines, and the right scale, represent the theoretical calculations of photoionization probability P_{ph}. In (b) spectrum of the momentum recoil p_{rec} imparted to the BEC against blue laser frequency is presented. Each data point is taken with a laser pulse with intensity I_{blue}=4 W/cm^2 and I_{IR}=2000 W/cm^2. The continuous line shows the calculated value of the momentum p_{rec}. The peaks are produced by the hyperfine structure of the 5P$_{3/2}$ state. The zero detuning corresponds to the 5S$_{1/2}F = 2 \rightarrow$ 5P$_{3/2}F' = 3$ hyperfine transition in appears

The number of ions produced during the photoionization process of the BEC of around 10^4 atoms, is plotted in figure 5.11 (b). The transition scheme presented in figure 5.1(a) is used. To begin, the average collected number of ions $\langle N_{ions}\rangle T$, with $\langle N_{ions}\rangle$ the number of produced ions, as a function of 421 nm laser detuning is measured. The wavelength of the second step laser is fixed. Each point in the figure corresponds to several BEC realizations. During this experiment we measured the integrated ion signal. Then the calibration of the signal has to be done by comparison with a single ion signal. Furthermore, these data are compared with the solution of the time evolution of the density matrix for the two photon ionization case. The continuous line plotted in figure 5.11 (a) represents the theoretical photoionization probability P_{ph}. The vertical scale on the right hand side is chosen to match the ion signal (scale on the left). The line broadening of 3 MHz was observed.

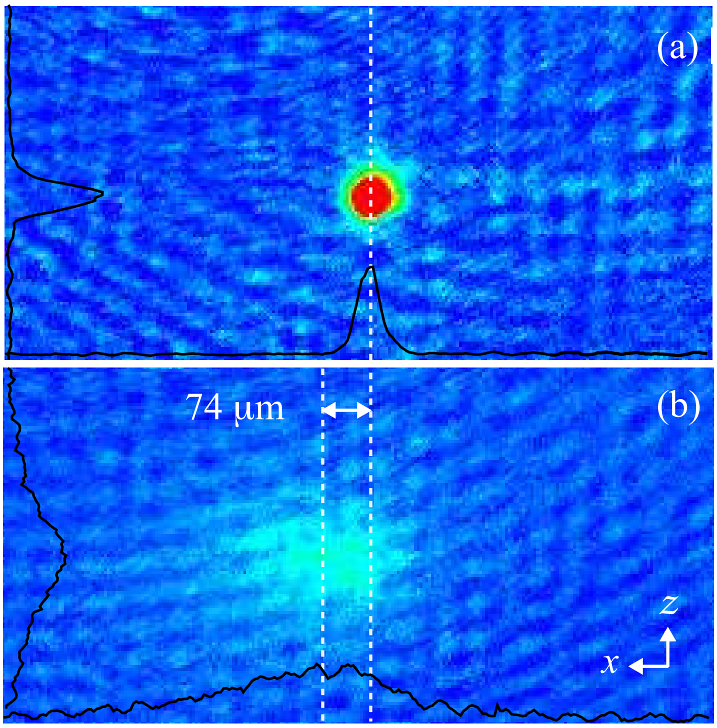

Figure 5.12: In (a) BEC absorption image, after 6.3 ms of time of flight. The vertical line indicates the atomic cloud center. In (b) absorption image of the ultracold atomic cloud irradiated by 0.3μs 421 nm laser pulse with intensity I_{blue}=0.7W/cm^2. The vertical lines indicate the new cloud center and the original one.

5.2.2 Mechanical effects of photoionization laser

The momentum transfer from the blue photons to the condensed atoms has also an effect on the shape of the BEC. While performing measurements on the BEC deformation of the BEC is observed. The image of a BEC cloud with its spatial distribution before laser ionization and after 6.3 ms of time of flight is presented in figure 5.12 (a). The BEC presented in figure 5.12 is 14$\times$14μm large.

In figure 5.12 (b) instead, an image of the ultracold atomic cloud after a 0.3 μs pulse composed of 421 nm and 1020 nm lasers is shown. Photoionization pulses strongly affect the ultracold atomic cloud by means of the following process:

- BEC absorbs a blue photon and recoils in opposite direction with momentum p_{rec},
- BEC spontaneously emits absorbed photons in the random directions,

- atoms get converted into a thermal cloud following spontaneous emission from the excited state and the resulting spatial distribution of the atomic cloud is broader.

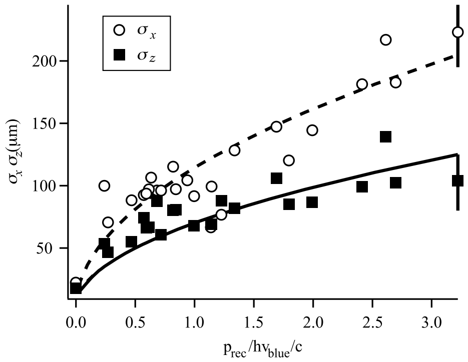

Figure 5.13: Spatial widths σ_x and σ_x (in μm) of the atomic thermal cloud created by blue photon absorption versus the momentum recoil p_{rec} imparted to the ultracold cloud.

A broadening of the momentum distribution is visible in the x direction of propagation of the irradiation but also in the vertical z direction. The spatial distribution of the atomic cloud is composed from the narrow BEC part and much broader thermal cloud, as in the spatial profiles reported in figure 5.12(b). Figure 5.13 reports the measurements of the σ_x width of the cold cloud in the horizontal direction and σ_z in the vertical. The thermal cloud broadening is proportional to the square root of the atomic recoil. The momentum transfer by the IR photons is negligible compared to that due to the blue photons. In figure 5.11 (b) reports experimental and calculated recoil momentum p_{rec} versus the blue laser detuning. In the plot, zero detuning corresponds to the $5S_{1/2}$(F=2)→$6P_{3/2}$(F'=3) transition. The visible resonant peaks match the F'=1, 2, 3 hyperfine states of $6P_{3/2}$. The theoretical prediction shows a very good agreement with the experimental points.

5.2.3 Rydberg spectra in BECs

It is important, to measure the widths of spectral lines of the Rydberg state. In this case we investigate the 53 D level. We used low density BECs to avoid strong interactions that could affect the result. The procedure used to create low density BEC samples is presented in more details in chapter 6. Firstly, the BEC is loaded into one arm of dipole trap while simultaneously switching off another one. Then the atoms are left to expand for 100 ms in the horizontal direction. In this way, the BEC is more than 300 μm wide. Figure 5.14 presents the number of ions

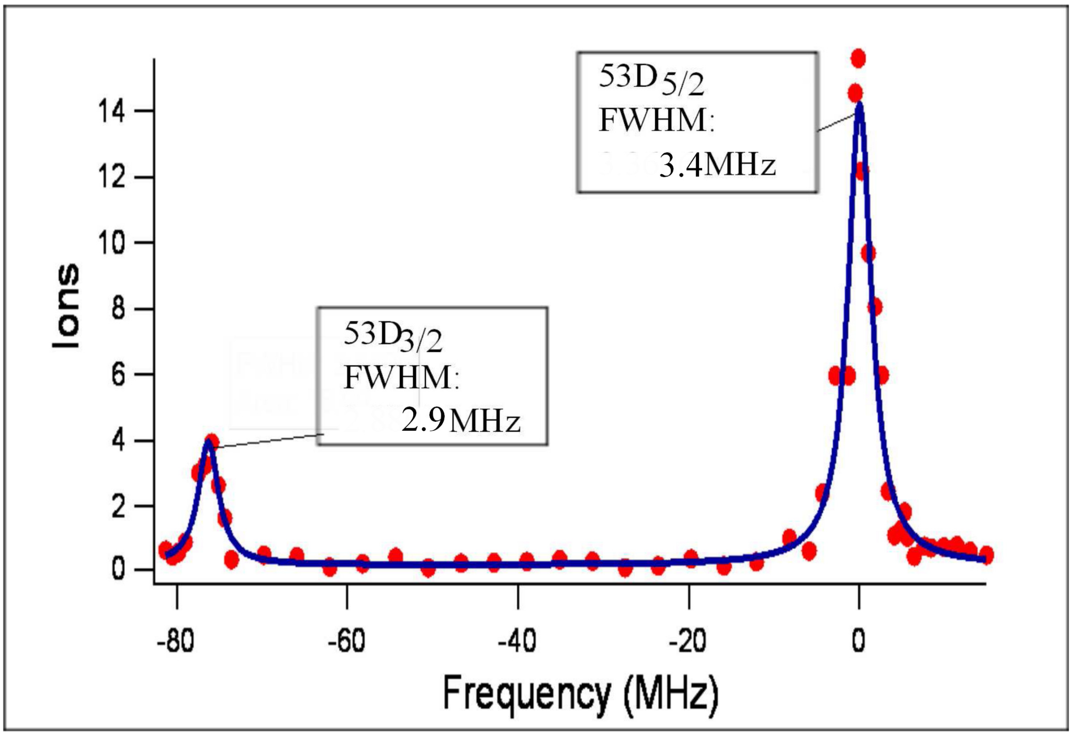

Figure 5.14: Number of ions detected by the CEM as a function of the IR laser detuning. Zero corresponds to the $6P_{3/2}$(F=3)→$53D_{5/2}$ transition. The frequency of the first step transition was detuned 500 MHz from the resonance. The intensity of the blue laser is I_{blue}=15 W/cm^2 and of the IR laser I_{IR}=160 W/cm^2.

detected by the CEM versus detuning of the 1020 nm laser light. Each point in figure 5.14 is an average of 3 measurements where 15 excitation impulses are shot in each realization of the BEC. The intensities of both lasers are constant for the duration of the experiments. The visible peaks correspond to the $D_{3/2}$ $D_{5/2}$ levels. As shown in figure 5.12 both peaks have a Full Width at Half Maximum (FWHM) around 3 MHz. The FWHM value given by the spontaneous decays corresponds to ≈0.4 MHz. The discrepancy is due to the dipole blockade and the linewidth of the excitation lasers.

5.3 Rydberg atoms in optical lattices

In the following chapters we will deal with Rydberg excitations of a BEC loaded into optical lattice created by 840 nm laser light, therefore one interesting point for future experiments was to check if lattice lasers beams are going to affect the spectral lines of the Rydberg states. In order to be sure that this radiation is not

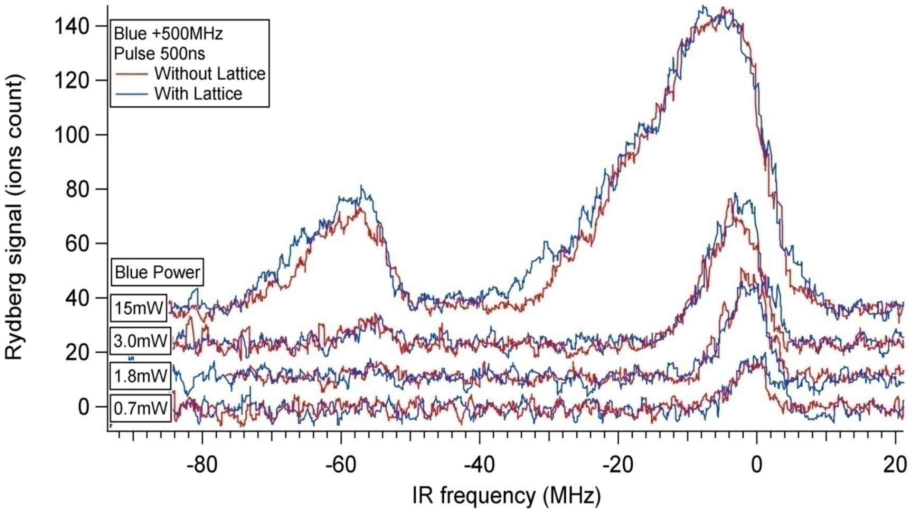

Figure 5.15: The spectral line of the $53D_{3/2,5/2}$ state. Atoms trapped in the MOT are irradiated by the 500 ns pulse of 421+1020 nm. The blue laser frequency is detuned by 500 MHz into the blue. The blue line corresponds to the case where the lattice lasers were applied and red one to the case without optical lattice.

going to affect Rydberg levels we excited Rydberg atoms in the presence of the 840 nm radiation. The experiments were performed using the atoms trapped in a MOT. The excitation pulse of 500 ns was applied and the 421 nm blue laser frequency was detuned by 500 MHz. Different intensities of the light were explored. In figure 5.15 the spectral lines of the 53 D sate are taken for different intensities of the blue laser. Spectra are taken by scanning the frequency of the second step transition. For each value of the blue laser intensity the scan is done with and without the lattice lasers. As shown in figure 5.15, the lattice laser beams don't introduce any shifts or broadening to the spectral lines of the Rydberg states. In a similar way we checked if the 1030 nm laser that creates the dipole trap does not introduces any effect to the spectral lines and the result was negative.

5.4 Conclusions

In this chapter a series of experiments was performed. Their purpose was to define several experimental parameters and to show how the future measurement can be affected. In the first section the experiments in the magneto-optical traps were described. A new experimental configuration for ionization and charge collection has been described and characterized. The efficiency of ionization was measured giving a value of 3(1)% for the configuration without lateral plates and 35(10)%

when the lateral plates were present. Furthermore, the Stark shift experiment allowed us to obtain an approximate value of the residual field in the experimental cell, on the order of 10 mV/cm. This experiment showed that we have very good control upon the applied external field. Furthermore, the losses observed for ultracold samples were presented.

The second part of this chapter was devoted to experiments in Bose Einstein condensates. First, the ionization spectra produced from a BEC have been presented. In the second part, some results on the Rydberg atom excitation were examined. The half line width of the Rydberg atom spectra of around 3 MHZ has been measured. In the last part of this chapter the Rydberg excitation of ultracold atoms inside optical lattices has been presented showing no heating effect due to the lattice lasers on the Rydberg spectra.

Chapter 6

Dipole Blockade Effect in ultracold atoms

An intriguing phenomenon arising from strong Rydberg interactions is the dipole blockade [44, 51]. The blockade effect is often presented in the context of quantum information processing, due to the fact that state dependent interactions are important for the creation of two qubit quantum gates [13]. This blockade phenomenon has been extensively studied both theoretically [4, 17] and experimentally in different atomic ensembles: cold atomic clouds [72, 39], single atoms [73, 33] and BECs [38]. The strong Rydberg-Rydberg interactions have been studied in the context of gases and the first experimental results presented a nonlinear dependence on the number of excited atoms as a function of increasing power of the excitation lasers and atomic density [72, 67]. Later research in high density regimes shows that one can also observe coherent collective excitations [39, 39, 33, 45]. The experiments presented in this thesis provide experimental information about the dipole blockade effect in Bose Einstein Condensates. Much stronger interactions in thermal samples are expected in BECs than in the thermal samples due to their higher densities. The blockade effect can be observed both using BEC samples of varying sizes and through the counting statistics, where the Mandel Q factor is an indicator of a sub-Possonian counting distribution expected in the strongly interacting regimes.

This chapter discusses experiments on the Rydberg excitation of atoms from Bose-Einstein condensates to Rydberg states. The results on dipole blockade measurements in BECs are reported. The experiments explored different BEC density regimes and their influence on Rydberg atoms production, (section 6.2). In the later part of this chapter we present the duration of the excitation pulse, (section 6.3). In the further part of the chapter results on counting statistic of ultracold atoms are presented (section 6.5).

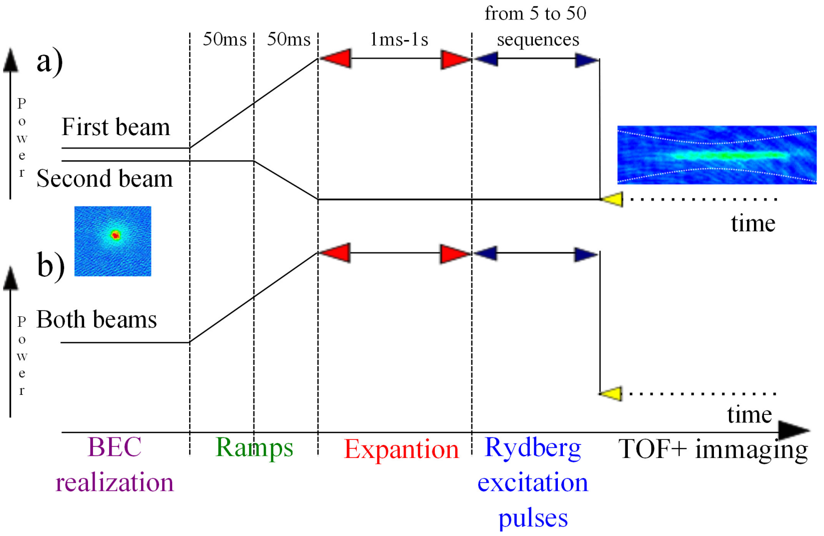

Figure 6.1: The experimental time sequence: (a) To expand the BEC, the atoms are loaded into a one of the arms of the dipole trap. (b) To squeeze the BEC, the powers in the dipole trap laser beams are ramped up. Squeezed or expanded BECs are then subject to excitation to Rydberg states and are imaged after a time of flight.

6.1 Experimental procedure

In the experiments presented in the following part of this chapter we aimed at measuring the Rydberg signal obtained from various sample sizes. Realization of condensates with different sizes combines the techniques of Bose Einstein condensation presented in chapter 3 with a method of changing condensate size. To obtain different sample sizes one can expand or squeeze the volume of a BEC, keeping constant the number of atoms in a sample. With the close to constant number of atoms when we change the size we change in effect the density of the sample.

The process described in chapter 3 results in Bose Einstein condensates with densities in the range of 10^{12}-10^{13} cm^{-3}. To experimentally achieve a Bose Einstein condensate with lower densities, so with bigger sizes, we expand the BEC in one arm of the dipole trap. At the final stage of evaporation the second dipole beam power is ramped down and atoms remain in only one arm of the trap whose power is ramped up in order to increase its radial trap frequency. Then the condensate is left for several milliseconds to expand in the horizontal direction, its size is denoted as σ_{BEC}. By changing this expansion time, τ_{exp}, one can chose the final size of the sample. An increase of τ_{exp} leads to an almost linear increase of

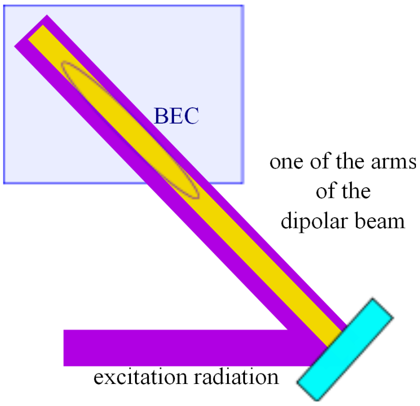

Figure 6.2: Optical path for Rydberg excitation radiation. Samples confined in one arm of the dipole laser are irradiated from along the direction of the dipole trap beam.

the size of BECs. In figure 6.1(a) the experimental time sequence of the expansion experiment is presented.

Smaller sizes of the sample are obtained by squeezing the sample confined by both arms of the dipole trap. The minimum size corresponds to the maximum applicable power to each arm of the dipole trap. The time sequence of this experiment is presented in figure 6.1(b).

After a realization of the sample with the chosen size, a Rydberg excitation pulse is performed. Each excitation/detention sequence consists of blue and IR laser pulse, field ionization and ions detection. The total duration of one sequence cannot be shorter than 42 μs due to a charging effect on the glass cell. If this time was shorter the cell would not have time to discharge and in the effect the experiment would be conducted in the presence of an external electric field. The minimum duration of the laser irradiation is limited to 30 ns. This value comes from the raise time of the Acousto-Optics Modulator.

To excite the sample, the two photon scheme described in chapter 4 was used. The first step of the transition was blue detuned by 500 MHz from the intermediate $6P_{3/2}$ state.

Typically, for each expansion time three realizations of a BEC, each with at least 15 excitation sequences were done. Then the number of the detected Rydberg atoms was averaged and plotted against the size of a BEC.

In all the experiments the irradiation beam was aligned along the dipole trap of beam that contained the expanding atoms, see figure 6.2. This alignment maximizes the overlap between the sample and the beams.

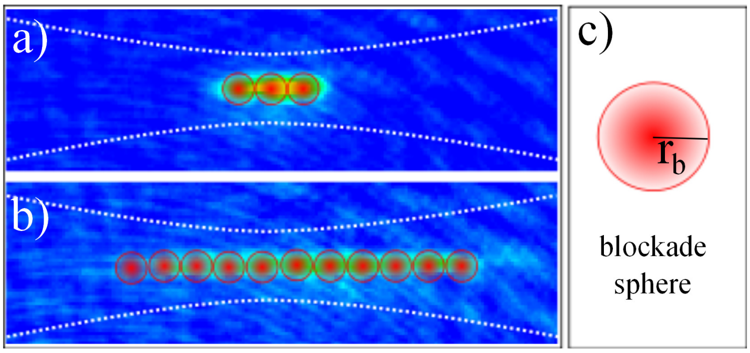

Figure 6.3: (a) and (b) present BEC expanded for different time, t_{exp}.(c) Transverse area of the blockade with the blockade radius, r_b. The spheres indicate the dipole blockade radius. The white doted lines represent the dipole trap beams.

6.2 Dipole Blockade in the expanded BEC

The experiment was performed to investigate the dependence on the size of the condensate of the number of Rydberg atoms that fit into the atomic cloud. This then could be used as a new method of measuring the dipole blockade radius. Measuring the collected ion number and knowing the efficiency of the collection one can calculate the number of Rydberg atoms created in a BEC. By changing the length of the elongated cloud between a few microns and several hundreds of microns we observed an increasing number of Rydberg atoms as more blockade spheres fit into the one-dimensional chain.

The dipole blockade effect described in chapter 3 is characterized by the blockade radius r_b. In a region dictated by this radius at most one Rydberg excitation can be present. In the 3D model this region is defined as a sphere and is discussed below. The 1D model can be viewed as a chain of Rydberg atoms separated by the average distance $d = 2r_b$. Therefore, while expanding the sample more blockade areas can fit into it resulting in exciting larger numbers of Rydberg atoms. While the BEC expands it takes the form of a tube with a radial size of around 3μm, which is less then the dipole blockade radius for any n state used in the experiments described in this chapter. The radial size of a BEC can be calculated using the formula for the width of a wavefunction of a particle in a trap assuming negligible interactions in the ground state [63]:

$$a_i = \sqrt{\frac{\hbar}{m\omega_i}} \approx 3\mu m, \tag{6.1}$$

The trap frequency ω_i in our case is around 50 Hz and corresponds to a dipolar beam power of 280 mW.

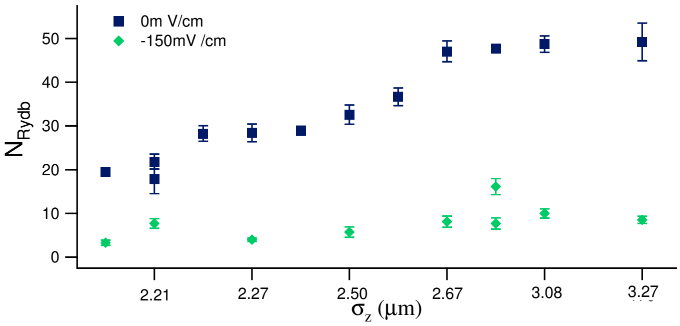

Figure 6.4: The dependence of the number of Rydberg atoms N_{Ryd} on the measured radial size of the atomic cloud, σ_z, without (squares) and with (dots) an external electric field of 150 mV/cm.

If one takes into account this value the sample can be described as 1D system. To confirm that we work in an effective 1D system we performed an experiment where the horizontal size of a sample was kept constant. Instead the radial size was changed by changing the temperature of the sample leading to a larger radial size for higher temperature values. It can be concluded from figure 6.4 which presents the dependence of the number of Rydberg atoms on the radial size of the sample, that in the range between 2.2 μm and 2.5 μm we operate in 1D system as the number of the excited atoms does not change. Going to wider samples that correspond higher temperature values, one observes the linear grow in the number of detected Rydberg atoms and constant number of Rydberg atoms from 2.7μm signalizing that 3D regime has been reached.

Furthermore, we were interested in what happens when an external electric field is acting on atoms. We know that in a case of our setup the residual electric field is present in the cell. The measurements were performed in the same way that measurements presented above but in this case an external electric field of $\approx$ 150mV/cm was applied. From the figure 6.4 (green diamonds) one can observe the effect of the field as a suppression of detected Rydberg atoms due to the increased size of the blockade radius.

Measurements of the number of Rydberg atoms against the size of the condensate were conducted for different n states. For all of them the dependence of the number of Rydberg atoms, N_{Rydb}, on σ_{BEC}, the size of the BEC sample, was plotted. Each point presented on the plots is a result of averaging three BEC realizations, each of 50 sequences. To calculate the number of Rydberg atoms produced an efficiency of 35% was assumed, see chapter 5. Figures 6.5 a), and b) present dependence of the number of excited Rydberg atoms on the size of the BEC for the chosen n states. The number of excited atoms increases with increasing the horizontal size of the BEC. Measurements of the $53\mathrm{D}_{5/2}$ state were repeated and showed good agreement between each other, see figure 6.5 b).

As can be seen in chapter 2 the Van der Waals interaction coefficient C_6, scales as n^{11}. So by imposing the C_6 proportionality to n^{11} in the $\frac{C_6}{R^6}$ therm, we obtain for the average Rydberg-atom separation $d = r_b \propto n^{11/6}$. This is true only when no electric field acts on the atoms. In the case when an external electric field is applied the average Rydberg-atom separation $d = r_b \propto n^{11/6} + n^{4/3}$ where $n^{4/3}$ is obtained by imposing the C_3 proportionality to n^4 in the $\frac{C_3}{R^3}$ therm. In the case of our experiment some residual field is present in the cell after switching off the plates and the grid. The presence of such a electric induces dipole dipole interactions which increases the dipole blockade radius r_b. Even if this field is on the order of 10 mV/cm, it causes small change of the measurements and the blockade radius. Nevertheless it has to be taken into account when one wants to obtain a good agreement between experimental and theoretical data. While calculating the number of detected Rydberg atoms, N_{Rydb}, the factor 1/2 was also taken into account. This factor comes from excitation probability of a Rydberg state. Each blockaded sphere should be considered as an effective two level system where only one atom in the sphere can get excited. However, we need to consider that we are collectively exciting atoms inside the blockaded area and therefore, the probability of excitation is equal 1/2 as we average over all the excitations. The effect of the external electric field on the atoms is presented in figure 6.6. This measurement was conducted for the $66\mathrm{D}_{5/2}$ state. The number of created Rydberg atoms was measured for different sizes of the condensed cloud without any external electric field (red line) and with an electric field of $\approx 150\mathrm{mV/cm}$ created by -10 V applied to the front plates (green line). From the figure 6.6 one can clearly see than when the field is applied the number of Rydberg atoms N_{Ryd} is much lower than in the case without the field, resulting in a higher dipole blockade radius r_b. As the Rabi frequency scales with the $\sqrt{N}$, where N is the number of atoms in the blocked region to keep the the pulse area fixed we had to adjust the time of the pulse for each size of the sample.

Figure 6.7 presents the blockade radius r_b as a function of the quantum number n. The experimental data are in good agreement with the calculated values. To fit the experimental results of the blockade radius against the n state both Van der Waals and dipole dipole interactions were taken into account.

To confirm obtained results we have compared the normalized number of excited Rydberg atoms, N_{Rydb}, to the saturation value N. The results present in figure 6.8 show good agreement between the curves of the $53\mathrm{D}_{5/2}$ and the $78\mathrm{D}_{5/2}$ states.

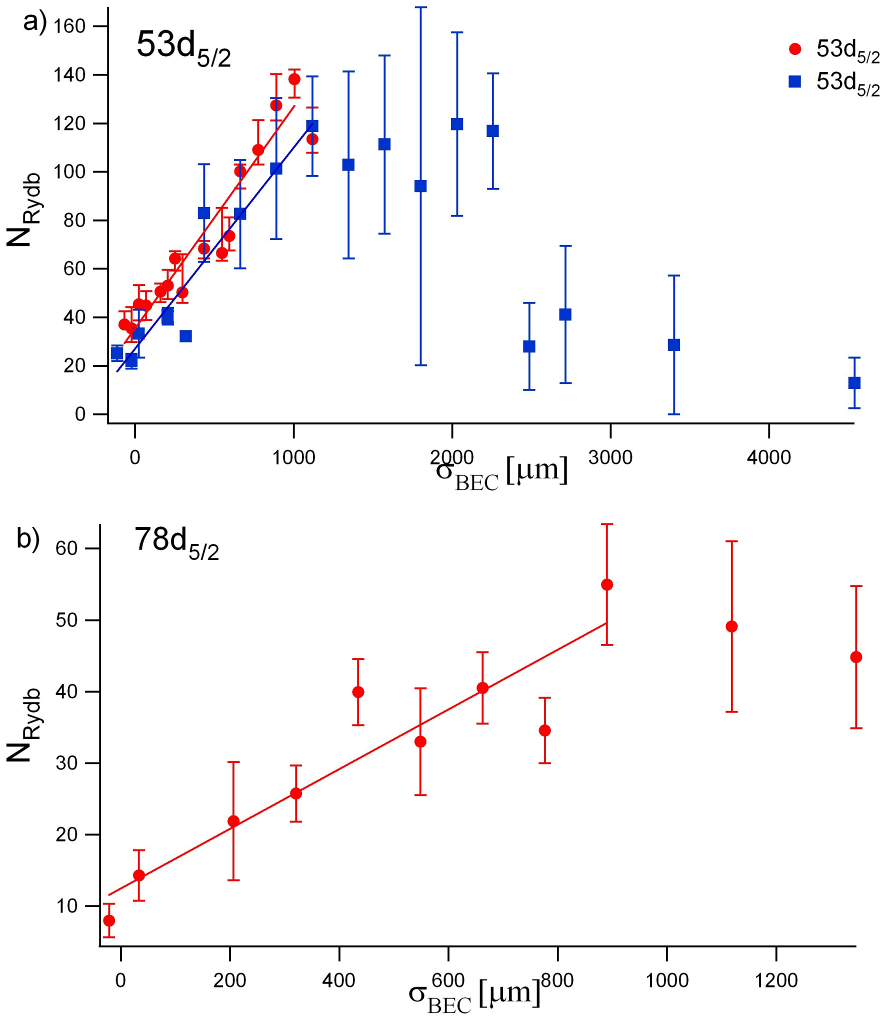

Figure 6.5: Number of excited Rydberg atoms, N_{Rydb}, as a function of the size of the sample, σ_{BEC}, for the a) 53D$_{5/2}$ and b) 78D$_{5/2}$ states. From these plots one can derive the blockade radius r_b.

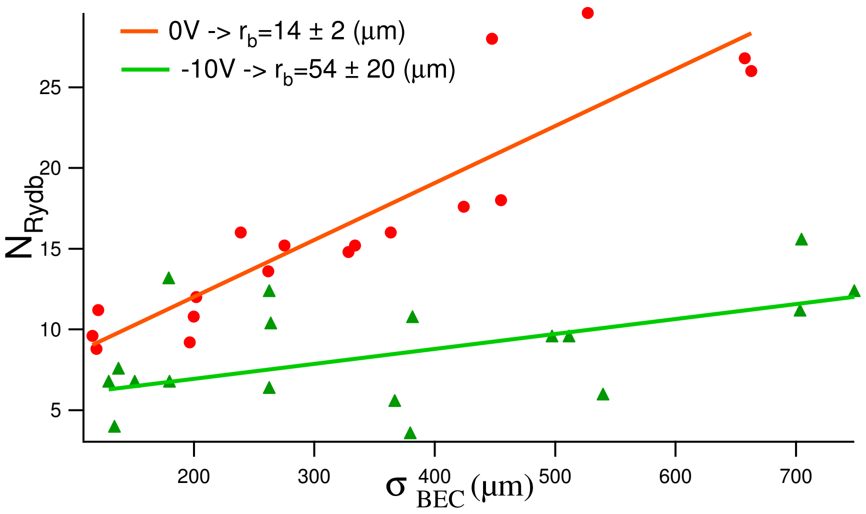

Figure 6.6: Number of excited Rydberg atoms, N_{Rydb}, as a function of the size of the sample, σ_{BEC}, for the 66 $D_{5/2}$ state. The dots present measurements conducted without presence of an external electric field. Instead triangles indicate Rydberg excitations in presence of such a field. The measured values of the dipole blockade radius for the 66 $D_{5/2}$ state were: without presence of an external electric field 14 ± 2 μm and 54 ± 20 μm with the applied field of 150 mV/cm.

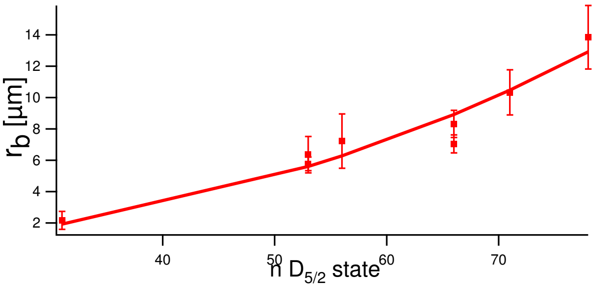

Figure 6.7: Dipole blockade radius as a function of the principal quantum number n. The red dots represent data obtained experimentally and the red line corresponds to theoretical fit that takes into account both Van der Waals and dipole-dipole interactions, the quantum defect being taken into account, as in ref. [22]. The results were obtained without an external electric field; however the residual electric field was taken into account. The linewidth of the excitation laser was 300kHz.

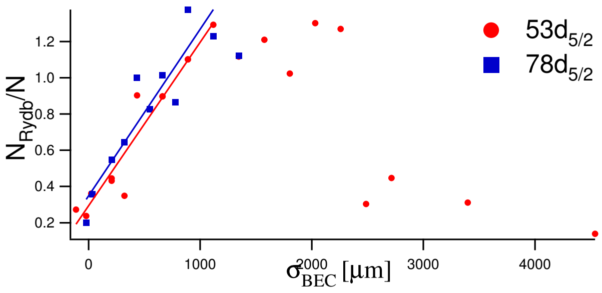

Figure 6.8: Number of the excited Rydberg atoms normalized to the saturation value,N_{sat}, as a function of the BEC size, σ_{BEC} for the 53D$_{5/2}$ (red dots) and 78D$_{5/2}$ states (blue squares).

6.3 Coherent excitations of Rydberg atoms in BECs

Recent results in trapping and manipulation of ultracold samples gave us the possibility to coherently control large atomic ensembles. We wanted to check if with the use of our present configuration an observation of the Rabi oscillations between ground and Rydberg state is possible. In this section the observation of coherent excitation to the Rydberg state for different states and densities is presented. Using the setup discussed in chapter 4 and the expansion technique described in section 6.1, a BEC sample was prepared in the same way three times and a number of identical sequences consisting of Rydberg excitation, field ionization and detection were conducted on each sample. The excitation time t_{pulse} or the condensate size σ_{BEC} were varied. The excitation dynamics were investigated by changing the irradiation pulse durations t_{pulse}, between 100 ns and 3 μs. The first step of the two photon transition was blue detuned from the resonance by 500 MHz. The density and the excitation state were varied in order to investigate the coherent behavior of Rydberg atoms.

In figure 6.9 experimental and theoretical excitation dynamics for three different BEC densities are presented. The graph represents a dependence of the number of excited Rydberg atoms, N$_{Rydb}$, on the excitation pulse t_{pulse}. Such slopes for blocked excitations are predicted in [40]. The initial slope, α, can be extracted from the fit of a simple exponential saturation function:

$$N_{Ryd}(t) = N_{sat}\left(1 - e^{\alpha t/N_{sat}}\right), \tag{6.2}$$

where t stands for the excitation time and $N_{Ryd}(t)$ is the number of Rydberg atoms at time t. This function does not reproduce the exact dynamics but can be used for extracting for example the saturation value, N_{sat}, and the rise time of the slope, as in [38].

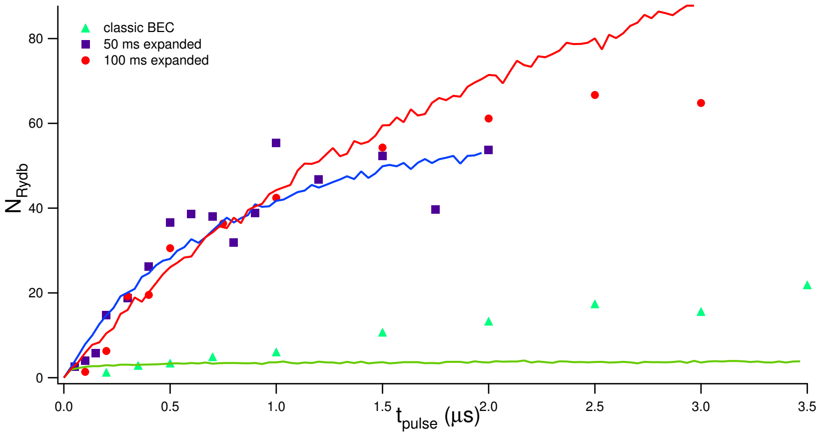

Figure 6.9: Number of the created Rydberg atoms as a function of the irradiation pulse length, t_{pulse} for three density values, the green triangles correspond to the classic BEC with density $\rho \approx 10^{14}$ cm $^{-3}$, the blue squares to 50 ms expansion and $\rho \approx 3\times10^{13}$ cm $^{-3}$, and the red dots to 100 ms expansion and $\rho \approx 1\times10^{13}$ cm $^{-3}$. Theoretical simulations of the excitation for the same density regimes as the one used in experiments are in good agreement with the experimental data and they are represented by lines.

Figure 6.9 shows that with a lower density the Rydberg atom number, N_R, grows more slowly than with the higher density values. This result is consistent with the theory (see equation (2.56)) that states that the collective Rabi frequency $\Omega_{coll} \propto \sqrt{N}$. Using a theoretical simple model representing interactions between the Rydberg atoms including the blockade effect, one can see that denser samples i.e. at 50 ms expansion, reach the saturation value faster than those with lower densities i.e. at 100 ms expansion. The fluctuation of the number of the Rydberg atoms visible in figure 6.9 is a result of the fluctuation of the number of atoms in the blockaded area obtained by integrating the distribution inside each sphere. The final number of the excited Rydberg atoms N_{Rydb} is a sum of contributions from all blocked regions. However, for the 100 ms expansion the discrepancy between theoretical and experimental results is visible. The number of excited Rydberg atoms predicted by theory is higher than the one observe during the measurements due to the saturation of the experimental signal on the CEM[1]. In the case of the non expanded BEC, the experimental curve differs significantly from curves obtained from the expanded BECs. This is due to the fact that we cannot consider the system being in 1D as the width of the non expanded BEC is greater than the radius of the blockade for the 53D$_{5/2}$ state. The almost pure condensate has a

---

[1] We observed that depending on a n state and the experimental sequence the detection saturates when from 40 to 80 ions reach the CEM.

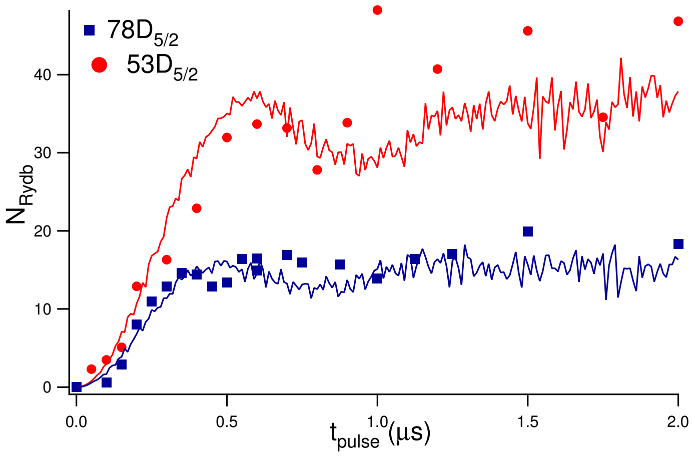

Figure 6.10: Number of excited Rydberg atoms, N_{Rydb}, as a function of the pulse lenght, t_{pulse} for the 53D$_{5/2}$ (red dots) and 78D$_{5/2}$ states (blue squares). Samples were expanded for 50 ms with the width in horizontal direction $\sim$ 160 μm. The experimental data are represented by symbols and their theoretical data by the continuous lines.

Gaussian distribution of atoms. The tail of such a distribution consists of single atoms that are far from the blockade regimes of the atoms in the center of the distribution. The exact contribution of these atoms is not well know and the results are currently under further investigation.

In figure 6.10 the typical excitation dynamics for two different n-states are presented. This experiment was conducted using 53D$_{5/2}$ and 78D$_{5/2}$ states. From the experimental points one can see that the Rabi oscillations that characterize coherent excitation are not very well distinguishable due to the non uniform distribution of atoms in the sample and the thermal tail of the BEC. The thermal fraction gets excited and creates the Rydberg excitations with different collective Rabi frequencies. In this way the excitations presented in the figure 6.10 are the average of excitations with different collective frequency. As a result clear oscillations are washed out. As expected with a higher n state the dipole blockade radius r_b increases and the characteristic initial slope is faster. As the blockade radius for the 53D$_{5/2}$ is half of the radius of the 78D$_{5/2}$ state, the number of blocked regions that fits into the sample volume is twice as big, therefore we observe twice as many detected Rydberg atoms. This is confirmed by a simple theoretical model assuming complete collective Rabi oscillations between the ground and excited state without decoherence over spatial dependence:

$$P_{Rydb} = \sin^2\left(\sqrt{N}\omega t/2\right), \tag{6.3}$$

where N is the number of atoms in the blocked area, ω is the Rabi frequency of the excitation calculated with our experimental parameters. The number of atoms in each sphere is calculated by integrating the distribution inside the sphere. Then by considering a 1D Gaussian distribution the contribution of different blockade sphere was summed. The separation between each sphere is twice the blockade radius. In the model the number of atoms and the width of the distribution for both states were fixed. The Rabi frequency was slightly adjusted due to the imprecise measurement of the waist and powers of both excitation laser. In the case of pure van der Waals interactions the distance between two excited Rydberg atoms is defined as R=$2r_b \propto$ n$^{11/6}$. In the blockade regime, the scaling law for the dependence of the collective Rabi frequency on the condensate volume is $\Omega \propto$V$^{1/2}$. According to theoretical model, and as reported in table 6.1, that Rabi frequency for the 1D configuration should scale as $n^{-7/12}$.

Table 6.1: Scaling laws for the excitation volume and the collective Rabi frequency 1D and 3D systems.

parameter	1D	3D
Volume V	$\propto$ R	$\propto R^3$
collective Rabi frequency Ω	$\propto n^{-7/12}$	$\propto n^{5/4}$

6.4 Probing with BEC

In this section we describe a method of imaging the intensity profile of the excitation lasers. A BEC small compared to the beam size allows us to examine intensity distribution of the laser beams using BEC as a probe. The sample is released from the trap and passes through the laser beams of the excitation radiation. This radiation consists of multiple pulses. The Rydberg atoms are detected while the BEC passes through the beams, see figure 6.11a). In figure 6.11 b) one can see the dependence of the ion count on the distance of the center of the cloud from the trap center. The obtained results for the width of the laser beam (115±12μm) are in very good agreement with the measured values.

6.5 Counting statistics in ultracold Rydberg samples.

In section 6.2 the blockade effect was explained using BEC samples of varying sizes. In this section we will use the Mandel Q factor as an indicator of sub-Poissonian counting distribution in the strongly interacting regimes. We present

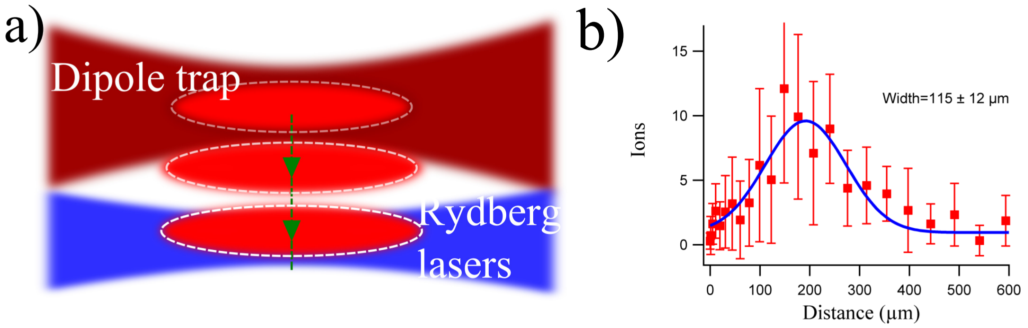

Figure 6.11: (a) Schematic representation of the BEC released from the dipole trap and passing through the excitation radiation. (b) The ion count versus distance (measured relative to an arbitrary reference point) is characterized by a Gaussian distribution.The inferred size of the laser beams is $115{\pm}12\mu$m, to be compared to actual size of 140μ.

results on large samples of ultra cold atoms trapped in magneto-optical traps. The atoms in magneto-optical traps were chosen instead of the Bose condensed samples due to the higher experimental repetition rate. Due to strong interactions that lead to dipole blockade we expected to see clear signature of sub-Poissonian counting statistic with negative values of the Mandel Q-parameter.

6.5.1 The Mandel Q parameter

The Mandel parameter Q describing the deviation from the Poissonian distribution is defined as [54]:

$$Q = \frac{\left\langle N_{Rydb}^2 \right\rangle - \left\langle N_{Rydb} \right\rangle^2}{\left\langle N_{Rydb} \right\rangle} - 1, \tag{6.4}$$

where N_{Rydb} stands for the number of excited Rydberg atoms. In the case of the pure Poissonian distribution, when the events are independent from each other the Q factor is equal to zero because the variance id equal the mean. Values for $Q > 0$ correspond to the super-Poissonian distribution and values $Q < 0$ to the sub-Poissonian one. The minimum $Q = -1$ represents a theoretical case without any fluctuations i.e. a pure or Fock state. In the limit of negligible interactions between atoms in the sample, the dynamics of each atom is independent of the dynamics of any other atom. If one assumes that the excitation laser irradiates the whole sample in a homogeneous way, the probability of excitation for one atom is $P_{exc} = \left\langle N_{Rydb} \right\rangle / \left\langle N_a \right\rangle$, where $\left\langle N_a \right\rangle$ is the number of atoms in the sample. The deviation of counting statistics from the Poissonian distribution is determined by the probability of excitation [50, 49, 4]. If a sample consisting of N atoms is a subject of the excitation to the Rydberg states and each of atoms has 100% probability to be excited, we obtain $Q = -P_{exc} = -1$. If then we consider the same sample but the excitations are blocked due to the dipole blockade effect, the number of excited Rydberg atoms in the whole sample is equal to the number of blockade spheres that fit into the region covered by the atomic ensemble. During one excitation pulse we excite again all possible Rydberg atoms from the system due to the collective effect and the probability is again equal 1 giving Q=-1. In this way the Rydberg excitation blockade is expected to lead to sub-Poissonian counting statistic with negative values of the Mandel Q parameter. To characterize the dipole blockade via counting statistic we need to assume that the number of Rydberg atoms does not fluctuate significantly from one excitation process to another.

6.5.2 Experimental results

In our experiment we have conducted measurements for states with $n > 52$ finding that Mandel parameters indicates strong sub-Poissonian counting statistics. As in [49] for detected number of Rydberg atoms, the detected Mandel parameter will be noted as Q'. Then the detection efficiency, η, has to be taken into account giving as a result $Q'\eta Q$ where Q is the the real value of Mandel parameter. We have obtained $Q' \approx -0.5$ which when considering η on the order of 35% Q' is very close to -1 (when errors of the detection efficiency and Q factor are taken into account). The negative Q' regime is extremely sensitive to the detuning from resonance of the Rydberg excitation, with even a few MHz detuning leading to highly super-Poissonian statistics.

We were interested to observe temporal changes of the sample in the regime where number of Rydberg atoms is saturated. For this reason we determine the Q-factor while performing excitation experiment using different time pulse lengths, see figure 6.12. One can see that the measured value of Q' decreases while the number of excited Rydberg atoms increases and they both reach their saturation point at the same time. This behavior was predicted by Stanojevic et al [68].

Furthermore, we were interested how the Q parameter depends on the detuning of the second transition laser. For this reason we have conducted a frequency scan of the IR laser. This measurement showed how the detuning of the IR laser may affect the reliability of the measurement. In figure 6.13 it is clearly visible that when one is out of resonance with the Rydberg state the value of Q-factor becomes higher. We assume that this is due to jitter of the IR laser in/out of the resonance position but this needs further theoretical investigation. The measurements presented in figure 6.14 for the dependence of confirm that when the laser is out of resonance with the excited state the Q does not reach its minimum value. The curve corresponding to 5 MHz detuning from resonance with the Rydberg

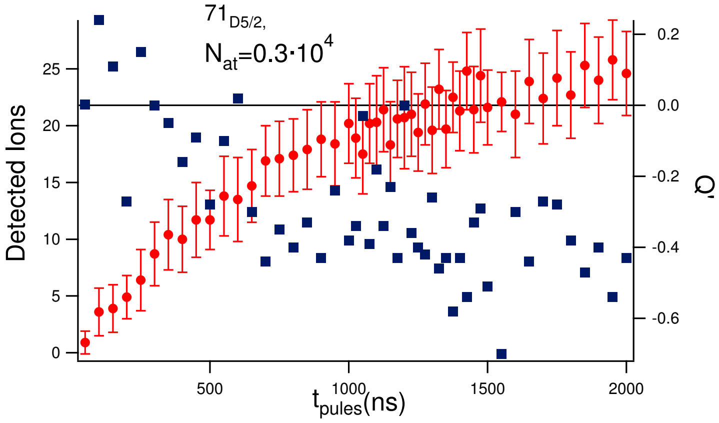

Figure 6.12: Excitation dynamics of the atoms trapped in the MOT. The 0.3×10^4 atoms were excited to the 71 $D_{5/2}$ state. The Q' factor was calculated for every point measured.

state clearly grows and the Q-factor takes positive values. The timescale of the excitations presented in figure 6.14 is longer than the usual excitation timescale due to instability of the excitation laser. Instead curve (fig. 6.12) where the IR laser was put on resonance presents a decrease of the Q-factor value while increasing the pulse duration. The same measurements were conducted using as a sample Bose Einstein condensates. The obtain results are in good agreement with the measurements in a MOT, as negative Q values were observed.

6.6 Conclusions

In this chapter results on excitation of Rydberg atoms from ultracold atomic samples were presented. A new technique for calculating the dipole blockade radius for effective 1D sample was demonstrated. By measuring the number of excited Rydberg atoms in samples characterized by different sizes it is possible to calculate the distance between the excited atoms. These results showed good agreement with theoretical calculations. An attempt to measure collective coherent excitations of Rydberg atoms in Bose Einstein condensate was also made. The obtained results follow the theoretical predictions of the simple model that assumes interactions between excited atoms. However, the collective Rabi oscillations were hard to observe due to the non uniform distribution of atoms in the samples. The evidence for an effective 1D system was presented by both experimental and theoretical results. Furthermore, we measured the counting statistics in the strong blockade regime in ultra-cold clouds. We have found clear signatures of strong interaction between Rydberg atoms that are proved by sub-Poissonian counting

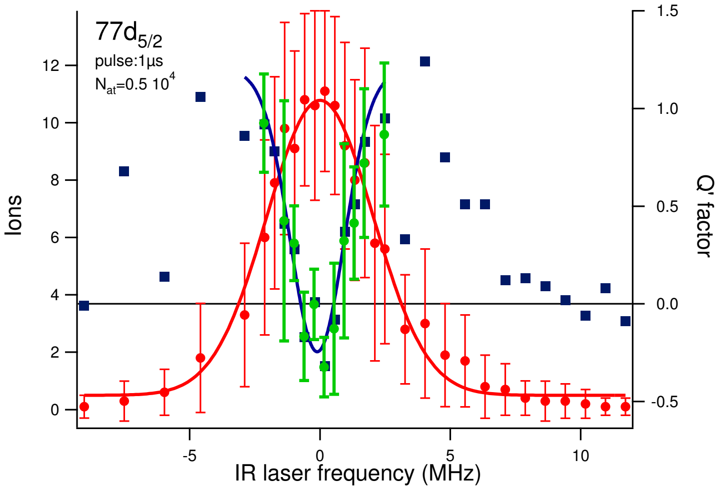

Figure 6.13: Rydberg atoms spectra in a MOT. The Q'-factor measurements (blue squares) against the frequency are shown as well. The blue laser was detuned by 1 GHz from the resonance with the intermediate state. The number of atoms was 0.5$\times$ 10^4 and the intensities were $I_{blue} \approx$ 20 W/cm^2 and $I_{IR} \approx$ 380 W/cm^2, respectively. The time of the pulse lenght was 2 μs.

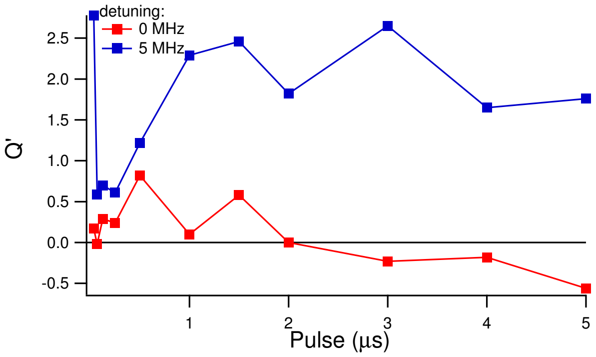

Figure 6.14: The Rydberg excitation dynamics in a MOT. Atoms were irradiated with blue and IR lasers with intensities $I_{blue} \approx$ 8 W/cm^2 and $I_{IR} \approx$ 380 W/cm^2, respectively. The red squares represent the case with the IR laser frequency put on resonance and the blue one with the IR laser frequency detuned 5 MHz from resonance.

statistics with Mandel Q-parameters around -0.5.

Chapter 7

Rydberg atoms in optical lattices

In recent years quantum information science was subject of intense studies [6, 12, 42]. The main goal for these theoretical and experimental efforts is to create quantum computers. To achieve this goal one needs to be able to implement quantum protocols that consist of a sequence of quantum gates which are basic quantum circuits. A quantum gate operates on a small number of interacting qubits. An experimental realization of a quantum bit is itself an arrangement of entangled atoms. It is important to think about implementing quantum protocols. Rydberg atoms were proposed to be a great subject for quantum information research as they are characterized by a large polarizability so they exhibit long range interactions. These interactions leading to dipole blockade effect make them a suitable candidate for realization of controllable quantum systems [44]. However, experimental implementation of quantum gates is a challenging task requiring coherent manipulation of a large number of coupled states and so future applications require the large number of Rydberg excitations in a spatially ordered array. This can be provided by placing atoms in periodical potentials. Several theoretical attempts to create two qubits gates encompassing these two fields were already made [42]. For example one of the discussed concepts uses atoms in optical lattices and controllable state dependent two body interactions. Coherent cold collisions of atoms, optical dipole-dipole interactions [12, 43], or the two qubit gates based on the large permanent dipole interactions between Rydberg atoms in static electric fields [44] may be example of such two body interactions.

In this chapter experiments with Rydberg atoms in the one dimensional optical lattice are presented. In the first section the non destructive character of Rydberg atoms excitation in optical lattices is shown. During an excitation process from a sample containing 50 thousand atoms only few reach the Rydberg state. It will be shown that this quantity is to small too perturb significantly the phase coherence of a Bose Einstein condensate. Subsequently results on coherent excitation of Rydberg atoms trapped in periodic potentials are demonstrated. According to the super-atom picture the collective Rabi frequency for a single-site excitation scales with $\sqrt{N}$, where N is the number of atoms in the blocked area. We demonstrate that the system consisting of tens of interacting Rydberg atoms trapped by periodic optical potential follows this scaling law. We also prove that well-defined length of the sample with sharp boundaries reduces the effect of non uniform distribution of atoms in the sample that is responsible for different collective local Rabi frequencies. As a result we can observe collective Rabi oscillations in contrast to the results presented in chapter 6.

7.1 Non destructive character of Rydberg excitations

In the case of the Rydberg atoms excited from a Bose Einstein condensate sample one may expect that atoms that underwent the transition to high energy states would destroy the phase coherence of the BEC. In this section we present results on the effect of Rydberg atoms on the phase coherence of the condensate. We performed measurements to check if the BEC after being a subject of excitation to high n quantum states maintains its coherent properties. An optical lattice is a useful tool to investigate phase properties of a Bose Einstein condensate. There are two methods to extract information from the BEC: to look at the condensate in situ or after time of flight. By looking at the BECs released form the lattice after several milliseconds of time of flight one observes its momentum distribution. As a result one can study the interference pattern of the atoms released from the lattice. For shallow potentials one can examine such parameters as the lattice depth, interference pattern profile or visibility.

Experiments presented in this section were performed in the configuration where the lattice beams were couterpropagating with a lattice spacing was on the order of half a micron. Clear interference pattern after free expansion of more than 20 ms of time of flight were observed.

- **Interference pattern profile**

  The sample was loaded adiabatically into the optical lattice which was then abruptly switched off. After 23.6 ms of time of flight, atoms were imaged via absorption imaging. Three different measurements were performed. First we imaged the atoms released from the lattice without applying any excitation radiation, see figure 7.1 a). Then to see the effect of the blue laser radiation on the atoms we irradiated the condensate in the lattice using 421 nm laser radiation, see figure 7.1b). Subsequently, we performed two step excitation using both excitation lasers (421 nm and 1020 nm) on the sample prepared in the same way as in two previous cases, see figure 7.1c).

The first step of this excitation pulse was 1 GHz blue detuned from the intermediate state and 75 shots of 1 μs were sent to the sample. By comparing these three figures it is possible to observe a clear effect on the interference pattern, when the excitations are on. An effect of the blue laser on the number of atoms is visible when one compares figures 7.1 b) with 7.1 a) but an even stronger effect can be seen by looking at fig. 7.1 c). In figure 7.1d) one can see the distribution profile of the three measurements. Although there is some decrease of the central and side peaks populations when the blue and blue + Ir radiation is applied, the overall interference pattern with all peaks is still visible.

- **Visibility measurements**

  One method of quantifying the degree of coherence between the lattice sides is to define a visibility of the interference pattern. To obtain a pattern that allows us to measure the visibility, one has to accelerate to the Brillouin zone edge the BEC loaded into an optical lattice [24]. The visibility is then calculated from the relative height of the side peaks compared to the minimal high. The side peaks correspond to the momentum classes $\pm 2\hbar k_L$, where is the wavewector $k_L = 2\pi/\lambda$. A sample interference pattern is presented in figure 7.2 where the horizontal axis of this figure has been rescaled in units of the recoil momentum. In this way it reflects momentum of the condensate before releasing it from the optical lattice.

  This interference pattern can become less distinct if one assumes that there is a random phase different between neighboring sites. The effect can vary from a slight peak broadening to the pattern becoming completely washed out. The measurements of the visibility were used to quantify this effect. The visibility is defined as the normalized difference between the maxima h_{max} and minima h_{min} of an interference pattern, see figure 7.2 [59]:

  $$V = \frac{h_{max} - h_{min}}{h_{max} + h_{min}}. \tag{7.1}$$

  Our measurements showed that it is possible to observe some decrease of the visibility of the interference pattern that for the irradiated samples is on the order of 45% and for samples without Rydberg excitation applied on the order of 65%. However, the side peaks are still very well defined and the error of the measurement is large. We can make a statement that by exciting Rydberg atoms in an optical lattice we observe almost no effect on the condensate visibility so far. Therefore, excitation to high n states can be done avoiding the BEC phase perturbation.

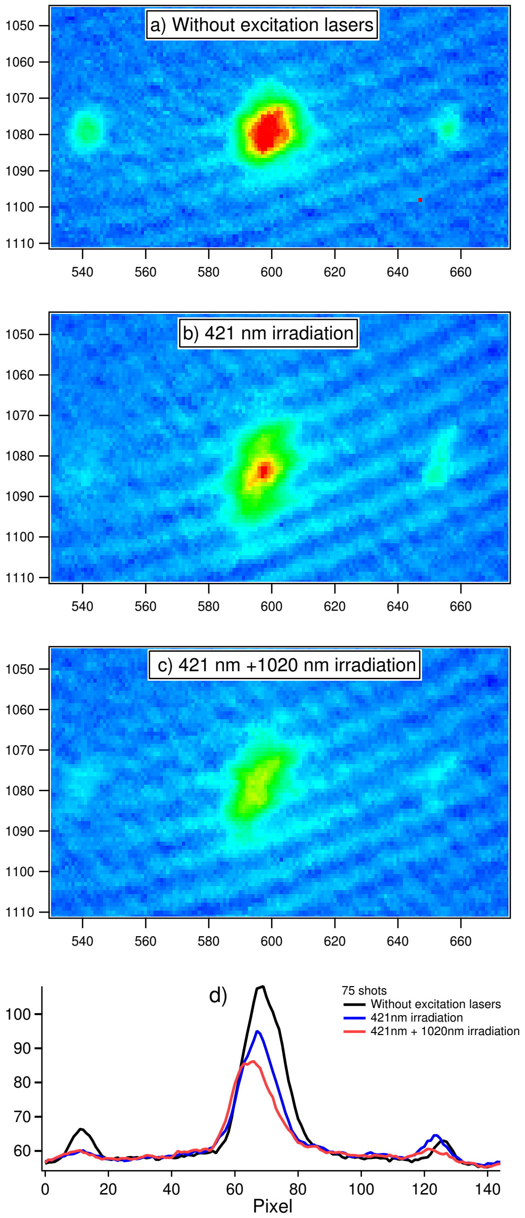

Figure 7.1: Interference patterns of the Bose Einstein condensate released from the optical lattice with d_L half a micron. Images are taken after ∼23 ms time of flight. (a) No excitation lasers are present, (b) 75 shots of the 421 nm laser radiation were applied, (c) both excitation lasers were used to create Rydberg atoms, 75 shots were applied to excite the sample. (d) A profile of interference patterns of the condensate released from an optical lattice. One can observe that the first order peaks are slightly less visible in the case with the excitation radiation.

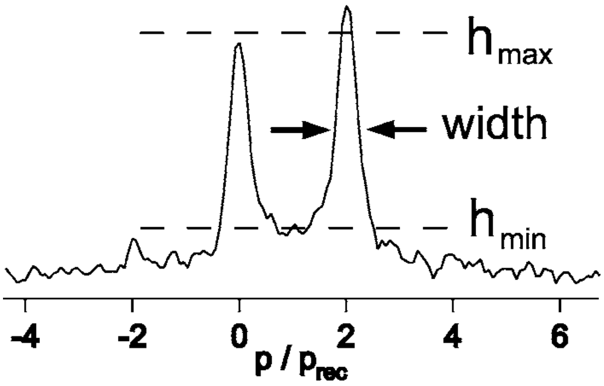

Figure 7.2: Calculation of the visibility. An absorption image integrated perpendicular to the lattice direction, where the h_{max} is the maximum and h_{min} the minimum of the interference pattern [59].

Summarizing, exciting Rydberg atoms in an optical lattice shows no effect on condensate phase. A typical BEC contains 50 thousand atoms of which only around 40 get excited. This quantity of Rydberg atoms does not perturb the phase coherence of the condensate. Also the interference pattern of a condensate released from stationary lattice remains well defined although some effect of the blue laser alone and both excitation lasers is visible. Therefore, more than 10 excitation sequences can be applied on the same condensate without a considerable change of phase coherence or atom number in the condensate.

7.2 Coherent excitations

We expected that by implementing optical potential to our system we will have an enhancement of the possibility of seeing collective oscillations as in each lattice well the profile of the atoms is more defined. The results presented in chapter 6 showed that Rydberg atoms get collectively excited. Nevertheless, an observation of complete Rabi oscillations was impossible because of the Gaussian profile of the atomic distribution in the sample and the fluctuation in density for each excitation volume. The enhancement of the oscillations is visible in figure 7.3 where Rydberg excitations as a function of pulse duration is presented for configuration with (blue dots) and without (red squares) implementing of optical potentials. In our configuration the collective Rabi frequency is expected to be $\sim$ 200 kHz and this value corresponds to experimental result visible in figure 7.3.

To maximize the number of collective excitations we set the lattice spacing used in the experiment above at $d = 2.2$ μm. This value is different from the one used in the experiments presented in previous section where $d = 0.5$ μm which

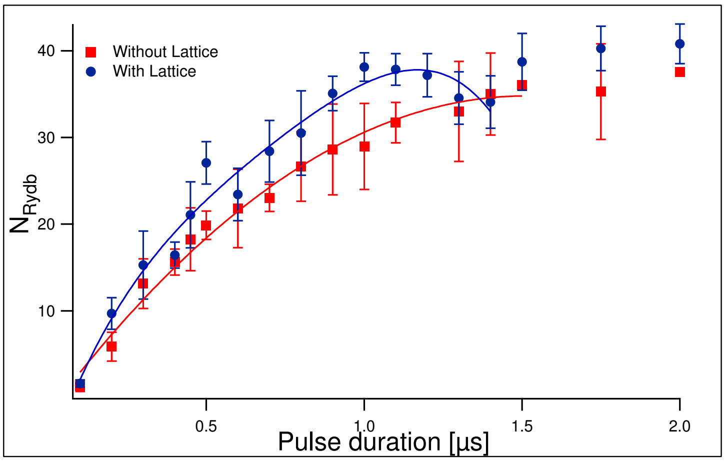

Figure 7.3: The excitation dynamics of the Bose Einstein condensate expanded for 50 ms in the horizontal arm of the dipolar trap. The intensities of the excitation lasers were $I_{blue} \approx 40$ W/cm^2 and $I_{IR} \approx 380$ W/cm^2 for the 421 nm and 1021 nm radiation respectively. The first step of the transition was blue detuned by 1 GHz from resonance with the 6P$_{3/2}$ state. Red squares correspond to the excitation dynamics of the atoms held only by the dipole trap, instead blue dots correspond to the atoms excited in the optical lattice. One can see that for the same parameters the oscillations are visible only in the case of excitations of atoms inside an optical lattice.

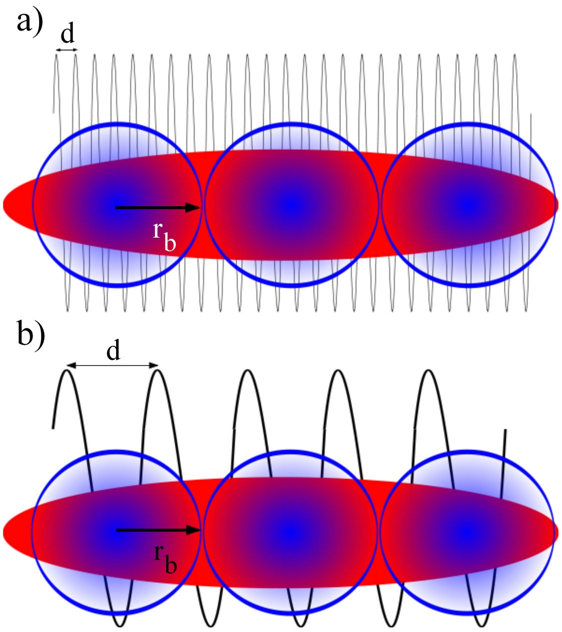

Figure 7.4: For a Bose Einstein condensate loaded into an optical lattice, the red spheres represent a region blocked by a Rydberg atom. (a) The lattice spacing is small compared to the radius of the blockade, $d << r_b$. (b) The lattice spacing is comparable with the radius of the blockade, $d \approx r_b$.

according to the formula 4.1 is achieved by two counterpropagating beams. In this chapter we will be using mainly the 53 $D_{5/2}$ state whose blockade radius, r_b, is around ~6 μm as it was estimated previously. Therefore in the case of counterpropagating beams the obtained d value is around ten times smaller than the dipole blockade radius; every tenth lattice site contains at most one collective Rydberg excitation. In our case, we aimed for a lattice spacing comparable with the radius blockade r_b to enhance the probability of single excitation per site, see figure 7.4. One can obtain the larger lattice spacing by changing the angle between the two beams creating the optical lattice. Therefore, putting two beams with an angle of $\Theta \sim 18°$ between them, give a maximal achievable in our setup lattice spacing of $d = 2.6$ μm. The experiments presented in the further part of this chapter are conducted in this configuration.

To enhance the visibility of the oscillation effect we use a special loading procedure to clean the atomic distribution, schematized in figure 7.5. The general idea of loading a Bose Einstein condensate into an optical lattice is briefly presented in chapter 4. In this section presented technique is improved in order to "cut" the edges of the Gaussian distribution of the sample, see figure 7.6.

- The condensate expands inside one dipole trap beam (This procedure is

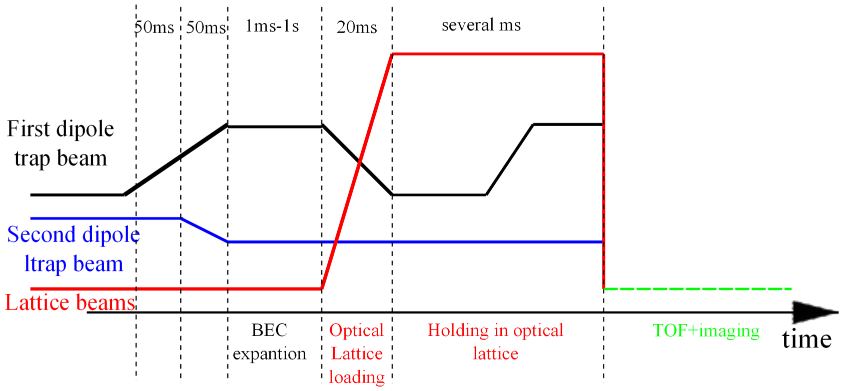

Figure 7.5: Time sequence of the experiment. Firstly, the atoms are loaded into one arm of the dipole trap where they expand. Then, the dipole trap beam is ramped down while the lattice beam is ramped up (2 ms). After increasing back the power of the dipole trap laser, the atoms trapped in the region of overlap of these two laser beams are subject to excitation pulses. Finally, the atoms are released and after few ms of time of flight an absorption image is taken.

already presented in previous chapter).

- The lattice beams are ramped up in 2 ms
- Simultaneously the power of the dipole trap laser is ramped down and the atoms outside the lattice region are lost from the trap. The value of the dipole laser is chosen to be low enough to lose the atoms from outside the lattice region. The overlap region of these two beams is defined by the lattice beam diameter and gives combined radial trap depth high enough to hold the atoms.
- At the end dipole trap power is ramped back and gives the maximal radial confinement of the atoms.

In this way we avoid having a large number of atoms outside the finite lattice region. In this way the condensate occupies a region of defined horizontal length and it gives us a possibility to evaluate precisely how many lattice sties are filled by atoms using equation (4.1) for the lattice spatial period. At the end the Rydberg excitations pulses are applied and both lattice and dipole beams are switched off. The atoms are allowed to fall for a few ms and then an absorption image is taken, see figure 7.5. In the meantime excited atoms are subject to electric field that ionizes and pushes them toward the channeltron where they are detected.

The usefulness of the cleaning technique can be explained with the use of a simple model that assumes the dipole blockade of Rydberg excitations with atoms

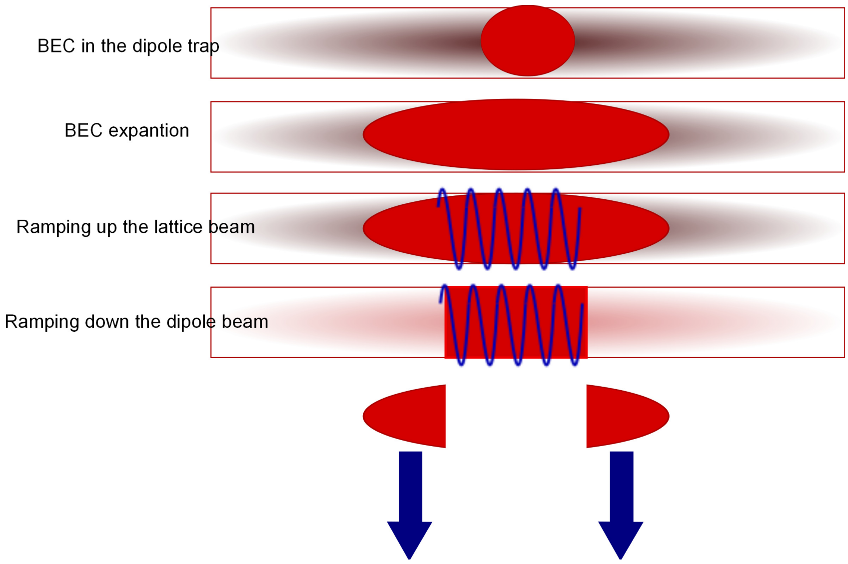

Figure 7.6: “Cleaning procedure”. Loaded into one arm of dipole trap laser, the atoms are expanded. Then by introducing the optical lattice laser they are confined in a region defined by the lattice beam diameter. When the dipole trap beam is ramped down the atoms outside the region of the overlap are lost from the trap.

divided by the small regions corresponding to the lattice spacing. In figure 7.7 one can see the Gaussian distribution of atoms, the blue line and the already cleaned distribution as a red line. An influence of these distributions on the theoretical results of the Rabi oscillations is clearly shown. The curve measured by using a condensate with the cleaned distribution should be characterized by deeper and more visible oscillations.

The frequency of coherent excitations of the Rydberg atoms is proportional to $\sqrt{N}$, where N is the number of atoms in the blockade sphere. Loaded into the lattice, a condensate was subject to the cleaning procedure cutting off the edges of the original BEC. In figure 7.8 the experimental results of the excitation dynamics for two different BEC densities are presented along with the results obtained from the theoretical model used in chapter 6. The expansion of the condensates was chosen to be 15 ms, 500 ms and 1 s. The difference in number of atoms in the blocked region is of a factor of 4 for the 15 ms and 500 ms expansions and 20 for the 15 ms and 1 s expansions. After rescaling with $\sqrt{N}$, the timescales of the collective excitations are the same and the oscillations happen for the three densities for the same time. A simple numerical model containing a gaussian distribution of on-site Rabi frequencies and a small dephasing rate between the lattice sites, chosen such as to reproduce the observed long-term increase in the number of collective excitations, agrees well with our experimental observations. This model is

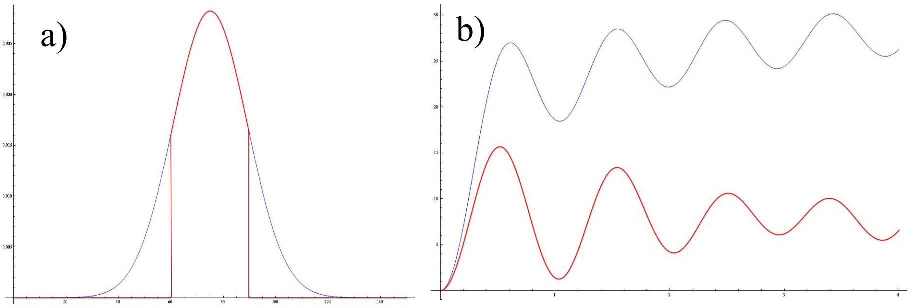

Figure 7.7: Simple simulation of the "cleaning" effect of the atom distribution. (a) On the left hand side the blue line represent Gaussian distribution of atoms loaded into an optical lattice and the red line already "cleaned" atoms distribution. (b) On the right hand side one can see that in the case of the Gaussian distribution the oscillations are weaker and not so pronounced as in the case of the "clean" distribution.

an extension of the model used to analyze results presented in chapter 6. In this case the separation between each blocked region is a fixed value corresponding to the closes multiple of lattice site that is comparable with the blockade radius. A visible in figure 7.8 increase of the signal is simulated by adding an atom number dependent dephasing :

$$P_{Rydb} = \sin^2\left(\sqrt{N}\omega t/2 + A\sqrt{N_{tot}}t\right), \tag{7.2}$$

where A is a coefficient, determined by a fit to one set of data and N_{tot} is the total number of atoms in the cloud.

7.3 Conclusions

In this chapter results on phase coherence of the Bose Einstein condensate during the Rydberg excitations were presented. Both the interference pattern of the BEC released from the static lattice and the visibility measured after releasing atoms from accelerated potential shows non destructive character of the Rydberg excitations on a phase of the condensate. In the second part of the chapter measurements of the collective excitations were shown. Using a new procedure to load atoms into a lattice we obtained well defined distribution of atoms is the sample. The importance of this procedure was then proved by a simple theoretical model. To conclude, the measurements provide evidence for coherent and collective Rydberg excitation dynamics of BECs loaded into optical potentials. The observed coherent collective excitations in different densities show the predicted scaling of the number of atoms in the blockaded region.

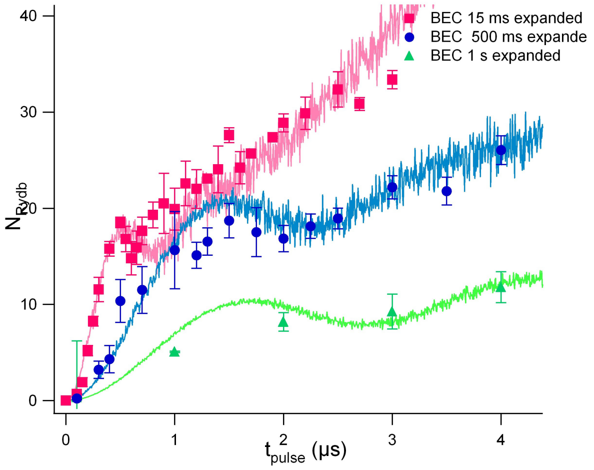

Figure 7.8: The excitation dynamics of the Bose Einstein condensate loaded into an optical lattice. Atoms were subject to the cleaning procedure and excited by 421 nm laser blue detuned by 1 GHz from the resonance with the $6P_{3/2}$ state with intensity $I_{blue} \approx 40$ mW/cm^2 and 1021 nm laser with intensity of $I_{IR} \approx 380$ mW/cm^2, condensates expanded by 15 ms are represented by red squares, the samples expanded by 500 ms by the blue dots and the one expanded by 1 s by green triangles. The continuous lines represent the results obtained from the simple numerical model.

Chapter 8

Summary and Outlook

The strong interactions of Rydberg atoms and their implications have been the unifying subject of this thesis. The fundamental phenomenon arising from these interactions, the dipole blockade was then predicted to be a useful concept for quantum information purposes, therefore experiments measuring the dipole blockade radius and describing the characteristic of the interactions were presented. Furthermore, as the quantum information requires also to coherently excited atoms and the ability to control interactions between them, it was proposed to load ultracold atoms into periodic potential. The results on the influence of the excitation on the phase coherence of a Bose Einstein condensate and on the coherent collective excitations were then shown in the following part of the thesis. The results of these experiments are summarized in the following.

In chapter 5 a series of experiments was presented. Their goal was to define experimental quantities and to show how future experiments can be affected both mechanically and on the level of internal energies. First the experiments in the magneto optical traps were performed. They gave us the knowledge about the detection efficiency of the system that was measured to be around 35%. Furthermore, by experimentally producing the Stark map and comparing it with the calculated values we have obtained an approximate value of the residual field in the glass cell around $\approx$ 10mV/cm. It was also proven that we have very good control upon the applied external field. As further results we have showed that due to emission from the excited level atoms experience a recoil. Some experiments using atoms in the Bose Einstein phase were performed as well. We have introduces the ionization spectra produced from a BEC. Then, we obtained some results on the Rydberg atom excitation such as the half line width of the Rydberg atom spectra (TBD). In the last part of this chapter the Rydberg excitation of ultracold atoms inside optical lattices has been shown. No heating effect due to the lattice lasers was observed on the Rydberg spectra.

Chapter 6 shows results on excitation of the Rydberg atoms from ultracold atomic ensembles. In this chapter we proposed a new method of measuring the dipole blockade radius r_b in an effective 1D system. This quantity can be extracted form the linear grow of the number of Rydberg atoms produced as a function of the size of the Bose Einstein condensate. These results are in very good agreement with the theoretical calculations. Furthermore, we presented the evidence for the effective one dimensional system. Moreover, we showed that the collective Rabi oscillations are hard to observe due to non uniform distribution of atoms in the sample. Finally, the counting statistic in the strong blockade regime in ultracold atomic cloud was presented. We demonstrated clear signatures of the strong interactions between the Rydberg atoms that were proved by sub-Poissonian counting statistic with measured Mandel Q'-parameter around $-0,5$ which results in -1 taking into account the efficiency of detection.

The results presented in chapter 7 shows that the Bose Einstein condensate remains phase coherent during the Rydberg excitation. This was proven by both looking at the interference pattern of the BEC released form the static lattice and the visibility measured after releasing atoms from accelerated potential. Furthermore, by using the new loading procedure that purify the atomic distribution we observed the coherent collective Rydberg excitation dynamics of BECs loaded into optical potentials. Moreover, I showed that collective coherent excitations for the different sizes of the sample follow predicted scaling of the number of atoms in the blockaded region.

The results presented in this thesis represent extensive studies on the Rydberg excitations in the magneto-optical traps and Bose Einstein condensates. The shown results on measuring the dipole blockade radius, exciting atoms loaded into optical potential into high energy levels and coherent collective excitations bring us closer to the main goal of the research on the Rydberg atoms which are the implementation of quantum protocols.

Chapter 9

Publications

Publications:

1. *Time-Resolved Measurement of Landau-Zener Tunneling in Periodic Potentials* A. ZENESINI, H. LIGNIER, G. TAYEBIRAD, J. RADOGOSTOWICZ, D. CIAMPINI, R. MANNELLA, S. WIMBERGER, O. MORSCH, AND E. ARIMONDO, Selected for the September 2009 issue of Virtual Journal of Atomic Quantum Fluids, Vol. 1, Issue 3 September 2009. [76]
2. *Ion detection in the photoionization of a Rb Bose-Einstein condensate* M. VITEAU, J. RADOGOSTOWICZ, A. CHOTIA; M.G. BASON, N: MALOSSI, F. FUSO , D. CIAMPINI, I. I. RYABTSEV, O. MORSCH, AND E. ARIMONDO, [74]

Conferences:

- **Young EMALI Research Meeting**, 22-24 May 2008,Vienna, Austria
  Poster: *Asymmetric Landau-Zener tunnelling and non-exponential decay in a periodic potential*
- **ICAP 2008**, 27 July-01August 2008, Storrs CN, USA

  Poster:*Asymmetric Landau-Zener tunnelling and non-exponential decay in a periodic potential*
- **EMALI Mini school *Control and engineering concepts plus experimental techniques: specific tools*** ,7-12 September 2008, Copenhagen, Denmark,
- **Second EMALI Annual Meeting**, 14-16 September 2008, Copenhagen, Denmark,
  Poster: *Asymmetric Landau-Zener tunnelling and non-exponential decay in a periodic potential*

- **EGAS (European Group on Atomic Systems)**, 8-11 July 2009, Gdansk, Poland,
  Poster: *Ultracold Rydberg atoms in optical lattices*
- **International Workshop - Bloch Oscillations and Landau-Zener Tunneling**, Max-Planck-Institut fúr Physik komplexer Systeme, Dresden, Germany, May 04 - 08, 2009, Dresden, Germany
  Poster: *Landau-Zener tunnelling revisited: asymmetric tunnelling and time-resolved measurements*
- **Young Researchers Meeting**, 22-24 March 2009, Oxford, UK,
- **Mid-term Meeting**, 23 March 2009, Oxford, UK,
  Oral presentation *ESR talk: Landau Zener Tunnelling and Photoionization experiments)*
- **ICAP 2010**, 25 July-01 August 2010, Cairns, Australia
  Poster: *Dipole blockade and counting statistics in ultra-cold and Bose condensed Rydberg samples*

Bibliography

[1] M. Anderlini, E. Courtade, D. Ciampini, J. Müller, O. Morsch, and E. Arimondo, *Two-photon ionization of cold rubidium atoms*, J. Opt. Soc. Am. B, 21 (2004), pp. 840–845.

[2] M. Anderson, J. Ensher, M. Matthews, C. Wieman, and E. Cornell, *Observation of Bose-Einstein condensation in a dilute atomic vapor*, Science, 269 (1995), p. 198.

[3] S. Andreev, V. Balykin, V. Letokhov, and V. V. Minogin, *Radiative slowing and reduction of the energy spread of a beam of sodium atoms to 1.5 k in an oppositely directed laser beam*, JETP Lett., 34 (1981), p. 442.

[4] C. Ates, T. Pohl, T. Pattard, and J. Rost, *Strong interaction effects on the atom counting statistics of ultracold Rydberg gases*, J. Phys. B: At. Mol. Opt. Phys., 39 (2006), pp. L233–L239.

[5] S. H. Autler and C. H. Townes, *Stark effect in rapidly varying fields*, Phys. Rev., 100 (1955), pp. 703–722.

[6] C. Bennett, F. Bessette, G. Brassard, L. Salvail, and J. Smolin, *Quantum computation*, J. Crypt., 5 (1992), pp. 3–28.

[7] K. M. Birnbaum, A. Boca, R. Miller, A. D. Boozer, T. E. Northup, and H. Kimble, *Photon blockade in an optical cavity with one trapped atom*, Nature, 436 (2005), p. 4.

[8] I. Bloch, *Ultracold quantum gases in optical lattices*, Nature Phys., 1 (2005), pp. 23 – 30.

[9] M. Born and V. Fock, *Beweis des Adiabatensatzes*, Z. Phys., 51 (1928), p. 165.

[10] S. Bose, *Planck's law and the hypothesis of light quanta*, Z. Phys., 26 (1924), p. 178.

[11] C. C. BRADLEY, C. A. SACKETT, J. J. TOLLETT, AND R. G. HULET, *Evidence of Bose-Einstein condensation in an atomic gas with attractive interactions*, Phys. Rev. Lett., 75 (1995), p. 11687.

[12] G. K. BRENNEN, C. M. CAVES, P. S. JESSEN, AND I. H. DEUTSCH, *Quantum logic gates in optical lattices*, Phys. Rev. Lett., 82 (1999), pp. 1060–1063.

[13] G. K. BRENNEN, I. H. DEUTSCH, AND P. S. JESSEN, *Entangling dipole-dipole interactions for quantum logic with neutral atoms*, Phys. Rev. A, 61 (2000), p. 062309.

[14] E. BRION, L. H. PEDERSEN, AND K. MOLMER, *Adiabatic elimination in a Lambda system*, J. Phys. A: Math. and Theor., 40 (2007), p. 1033.

[15] V. BUŽEK, R. DERKA, AND S. MASSAR, *Optimal quantum clocks*, Phys. Rev. Lett., 82 (1999), pp. 2207–2210.

[16] T. J. CARROLL, K. CLARINGBOULD, A. GOODSELL, M. J. LIM, AND M. W. NOEL, *Angular dependence of the dipole-dipole interaction in a nearly one-dimensional sample of Rydberg atoms*, Phys. Rev. Lett., 93 (2004), p. 153001.

[17] A. CHOTIA, M. VITEAU, T. VOGT, D. COMPARAT, AND P. PILLET, *Kinetic monte carlo modeling of dipole blockade in Rydberg excitation experiment*, NJP, 10 (2008), p. 045031.

[18] S. CHU, L. HOLLBERG, J. BJORKHOLM, A. CABLE, AND A. ASHKIN, *Three-dimensional viscous confinement and cooling of atoms by resonance radiation pressure*, Phys. Rev. Lett., 55 (1985), p. 48.

[19] D. CIAMPINI, *Realization of a ^{87}Rb Bose-Einstein Condensate: Atomic Physics with Coherent Matter Waves*, PhD thesis, Dipartimento di Fisica E. Fermi, Universita' degli Studi di Pisa, Italy, 2002.

[20] D. CIAMPINI, M. ANDERLINI, J. MÜLLER, F. FUSO, O. MORSCH, J. THOMSEN, AND E. ARIMONDO, *Photoionization of ultracold and Bose-Einstein condensed Rb atoms*, Phys. Rev. A, 66 (2002), pp. 043409–043409–8.

[21] C. COHEN-TANNOUDJI, J. DUPONT-ROC, AND G. GRYNBERG, *Atom-photon interactions*, John Wiley and Sons, 1992.

[22] D. COMPARAT AND P. PILLET, *Dipole blockade in a cold Rydberg atomic sample [Invited]*, J. Opt. Soc. Am. B, 27 (2010), pp. A208–A232.

[23] E. COURTADE, M. ANDERLINI, D. CIAMPINI, J. MÜLLER, O. MORSCH, E. ARIMONDO, M. AYMAR, AND E. ROBINSON, *Two-photon ionization of cold rubidium atoms with a near resonant intermediate states*, J. Phys. B-At. Mol. Opt. Phys., 37 (2004), pp. 967–979.

[24] M. CRISTIANI, O. MORSCH, J. H. MÜLLER, D. CIAMPINI, AND E. ARIMONDO, *Experimental properties of Bose-Einstein condensates in one-dimensional optical lattices: Bloch oscillations, Landau-Zener tunneling, and mean-field effects*, Phys. Rev. A, 65 (2002), p. 063612.

[25] F. DALFOVO, S. GIORGINI, L. PITAEVSKII, AND S. STRINGARI, *Theory of Bose-Einstein condensation in trapped gases*, Rev. Mod. Phys., 71 (1999), p. 463.

[26] K. DAVIS, M. MEWES, M. ANDREWS, N. VAN DRUTEN, S. DURFEE, D. KURN, AND W. KETTERLE, *Bose-Einstein condensation in a gas of sodium atoms*, Phys. Rev. Lett., 75 (1995), p. 3969.

[27] R. H. DICKE, *Coherence in spontaneous radiation processes*, Phys Rev., 93 (1954), p. 99.

[28] T. DINNEEN, K. WALLACE, C. D. TAN, AND P. GOULD, *Use of trapped atoms to measure absolute photoionization cross sections*, Opt. Lett., 17 (1992), pp. 1706–1708.

[29] B. P. DIVINCENZO, *Quantum computation*, Science, 270 (1995), pp. 255 – 261.

[30] A. EINSTEIN, *Quantentheorie des einatomigen idealen gases, 1.*, Sitzber. Preuss. Akad. Wiss. Bereicht, (1924), pp. 261–267.

[31] ——, *Quantentheorie des einatomigen idealen gases 2.*, Sitzber. Preuss. Akad. Wiss. Bericht, (1925), pp. 3–14.

[32] T. A. FULTON AND G. J. DOLAN, *Observation of single-electron charging effects in small tunnel junctions*, Phys. Rev. Lett., 59 (1987), pp. 109–112.

[33] A. GAËTAN, Y. MIROSHNYCHENKO, T. WILK, A. CHOTIA, M. VITEAU, D. COMPARAT, P. PILLET, A. BROWAEYS, AND P. GRANGIER, *Observation of collective excitation of two individual atoms in the Rydberg blockade regime*, Nature Phys., 5 (2009), pp. 115 – 118.

[34] T. F. GALLAGHER, *Rydberg Atoms*, Cambridge University Press, 1994.

[35] A. GRABOWSKI, A. R. HEIDEMANN, A. R. LÖW, A. STUHLER, AND A. T. PFAU, *High resolution rydberg spectroscopy of ultracold rubidium atoms*, Fortschr. Phys., 54 (2006), pp. 765–775.

[36] R. GRIMM, M. WEIDEMÜLLER, AND Y. B. OVCHINNIKOV, *Optical dipole traps for neutral atoms*, Adv. At. Mol. Opt. Phys., 42 (2000), pp. 95–170.

[37] T. HÄNSCH AND A. SCHAWLOW, *Cooling of gases by laser radiation*, Optics Commun., 13 (1975), p. 68.

[38] R. HEIDEMANN, *Rydberg excitation of Bose-Einstein condensates: Coherent Collective Dynamics*, PhD thesis, Physikalisches Institut der Universität Stuttgart, 2008.

[39] R. HEIDEMANN, U. RAITZSCH, V. BENDKOWSKY, B. BUTSCHER, R. LÖW, L. SANTOS, AND T. PFAU, *Evidence for coherent collective Rydberg excitation in the strong blockade regime*, Phys. Rev. Lett., 99 (2007), p. 163601.

[40] J. HONER, H. WEIMER, T. PFAU, AND H. BÜCHLER, *Collective many-body interaction in Rydberg dressed atoms*, arXiv:1004.2499v1, (2010).

[41] K. HUANG, *Statistical Mechanics*, John Wiley & Sons, third ed., 1966.

[42] D. JAKSCH, *Optical lattices, ultracold atoms and quantum information processing*, Contemp. Phys., 45 (2004), pp. 367–381.

[43] D. JAKSCH, H.-J. BRIEGEL, J. I. CIRAC, C. W. GARDINER, AND P. ZOLLER, *Entanglement of atoms via cold controlled collisions*, Phys. Rev. Lett., 82 (1999), pp. 1975–1978.

[44] D. JAKSCH, J. I. CIRAC, P. ZOLLER, S. L. ROLSTON, R. CÔTÉ, AND M. D. LUKIN, *Fast quantum gates for neutral atoms*, Phys. Rev. Lett., 85 (2000), pp. 2208–2211.

[45] T. A. JOHNSON, E. URBAN, T. HENAGE, L. ISENHOWER, D. D. YAVUZ, T. G. WALKER, AND M. SAFFMAN, *Rabi oscillations between ground and rydberg states with dipole-dipole atomic interactions*, Phys. Rev. Lett., 100 (2008), p. 113003.

[46] C. KITTEL, *Introduction to solid state physics*, John Wiley & Sons, seventh ed., 1996.

[47] P. LAMBROPOULOS, *Theory of multiphoton ionization: Near-resonance effects in two-photon ionization*, Phys. Rev. A, 9 (1974), pp. 1992–2013.

[48] P. Lett, R. Watts, C. Westbrook, W. Phillips, P. Gould, and H. Metcalf, *Observation of atoms laser cooled below the Doppler limit*, Phys. Rev. Lett., 61 (1988), p. 169.

[49] T. C. Liebisch, A. Reinhard, P. R. Berman, and G. Raithel, *Atom counting statistics in ensembles of interacting Rydberg atoms*, Phys. Rev. Lett., 95 (2005), p. 253002.

[50] ——, *Erratum: Atom counting statistics in ensembles of interacting Rydberg atoms [Phys. Rev. Lett. 95, 253002 (2005)]*, Phys. Rev. Lett., 98 (2007), p. 109903.

[51] M. D. Lukin, M. Fleischhauer, R. Cote, L. M. Duan, D. Jaksch, J. I. Cirac, and P. Zoller, *Dipole blockade and quantum information processing in mesoscopic atomic ensembles*, Phys. Rev. Lett., 87 (2001), p. 037901.

[52] B. m. Olmos Sanchéz, *Information measures of quantum systems. Collective Rydberg excitations of an atomic gas confined in a ring lattice*, PhD thesis, Departamento de Física Atómica, Molecular y Nuclear, Universidad de Granada, Spain, 2010.

[53] M. G. Makris and P. Lambropoulos., *Reexamination of multiphoton ionization of xenon under 12.7-eV radiation.*, Phys. Rev. A, 77 (2008), p. 023415.

[54] L. Mandel, *Sub-Poissonian photon statistics in resonance fluorescence*, Opt. Lett., 4 (1979).

[55] M. Mandl, *Statistical Physics*, John Willey and Sons, Manchester, 1988.

[56] N. Masuhara, J. Doyle, J. Sandberg, D. Kleppner, and T. Greytak, *Evaporative cooling of spin-polarized atomic hydrogen*, Phys. Rev. Lett., 61 (1988), p. 935.

[57] H. J. Metcalf and P. van der Straten, *Laser Cooling and Trapping*, Springer, 1999.

[58] A. K. Mohapatra, T. R. Jackson, and C. S. Adams, *Coherent optical detection of highly excited Rydberg states using electromagnetically induced transparency*, Phys. Rev. Lett., 98 (2007), p. 113003.

[59] O. Morsch and M. Oberthaler, *Dynamics of bose-einstein condensates in optical lattices*, Rev. Mod. Phys., 78 (2006), pp. 179–215.

[60] M. NIELSEN AND I. L. CHUANG, *Quantum Computation and Quantum Information*, Cambridge University Press, second ed., 2000.

[61] M. S. O'SULLIVAN AND B. P. STOICHEFF, *Scalar polarizabilities and avoided crossings of high Rydberg states in Rb*, Phys. Rev. A, 31 (1985), pp. 2718–2720.

[62] E. PEIK, M. BEN DAHAN, I. BOUCHOULE, Y. CASTIN, AND C. SALOMON, *Bloch oscillations of atoms, adiabatic rapid passage, and monokinetic atomic beams*, Phys. Rev. A, 55 (1997), pp. 2989–3001.

[63] C. PETHICK AND H. SMITH, *Bose-Einstein Condensate in Dilute Gases*, Cambridge University Press, Cambridge, 2002.

[64] W. PETRICH, M. H. ANDERSON, J. R. ENSHER, AND E. A. CORNELL, *Stable, tightly confining magnetic trap for evaporative cooling of neutral atoms*, Phys. Rev. Lett., 74 (1995), pp. 3352–3355.

[65] R. POTVLIEGE AND C. S. ADAMS, *Photo-ionization in far-off-resonance optical lattices*, NJP, 8 (2006), p. 163.

[66] C. SIAS, *Control of matter wave tunneling in an optical lattice*, PhD thesis, Dipartimento di Fisica E. Fermi, Universita' degli Studi di Pisa, Italy, 2007.

[67] K. SINGER, M. REETZ-LAMOUR, T. AMTHOR, L. MARCASSA, AND M. WEIDEMÜLLER, *Suppression of excitation and spectral broadening induced by interactions in a cold gas of Rydberg atoms*, Phys. Rev. Lett., 93 (2004), p. 163001.

[68] J. STANOJEVIC AND R. CÔTÉ, *Many-body Rabi oscillations of Rydberg excitation in small mesoscopic samples*, Phys. Rev. A, 80 (2009), p. 033418.

[69] D. A. STECK, *Rubidium 87 d line data, (revision 2.1.2)*, http://steck.us/alkalidata/, (2009).

[70] B. K. TEO, D. FELDBAUM, T. CUBEL, J. R. GUEST, P. R. BERMAN, AND G. RAITHEL, *Autler-Townes spectroscopy of the* $5s1/2 - 5p3/2 - 44d$ *cascade of cold* ^{85}*Rb atoms*, Phys. Rev. A, 68 (2003), p. 053407.

[71] C. E. THEODOSIOU, *Lifetimes of singly excited states in He I*, Phys. Rev. A, 30 (1984), pp. 2910–2921.

[72] D. TONG, S. M. FAROOQI, J. STANOJEVIC, S. KRISHNAN, Y. P. ZHANG, R. CÔTÉ, E. E. EYLER, AND P. L. GOULD, *Local blockade of Rydberg excitation in an ultracold gas*, Phys. Rev. Lett., 93 (2004), p. 063001.

[73] E. URBAN, T. A. JOHNSON, T. HENAGE, L. ISENHOWER, D. D. YAVUZ, T. G. WALKER, AND M. SAFFMAN, *Observation of Rydberg blockade between two atoms*, Nature Phys., 5 (2009), pp. 110–114.

[74] M. VITEAU, J. RADOGOSTOWICZ, A. CHOTIA, M. BASON, N. MALOSSI, F. FUSO, D. CIAMPINI, O. O. MORSCH, I. RYABTSEV, AND E. ARIMONDO, *Ion detection in the photoionization of a Rb Bose-Einstein condensate*, J. Phys. B: At. Mol. Opt. Phys., 43 (2010), p. 155301.

[75] A. ZENESINI, *Coherence and adiabaticity in dressed matter waves*, PhD thesis, Dipartimento di Fisica E. Fermi, Universita' degli Studi di Pisa,Italy, 2008.

[76] A. ZENESINI, H. LIGNIER, G. TAYEBIRAD, J. RADOGOSTOWICZ, D. CIAMPINI, R. MANNELLA, S. WIMBERGER, O. MORSCH, AND E. ARIMONDO, *Time-resolved measurement of Landau-Zener tunneling in periodic potentials*, Phys. Rev. Lett., 103 (2009), p. 090403.